Orbit Estimation of Geosynchronous Objects Via Ground-Based and Space-Based Optical Tracking

by

Jill Tombasco

B.S., Pennsylvania State University, 2005

M.S., University of Colorado, 2009

A thesis submitted to the

Faculty of the Graduate School of the

University of Colorado in partial fulfillment

of the requirements for the degree of

Doctor of Philosophy

Department of Aerospace Engineering Sciences

2011

This thesis entitled:
Orbit Estimation of Geosynchronous Objects Via Ground-Based and Space-Based Optical Tracking
written by Jill Tombasco
has been approved for the Department of Aerospace Engineering Sciences

_____

Dr. Penina Axelrad

_____

Dr. George Born

Date _____

The final copy of this thesis has been examined by the signatories, and we find that both the content and the form meet acceptable presentation standards of scholarly work in the above mentioned discipline.

Tombasco, Jill (Ph.D., Aerospace Engineering Sciences)

Orbit Estimation of Geosynchronous Objects Via Ground-Based and Space-Based Optical Tracking

Thesis directed by Dr. Penina Axelrad

Angles-only orbit estimation of geosynchronous objects is a unique challenge due to the dense population of clustered geosynchronous objects, the singularities of and perturbations to geosynchronous motion, and the error inherent to experimental observations of geosynchronous objects. Passive optical tracking of geosynchronous space objects has traditionally been performed by ground-based sensors, and the capability has advanced significantly through the introduction of space-based angles-only tracking. This research addresses three key facets of geosynchronous orbit estimation accuracy: improvement to the accuracy via appropriate coordinate modeling, empirical characterization of achievable ground-based angles-only estimation accuracy, and analytic modeling of the space-based angles-only estimated uncertainty. This research develops and analyzes improvements to geosynchronous orbit estimation based on high-fidelity dynamic modeling with a specialized set of coordinates designed specifically to address the geosynchronous orbit conditions. The use of an appropriate representation, the GEO elements, enhances the orbit estimation accuracy compared to the more traditional inertial Cartesian state space representation of geosynchronous motion. Simulation and experimental studies demonstrate that GEO element estimation better recovers the in-track motion than inertial position and velocity state estimation. The short-term estimation accuracy given ground-based tracking is characterized empirically using the Wide Area Augmentation System satellite reference ephemerides. The results show that 10 meter accuracy is possible given short sampling intervals (10 to 30 seconds) and long nightly track lengths (3 or more hours). Several tracking scenarios are found to meet accuracy requirements on the order of 100 meters. The observability of relative states using space-based angles-only tracking of geosynchronous objects by a geosynchronous sensor is analyzed, and first-order analytic expressions for the predicted uncertainty of the along-track separation and intersatellite range are developed

assuming space-based passive tracking. The uncertainty models are validated via Monte Carlo analysis. The results demonstrate that 1 hour of continuous space-based passive tracking can estimate the range to the order of tens of meters, and 12 hours produces range uncertainty on the order of meters. The outcome of this research is a set of methods to improve the performance of geosynchronous orbit estimation, and an enhanced understanding of the accuracy possibilities of angles-only ground-based and space-based geosynchronous orbit estimation.

Dedication

The inspirational value of the space program is probably of far greater importance to education than any input of dollars... A whole generation is growing up which has been attracted to the hard disciplines of science and engineering by the romance of space.

Arthur C. Clarke

Acknowledgements

I would like to acknowledge my advisor, Dr. Penina Axelrad, who managed to make my dissertation research educational, challenging, rewarding, and fun, all at the same time. I have greatly enjoyed my time working with Penny, and have learned so many valuable lessons along the way. I would also like to thank Dr. Moriba Jah, whose guidance provided insight into this work and whose encouragement strengthened my confidence. Also, thanks to the remaining members of my dissertation committee: Dr. George Born, Dr. Webster Cash, Dr. Robert Robertson, and Dr. Hanspeter Schaub. Finally, I would like to acknowledge Oliver Montenbruck for the technical insight which he provided.

I could not have survived the Ph.D. process if not for the support of great friends. To Aurore Sibois, Sebastian Kreissl, Stevi Wood, and Laura Robilotta: each of you made the past four years a wonderful experience, and kept me sane during the most stressful of times.

Finally, I would like to thank my husband, Carl Seubert. I consider myself lucky to have found someone who can provide emotional support when I'm stressed, supply healthy meals when I'm busy working, *and* work through theoretical orbital mechanics with me. Carl: your patience, understanding and love have not gone unappreciated.

Contents

Chapter

Tables

Table

Figures

Figure

Chapter 1

Introduction

It was in a February 1945 letter to the editor of Wireless World magazine that the concept of a geosynchronous satellite was first popularized. "An artificial satellite at the correct distance from the Earth would make one revolution every 24 hours; i.e., it would remain stationary above the same spot and would be within optical range of nearly half the Earth's surface. Three repeater stations, 120 degrees apart in the correct orbit, could give television and microwave coverage to the entire planet. I'm afraid this isn't going to be of the slightest use to our post-war planners, but I think it is the ultimate solution to the problem."[21] The author was Arthur C. Clarke, and the problem to which he was referring was that of usage of the V2 rocket following the end of World War II. While Clarke is generally credited for popularizing the geosynchronous satellite notion, its creator was actually Hungarian pioneer of astronautics Herman Potoĉnik. He proposed the concept of a geosynchronous satellite in his 1928 book, The Problem of Space Travel: The Rocket Motor.[117]

Sixteen years after Clarke's letter was published, the National Aeronautics and Space Administration (NASA) began the Syncom program to test experimental geosynchronous communication satellites. The first satellite to successfully reach the geosynchronous orbit was Syncom 2, launched in July 1963. In addition to testing the inaugural satellite television transmissions, Syncom 2 was used for the first live two-way satellite telephone call between United States President John F. Kennedy and the Nigerian Prime Minister Abubakar Balewa.[50] Now, more than eighty years after its conception, the geosynchronous orbit is densely populated by international commercial, scientific, and military satellites as well as non-operational satellites and debris.

The North American Aerospace Defense Command (NORAD) maintains element sets for all tracked resident space objects. Approximately 400 geosynchronous element sets are publicly available via the SpaceTrack website managed by the U.S. Air Force.[23] The European Space Agency (ESA) Database and Information System Characterizing Objects in Space (DISCOS) contains approximately 1161 catalogued objects that pass through the geosynchronous orbit. Of these, approximately 391 objects are controlled active satellites, approximately 169 objects are in uncontrolled libration orbits, and approximately 594 uncontrolled objects are drifting in or near the geosynchronous orbit (the remaining 7 objects are uncharacterized).[19]

In addition to the geosynchronous orbit regime, several near-geosynchronous orbits exist which are relevant to geosynchronous operations.[110] The Geosynchronous Transfer Orbit (GTO) is a highly elliptic orbit with an apogee of approximately 35,700 kilometers that is used for injection into the geosynchronous orbit. Another class of geosynchronous transportation orbits is subsynchronous orbits, which are at a lower altitude than the nominal geosynchronous altitude and are used to longitudinally transport geosynchronous satellites. Due to the lower altitude, objects in subsynchronous orbits drift in an eastern longitude direction relative to the Earth-fixed frame. Conversely, objects orbiting at a slightly higher altitude than that of the nominal geosynchronous orbit exhibit westerly longitudinal drift. These higher-altitude orbits, referred to as supersynchronous orbits, are typically used as disposal orbits for geosynchronous satellites that have reached their end of life.

Usage of the geosynchronous orbit regime is regulated by the International Telecommunications Union (ITU), an agency of the United Nations responsible for preventing inter-satellite transmission interference and collisions.[75] For operational and assignment purposes, the ITU subdivides the geosynchronous orbit regime into longitudinal slots approximately 0.2 to 2 degrees wide (approximately 150 to 1500 kilometers at the nominal geosynchronous altitude).[90] Ownership of the longitudinal slots is a paradox: during the late 1980s the ITU gave all countries the right to longitudinal slots above their geographic territories, but the current Outer Space Treaty forbids space sovereignty by any nation. In practice, the distribution of longitudinal slots by the

ITU is generally handled on a first-come, first-serve basis, with consideration given to the country that "owns" the desired slot.[75]

Geosynchronous longitudinal slots providing coverage to industrialized nations are in high demand and location availability is quickly becoming exhausted. Taking advantage of the economic principle of supply and demand, the nation of Tonga set a precedent for less developed countries geographically close to industrialized nations leasing the rights to their longitudinal slots.[109] As a result of the demand for operational space and the close spacing of assigned longitudinal slots, an increasing population of geosynchronous and near-geosynchronous objects are operating in close-proximity clusters, particularly in regions of high value. For example, in 2001 Eutelsat operated up to 5 satellites within a single 2 degree-wide slot located near 13 degrees East longitude.[33]

In order to continue successful geosynchronous operations amidst a dense space object population, a robust method of geosynchronous tracking and orbit estimation is necessary. However, geosynchronous orbit estimation is a challenge because of the following reasons:

- The close spacing of objects leads to incorrectly assigned observations of geosynchronous objects.
- There is a large number of newly-discovered debris objects of unknown origin.
- The unique observation geometry strongly couples ground-sensor biases with object orbital parameters.
- The strong influence of Earth's gravitational field in near-resonant orbits creates non-negligible second-order disturbing forces.
- The solar radiation effect is very significant on large communication geosynchronous satellites and is difficult to model correctly.

Geosynchronous objects are typically tracked via optical telescopes (collecting angular and photometric observations), laser ranging sensors or radio frequency sensors (range and range-rate observations). This work focuses on optical (angles-only) geosynchronous orbit estimation. Optical

sensing is a passive data collection technique unrestricted by lasing constraints and capable of detecting space objects outside of the range of radar. Furthermore, as a passive collection technique, optical imaging allows the sensor to track objects surreptitiously. Space-based optical tracking is an attractive addition to ground-based optical sensors due to the reduced weather limitations and potential to perform close-proximity tracking.

1.1 Challenges of Geosynchronous Angles-Only Orbit Estimation

A general orbit tracking and estimation technique is desirable to increase operational commonality; however, a blanket approach to orbit determination can sacrifice solution accuracy. A specialized approach may be necessary to obtain more accurate orbit information for high-value satellites. An angles-only orbit estimation approach focusing on the geosynchronous orbit regime is appropriate because of the particular challenges of observing and estimating the motion of geosynchronous objects. Such challenges can be subdivided into two categories: those that deal with the measurements of geosynchronous objects and those involving the dynamic modeling of geosynchronous objects. Measurement challenges include the availability of observations, the observation geometry relative to a ground-based sensor, correct association of observations and space objects, and systematic measurement error. The dynamic model challenges include realistically modeling orbit perturbations and selecting an appropriate coordinate set to represent geosynchronous object motion. Each of these challenges and its impact on geosynchronous orbit estimation is described in the following subsections.

1.1.1 Observation Availability

Optical observations are only available when the satellite is in proper lighting conditions: the object must be illuminated while the ground-based sensor is not. At best, this restricts collection of optical measurements between the sunset and sunrise terminators. Cloud coverage and lunar illumination also affect the availability of measurements. Additionally, the measurement quality is susceptible to light pollution and atmospheric fluctuations. The sensors therefore tend

to be confined to a limited number of geographic locations, limiting the possible tracking coverage. Furthermore, optical sensors typically track numerous objects throughout the night and are not dedicated to tracking a single object.

1.1.2 Observation Geometry

The limiting geometry of ground-based observations also impacts geosynchronous orbit estimation. Geosynchronous objects are unique in that their position relative to a fixed spot on the Earth remains largely constant, so that collecting more observations of an object from a ground-based sensor will not always provide additional information on the object's orbit. This geosynchronous geometry limitation introduces a specific issue of orbit determination with optical measurements: short duration observations do not expose the orbit geometry. In particular, the semi-major axis is not directly observable via angular observation at any given time, but rather through the angular rate of change. Consequently, a single night of data is not sufficient to achieve a reliable high-accuracy solution.

1.1.3 Observation Association

The recent development of more powerful wide-field-of-view (WFOV) sub-arcsecond accuracy optical sensors has resulted in the ability to detect smaller and, in some cases, previously untracked geosynchronous and near-geosynchronous objects.[34] This capability, combined with the increasing population of geosynchronous objects, means that it is becoming more likely that an optical sensor will detect multiple objects simultaneously. The presence of multiple objects can lead to the misidentification of a target and incorrect association of observations and targets. Incorrectly assigned measurements may degrade the quality of space tracking databases by introducing unrealistically large measurement residuals to the estimation process. There also exists the possibility that the sensor will misidentify an object, which can lead to reacquisition issues and ultimately lost objects.

1.1.4 Sensor Bias and Systematic Measurement Error

Optical measurements contain underlying systematic errors and biases which degrade measurement quality. At the geosynchronous altitude, 1 arcsecond of angular error from the ground corresponds to approximately 200 meters of position error. Unaccounted measurement error can contribute to state estimate error; for example, an unmodeled azimuth observation offset of 1 arcsecond can result in a longitude estimate error of approximately 200 meters. As such, accounting for systematic measurement error is key to accurate geosynchronous orbit estimation.

Systematic measurement errors are typically unique to a particular sensor, site location, and pointing direction. The sensor may be calibrated to reduce systematic error, but in general some uncharacterized measurement error remains. A possible means of mitigation is to estimate for the uncharacterized systematic measurement errors. However, the geometric sensitivity of geosynchronous object measurements is often such that measurement error cannot be discriminated from orbital element error.

1.1.5 Dynamic Model Error

The accuracy of orbit estimation is further limited by error within the dynamic model, which arises from imperfect modeling of the forces acting on an object as well as numerical error introduced by propagation of an inappropriate coordinate representation. The dominant disturbing forces on objects in geosynchronous orbits are perturbations due to the oblateness of the Earth, lunisolar gravitational attraction, and solar radiation pressure. Additional disturbing forces acting on the object are orders of magnitude smaller than these dominant perturbations, but may be non-negligible when an object is in resonance with the Earth's rotation. Certain perturbations, such as gravitational forces, depend on the precise locations of the attracting bodies and spacecraft at a specific time and can be modeled generically for all spacecraft. Other perturbations, such as solar radiation pressure, are highly dependent on individual spacecraft properties in addition to the spacecraft position, such as surface reflectivity, total mass, and sun-facing surface area. A highly

accurate dynamic model must tailor the solar radiation disturbing forces to individual objects.

Spacecraft orbits are generally propagated forward in time via numerical integration of the dynamic model. The choice of coordinate representation and the integration step size are nontrivial for accurate geosynchronous dynamic modeling. Classical orbit elements are undefined for circular equatorial orbits, and the commonly-used variational equations become singular for zero eccentricity and inclination, which can introduce numerical issues for near-zero eccentricity and inclination. Inertial Cartesian coordinates vary rapidly, so that large integration time steps lose dynamic fidelity. As the dynamics of a geosynchronous object are slowly varying, an element set that also changes slowly over time is better suited for modeling than an element set that changes more rapidly. Earth-fixed Cartesian coordinates are slowly varying; however, these coordinates are difficult to use due to the inherent error introduced by the necessary reference frame transformations. The integration time step for geosynchronous propagation should also be carefully chosen, as time steps that are too small may introduce errors due to limited numerical precision in the case of small perturbations.

1.2 Overview of Research

The research presented in this dissertation focuses on improving orbit estimation of geosynchronous objects using angles-only observations, as well as analyzing the estimated orbit accuracy given ground-based and space-based passive tracking. Specific geosynchronous orbit estimation challenges discussed in this chapter are addressed through this work. The goals of this research are as follows:

- Develop a high-accuracy dynamic model of geosynchronous motion using a well-suited coordinate representation.
- Develop an estimation strategy using angles-only observations and an appropriate dynamic modeling coordinate set.
- Characterize the achievable geosynchronous orbit accuracy given ground-based angles-only measurements collected by a single sensor.

- Assess the observability of the state of a deputy object relative to a chief object given only space-based angular measurements.
- Develop a model of estimated orbit accuracy given geosynchronous-to-geosynchronous (GEO-to-GEO) space-based angles-only observations.

Each of these research goals is now discussed in further detail.

1.2.1 Coordinate Representation of Geosynchronous Motion

The uniqueness of the geosynchronous orbit regime, including near-circular equatorial singularities and minimal satellite motion with respect to an Earth-fixed frame, leads to the necessity for specialized dynamic modeling of satellite motion. Conventional methods for orbit propagation and estimation use classical Keplerian elements or inertial position and velocity vectors to represent the position and velocity states. Unfortunately, neither of these representations is ideal for the near-geosynchronous regime; classical orbit elements are poorly defined for near zero eccentricity and inclination, and the rapidly-changing inertial position and velocity coordinates obscure the simplicity and near-linearity of geosynchronous motion.[37] Equinoctial elements are comparable to the classical elements but are better suited to the low inclination, low eccentricity case. The synchronous elements are a specialized set defined specifically for low inclination, low eccentricity, 24-hour period orbits.[90]

This study investigates dynamic modeling and orbit estimation of geosynchronous satellites using traditional and specialized orbit representations. Nonlinear variational equations for generally-perturbed synchronous elements are developed via Poisson brackets. A hybrid element set of synchronous and equinoctial elements called the GEO elements is also introduced to avoid numerical sensitivities. Numerical propagation studies evaluate the precision and accuracy of inertial Cartesian, Keplerian, synchronous and GEO element dynamic models. The suitability of approximating the synchronous element equations of motion for small eccentricity and inclination values is assessed. Results show that the nonlinear GEO and synchronous models are consistent for

large and small time-steps and are of comparable accuracy to the more traditionally-used inertial Cartesian model. This work has been published in the *Journal of Guidance, Control and Dynamics (Tombasco, Axelrad and Jah).*[98]

1.2.2 Angles-Only Estimation Strategy

Given the slowly-varying motion of geosynchronous satellites relative to an Earth-fixed sensor, ground-based optical observations of geosynchronous objects do not exhibit a strong time-variation over short time periods even up to one night. Also, the GEO elements are shown to vary in a near-linear fashion for natural perturbed orbital motion. For these reasons, this work applies a batch estimator for the angles-only orbit determination problem. The GEO element model developed for the dynamic modeling research is further validated via an estimation analysis in which two nights of experimental and simulated optical data of the Tracking and Data Relay Satellite (TDRS) 8 are each processed by a GEO element batch estimator. For comparison, the same measurements are processed by an analogous inertial Cartesian state batch estimator. The results show that the GEO elements are suitable for geosynchronous dynamic modeling and estimation. Additionally, the GEO element batch estimator provides a more accurate estimate of the state and covariance than the Cartesian position and velocity estimator because the GEO element estimator is less affected by errors introduced through the measurement linearization. The simulation analysis shows that the GEO element estimation error is on the order of 10 meters in radial, in-track and cross-track position and 10 millimeters per second in each velocity component; the inertial Cartesian state space estimator produces error on the order of 500 meters in the in-track position component and 4 centimeters per second in the radial velocity direction. This work has been published in the *Journal of Guidance, Control and Dynamics (Tombasco, Axelrad and Jah).*[98]

1.2.3 Accuracy of Ground-Based Geosynchronous Orbit Estimation

Orbit estimation accuracy is a measure of the error in the estimated orbit from the truth orbit; however, direct computation of the estimation error is only possible for simulation studies in

which the truth orbit is known. In the absence of a truth orbit for experimental orbit estimation, the orbit accuracy must be assessed via other metrics, such as the postfit measurement residuals, the estimated covariance or a reference orbit if one is available. Certain spacecraft are tracked regularly and their reference orbits maintained to some required accuracy. For example, the TDRS satellites operated by the National Aeronautics and Space Administration (NASA) are tracked with ground-based radar systems and osculating element sets accurate to tens of meters are provided at 24-hour intervals.[57] The TDRS satellites have previously been used to asses the accuracy of angles-only orbit estimation.[76; 77] The Two-Line Element Sets (TLEs) provided by NORAD are also used as reference point solutions; however, the TLEs are limited and of variable accuracy (sometimes on the order of tens of kilometers); are updated on an irregular basis (on the order of every few days to every few weeks); and are generated for use with a specific dynamic model.[102]

By taking advantage of meter-level accuracy high-rate reference ephemerides, this work investigates the geosynchronous orbit estimation accuracy that can be achieved given short-term dedicated tracking by a single ground-based optical sensor. Two Global Positioning System (GPS) Wide Area Augmentation System (WAAS) satellites are chosen for this case study because highly-accurate WAAS reference position and velocity point solutions are available for public use and present the opportunity to experimentally assess the effect of orbit perturbations to the meter level. Simulated (noisy) angles-only observations are generated from these experimental reference ephemerides. By varying the tracking parameters of nightly tracking arc length, sampling rate, and orbit epoch, and fitting to two consecutive days of observations, a batch estimation analysis is performed which empirically characterizes the expected level of two-day solution accuracy given an imperfect dynamic model and a satellite which is performing small, frequent maneuvers. The results show that the estimated solution fits over the two-day period to better than 10 meters. An analysis of one month of data for an uncontrolled satellite is performed to statistically determine the solution uncertainty and mean accuracy. It is shown that 10 meter accuracy is possible given short sampling intervals (10 to 30 seconds) and nightly track lengths or 3 or more hours per night. Several tracking scenarios are found to meet accuracy requirements on the order 100 meters. This

work has been accepted for publication in the *Journal of Astronautical Sciences (Tombasco and Axelrad).*[97]

1.2.4 Observability of Relative GEO Elements Given Space-Based Angles-Only Measurements

Previous studies relying on Hill's linearized equations of motion have concluded that relative orbit estimation is not possible given close-proximity space-based angles-only measurements when both objects are in unperturbed orbits.[112] The issue is a lack of observability of the along-track separation. However, as is shown in this work, the observability issue can be mitigated by using a different coordinate representation of the relative motion. The observability of the relative GEO elements for two objects in Keplerian geosynchronous orbits is explored using relative angular measurements and a spherical representation of the relative position vector. The spherical coordinate dynamic model of relative motion is linearized about the chief satellite's orbit, and a dynamic model analogous to Hill's relative motion model is constructed by assuming that chief spacecraft is in a circular equatorial orbit. The full measurement sensitivity matrix is derived and the observability demonstrated via numerical simulation studies. The results show that the use of a spherical coordinate representation allows the relative GEO elements to be recovered while still employing a simple linearized dynamic model (analogous to the Hill's relative motion dynamic model) and angles-only measurements. This work has been accepted for publication in the *Journal of Guidance, Control and Dynamics (Tombasco and Axelrad).*[96]

1.2.5 Estimated Covariance for GEO-to-GEO Space-Based Angles-Only Tracking

In general orbit determination applications, particularly the processing of experimental data when no reference orbit is available, the estimated covariance may be the single most important piece of information produced by an estimator. The final focus of this research is the modeling and analysis of the estimated orbit uncertainty expected given space-based angles-only tracking data. Rather than study the predicted covariance through an empirical analysis, the covariance

profile for a subset of elements is modeled analytically. This is performed by finding a first-order solution to the Riccati matrix equation, which governs the covariance temporal behavior given continuous observations. The linearized spherical coordinate dynamic model is further simplified by assuming that the relative motion is bounded. In order to produce a closed-form analytic solution, the Riccati equation is linearized to first order about zero differential inclination. The variance profile is determined for the relative longitude as this is the limiting parameter for orbit accuracy. The estimated uncertainty in the along-track separation is modeled as a function of the *a priori* covariance information, the Gaussian measurement noise distribution, the chief spacecraft mean motion and the orbit arc swept out by the chief spacecraft during the tracking time. The variance profile of the range from the chief spacecraft to the deputy spacecraft is analytically modeled to provide a single metric of the relative uncertainty. The first-order predicted uncertainty profiles are numerically validated through a Monte Carlo analysis of the estimated state errors and uncertainty. The results demonstrate that 1 hour of continuous space-based passive tracking by a well-placed observing satellite can decrease the intersatellite range uncertainty to the order of tens of meters. Approximately 12 hours of observations produces meter-level range uncertainty. The results also show that the first-order predicted range uncertainty is within a few meters of the non-approximated estimated range uncertainty given a relative inclination of $1\text{x}10^{-2}$ degrees, which produces a maximum out-of-plane separation of approximately 7.5 kilometers.

1.3 Previous Work

The dynamic modeling and angles-only orbit estimation of geosynchronous objects, including active and inactive satellites as well as debris objects, has been extensively researched over the past few decades. The following section briefly summarizes the most relevant references such that the contributions of this work may be placed in the context of prior efforts. Further details on each reference, as well as additional references, are presented in the subsequent chapters.

1.3.1 Geosynchronous Dynamic Modeling

Research documents regarding the dynamics of geosynchronous objects can be found dating back to the 1960s. One of the pioneering researchers in the field of Earth-resonant motion was Ahmed Aly Kamel, who published several significant papers on perturbed geosynchronous motion.[38; 39; 40] His work developed linearized analytic models representing the change in mean orbital elements given approximated effects of the dominant geosynchronous perturbations: solar radiation pressure, non-spherical Earth gravity, and luni-solar third body gravity.

Erik Mattias Soop literally wrote the book on geosynchronous dynamic modeling and standard operational practices.[90] Soop presented a dynamic model that is linearized about the geostationary orbit and is defined in the synchronous elements. Soop's model is primarily used by European satellite operators and researchers.[61] His text focuses on practical geosynchronous satellite operations, including generalized models for station-keeping maneuvers, proximity operations and longitude maintenance.

Most recently, the literature has focused on the long-term evolution of high area-to-mass geosynchronous debris objects. Stephane Valk, Anne Lemaitre, et. al. have developed a semi-analytic Hamiltonian dynamic theory to model the naturally perturbed motion of this class of objects.[53; 99; 100; 101] Their development was geared towards long-term evolution studies on the order of several decades to several centuries.

1.3.2 Ground-Based Geosynchronous Orbit Estimation

Tracking and estimation of a geosynchronous object via ground-based optical sensors has been researched through both simulation and experimental analysis. One of the most prolific authors of simulation studies, both ground-based and space-based, has been Sawada Kawase.[44; 47] Using a linearized dynamic model, Kawase theoretically modeled the orbit determination error given the level of optical measurement noise. Kawase showed that the expected orbit uncertainty is on the order of 1 kilometer assuming Gaussian measurement noise of 1 arcsecond.

Additional work in the area of simulation and experimental data analysis has been completed by Chris Sabol, et. al.[76; 77; 78] The simulation studies showed that a week of optical data resulted in orbit accuracy on the order of 10 meters.[76] However, it was shown that there was a discrepancy between the simulated estimation accuracy and that which had so far been achieved in experimental analysis. Processing of experimental optical data produced solutions that were only accurate to a few hundred meters.[78]

David Vallado, et. al. have published the results of combining international sources of optical data for the purposes of collision avoidance.[105; 106] This cooperative angles-only orbit estimation allows for ground-based coverage of the entire geosynchronous belt.[6] The results have shown that orbit solutions with uncertainty on the order of a few kilometers can be achieved given sparse data collected over several days.

Thomas Schildknecht, et. al. have performed extensive experimental analysis of angles-only space debris orbit estimation and propagation.[63; 64; 84; 85] Specifically, their work has led to the discovery of a population of high area-to-mass debris objects in highly-eccentric orbits crossing through the geosynchronous orbit regime. Orbit fits to years' worth of optical data has been used to study the long-term motion of this unexpected set of objects.

1.3.3 Geosynchronous Relative State Estimation

High-accuracy WFOV ground-based and space-based optical sensors are capable of simultaneously tracking multiple geosynchronous objects, and as such several estimation techniques have been presented which exploit the commonalities between close-proximity geosynchronous object dynamics and reduce measurement errors given ground-based optical data.

Sawada Kawase demonstrated the observability of relative non-singular orbit elements given ground-based differential angular measurements, and developed a first-order approximation for the expected uncertainty after one day of tracking.[48] Simulation studies in which one week of continuous radio-interferometric measurements were processed with a correlated Kalman filter showed approximately 50 meters of estimate error.[46] However, experimental analysis produced errors on

the order of a few hundred meters.[45]

Chris Sabol and Keric Hill, et. al.[33; 79] have also investigated relative orbit estimation through simulation and experimental data analysis. Simulation results fitting to multiple nights of data demonstrated 50 meters of orbit error.[79] Experimental orbit estimation analysis in which two nights of optical data were processed with a batch estimator and the propagated solution compared with subsequent data arcs demonstrated error on the order of 10 kilometers.

1.3.4 Relative State Observability Given Space-Based Angles-Only Measurements

The launch and operation of the Space-Based Space Surveillance (SBSS) satellite has led to numerous research papers discussing the observability limits of space-based angles-only tracking and estimation. David Woffinden and David Gellar [112; 113] have clearly demonstrated the limitations on observability when using Hill's linearized rectilinear model of relative motion and space-based angles-only measurements.[112] Essentially, for this scenario they showed that the intersatellite range was not observable from angular measurements. Their follow-on work developed optical maneuvers which the tracking spacecraft can perform in order to introduce observability.[113]

Another method of mitigating the observability limitations of space-based angles-only tracking was proposed by J. Schmidt and T. Alan Lovell.[86] Their work formed a subset of elements describing the two-body elliptical motion of a deputy spacecraft as seen by a chief spacecraft as functions of the space-based angular measurements. It was assumed that the measurements are not degraded by noise or systematic errors, and the measurements were solved for an element subset, which aided in the determination of a set of orbits to which an object may belong.

Research relevant to the angles-only observability issue is also found outside of the field of aerospace engineering. Sherry Hammel, et. al. [30] have explored similar concepts for the application of underwater craft formation tracking and control. Given bearings-only measurements of a deputy craft relative to a chief craft, the requirements for full state observability were developed. A framework for chief craft maneuvers to enhance observability were introduced, and special conditions in which a subset of position and velocity states may be recovered were presented.

1.3.5 Space-Based Angles-Only Relative State Estimation Accuracy

The SBSS satellite is able to provide space-based angles-only optical measurements via the Space-Based Visible (SBV) sensor package.[31] This measurement accuracy of this sensor is approximately 4 arcseconds.[108] Additionally, Canada is planning a fully-operational SBSS satellite, Sapphire, which is planned to be contributing to the US Space Surveillance Network (SSN) by the end of 2011.[58] Initial experiments indicate that the Sapphire visible sensor has an accuracy of approximately 3 arcseconds.[87]

Simulation studies of angles-only initial orbit determination for space-based tracking data have been performed by David Vallado.[56; 104] These simulation studies assessed how the orbital regime of the tracker satellite affects the orbit estimation accuracy of a tracked geosynchronous object.[104] The results showed that significant relative motion between the chief and deputy satellites resulted in better orbit accuracy than scenarios with little relative motion. Additional simulation studies have shown that the inclusion of ground-based optical data can help the filter converge in cases of limited observability.[56]

Finally, Sawada Kawase [43] has published relevant research developing analytic expressions for the expected covariance given range and angles tracking. Assuming a linearized two-body dynamic model and no *a priori* information, Kawase predicted the estimated covariance of a subset of orbit elements given noisy range and azimuth measurements collected over one day. The range measurements are solved for the in-plane orbit elements of the deputy, and the azimuth measurements (defined as measuring the out-of-plane angular displacement relative to a chief satellite) are solved for the out-of-plane elements.

1.3.6 Covariance Propagation

Typically, covariance propagation is performed via linearized mapping that has been approximated about some nominal trajectory.[94] Sorenson and Alspach [91; 9] published the technique of Gaussian Mixture Modeling, in which a non-Gaussian error distribution is modeled as a sum

of Gaussian distributions. Park and Scheeres [69; 70] have introduced higher-order state transition tensor mapping for more accurate covariance propagation for nonlinear systems. DeMars [24] developed an accurate covariance propagation method that is not computationally intense, which measures the system nonlinearity to determine whether to use a standard sigma-point propagation of the Gaussian Mixture Model. This technique has been proven to be very accurate for the propagation in nonlinear systems. The work presented in this thesis leverages the simplicity and near-linearity of the GEO elements and uses a first-order linearized covariance mapping with no significant loss in accuracy.

1.4 Contributions of Research

The research developments presented in this dissertation are further advancements to the efforts in dynamic modeling of geosynchronous motion and angles-only geosynchronous orbit estimation using ground-based and space-based optical measurements. Now, the specific contributions of each section of this thesis are outlined and the contributions of this research as compared to the previous work by other authors are summarized.

1.4.1 Dynamic Modeling and Estimation Coordinate Representation

The development of a high-fidelity geosynchronous dynamic model depends on the choice of modeling coordinates and the inclusion of orbit perturbations. In contrast to the long-period averaged models, this research focuses on modeling the short-period dynamics (on the order of several days) of the osculating elements. Also, a general perturbation model is used and the GEO element variational equations are not linearized about geosynchronous orbits. This research has led to the development of a hybrid set of synchronous and equinoctial elements as an appropriate coordinate representation for geosynchronous motion. A nonlinear GEO element dynamic model for general perturbations that is numerically stable for the propagation of geosynchronous and near-geosynchronous orbits has been developed and validated. Also, a GEO element batch estimator has been developed and validated with simulated and experimental optical data.

The specific contributions of the research on coordinate representation for dynamic modeling and estimation include the following:

- Appropriate coordinate representation for geosynchronous dynamic modeling
- Effect of coordinate selection on dynamic propagation of geosynchronous motion
- Development of an accurate perturbed dynamic model
- Required complexity to accurately model realistic perturbations
- Improvements to batch estimation of a geosynchronous object by selecting an appropriate coordinate representation
- Validation using TDRS reference data, and simulated and experimental optical observations

Next, a direct comparison of this thesis research with the relevant work of other authors in the area of geosynchronous dynamic modeling is provided. Fig. 1.1 summarizes the contributions of the prior work and this research.

Prior Work	Contributions of Prior Work	Contributions of Thesis Research
Kamel[38-40]	Linearized effect of luni-solar, Earth triaxiality and solar pressure perturbations on mean elements	Non-linear osculating element variational model for general perturbations
Soop[90]	Linearized equations of motion for two-body geosynchronous motion	Non-linear equations of motion for perturbed geosynchronous motion
Valk, et. al.[98-101]	Long-term averaged model of perturbed geosynchronous motion	Perturbed geosynchronous motion applicable to short-term modeling

Figure 1.1: Comparison of Geosynchronous Dynamic Modeling Research and Related Prior Work

1.4.2 Ground-Based Angles-Only Orbit Estimation Accuracy

The accuracy of an estimated orbit can only be determined to the accuracy level of the reference orbit. This work uses recent high-accuracy WAAS reference ephemerides to assess the estimated orbit accuracy to the meter-level. This is a significant accuracy improvement over the commonly-used TDRS reference osculating elements and TLEs. The failure of Galaxy 15 during the research period, serendipitous for this study, offers the unique opportunity to process experimental high-accuracy point solutions of an uncontrolled geosynchronous satellite. Novel case studies of two WAAS satellites, Anik F1R and Galaxy 15, enable a true test of accuracy using realistic vehicle motions for both controlled and drifting vehicles.

Specific contributions on the research on ground-based orbit estimation accuracy include:

- Development and validation of GEO element batch estimation with optical data
- Validation with high-accuracy experimental WAAS reference ephemerides
- Analysis of meter-level realistic orbit dynamics of controlled and uncontrolled geosynchronous satellites
- Determination of minimum tracking data requirements to achieve desired orbit accuracy performance

Fig. 1.2 provides a comparison of the contributions of this research with the contributions of the significant related work performed by others.

Prior Work	Contributions of Prior Work	Contributions of Thesis Research
Kawase[44,47]	Linearized analytic model of expected geosynchronous orbit accuracy given sparse optical measurements	Empirical analysis of achievable geosynchronous orbit accuracy given two days of optical measurements collected at various rates
Sabol, et. al.[76-77]	Simulation & experimental analysis of geosynchronous orbit accuracy for several days to a week of data (compared to TDRS reference orbit)	Empirical analysis of shorter-term orbit accuracy using meter-level experimental reference ephemerides; systematical study of effect of tracking parameters on accuracy
Vallado, et. al.[103-104]	Experimental analysis of geosynchronous orbit accuracy given several days of sparse optical data (compared to TLEs)	Empirical analysis of shorter-term orbit accuracy using meter-level experimental reference ephemerides; systematical study of effect of tracking parameters on accuracy
Schildknecht, et. al. [98-99]	Experimental analysis of several years of optical data of high area-to-mass geosynchronous debris	Empirical analysis of short-term optical data of low area-to-mass geosynchronous spacecraft

Figure 1.2: Comparison of Ground-Based Orbit Estimation Research and Related Prior Work

1.4.3 Space-Based Angles-Only Covariance Prediction

In order to better understand the capabilities of space-based angles-only tracking, this work investigates the orbit accuracy of a GEO-to-GEO tracking system. The first major contribution of this research is the demonstration that space-based angles-only tracking and estimation is possible for Keplerian orbits without maneuvering the chief satellite. The second contribution is the development of analytic covariance modeling for the relative longitude and intersatellite range estimated uncertainty. These developments lead to a set of orbit estimation tools which may be used to approximate the minimum tracking requirements necessary to obtain a desired relative orbit accuracy.

Specific contributions to the field of space-based angles-only orbit estimation include:

- Development of relative GEO element batch estimator that processes space-based angles-only measurements
- Numerical demonstration of full observability of relative GEO elements given space-based angles-only measurements
- Analytic development of approximated model of estimated covariance to predict uncertainty of along-track separation
- Analytic development of approximated model of estimated covariance to predict uncertainty of intersatellite range
- Validation of analytic models with Monte Carlo analysis of GEO-to-GEO optical measurements
- Determination of minimum tracking data requirements to achieve desired orbit accuracy performance

Finally, Fig. 1.3 addresses the most significant relevant research contributions published by

others, and how the research presented in this dissertation expands the understanding of space-based angles-only orbit estimation accuracy.

Prior Work	Contributions of Prior Work	Contributions of Thesis Research
Woffinden, et. al. [109-112]	Observability analysis given Hill's rectilinear linearized model of relative motion and space-based angles-only measurements	Observability analysis given a spherical model of linearized relative motion and space-based angles-only measurements
Schmidt, et. al.[86]	Theoretical expressions for a subset of relative geometry elements given perfect space-based angular measurements	Theoretical expressions for a subset of relative hybrid elements given noisy space-based angular measurements
Vallado, et. al.[56,102]	Simulation analysis of GEO-to-GEO Gooding angles-only initial orbit determination accuracy	Analytic analysis of GEO-to-GEO batch estimation orbit accuracy for a subset of relative hybrid elements
Kawase[43]	Development of linearized analytic model of deputy element estimated covariance given no *a priori*, range and angles observations, and tracking duration spanning one day	Development of linearized analytic model of relative hybrid element estimated covariance incorporating *a priori*, angles-only observations, and variable tracking duration

Figure 1.3: Comparison of Space-Based Orbit Estimation Research and Related Prior Work

1.5 Thesis Overview

The remainder of this dissertation is outlined as follows. Chapter 2 presents the development of a high-fidelity geosynchronous dynamic model and numerical simulation results. A general discussion of orbit estimation approaches is given in Chapter 3, which also presents the development of a GEO element batch processor and the results of experimental and simulated orbit estimation of a single geosynchronous object. Chapter 4 presents details on the WAAS reference ephemerides and the empirical characterization of the ground-based orbit estimation accuracy. Chapter 5 develops the relative GEO element batch estimator, and demonstrates that the relative GEO elements are observable given space-based angles-only measurements and a spherical coordinate linearized Keplerian model of relative motion. This concept is expanded in Chapter 6, in which the model described in Chapter 5 is used to develop the analytic covariance models. Chapter 6 also presents the results of a Monte Carlo analysis which validate the analytic covariance profiles. Finally, Chapter 7 summarizes the dissertation research and outlines future work as an extension of this dissertation research.

Chapter 2

Geosynchronous Dynamic Model

2.1 Introduction

The evolution of natural satellites has been studied extensively for millennia. The earliest-known study of orbital motion was performed in ancient Babylonia, as the Chaldeans developed the Saros cycle to predict solar eclipses throughout the last few centuries B.C.[29] Fundamental understanding of the kinematics of orbital motion was introduced through the combination of Tycho Brahe's meticulous celestial observations (16^{th} century) and Johann Kepler's theoretical developments (early 17^{th} century).[12] The final piece which brought together the basic theory of planetary motion was Isaac Newton's dynamical laws (late 17^{th} century).[102] (Interestingly, Newton's Ph.D. thesis made no mention of his theory of gravitational forces.) Progressing forward to October 4, 1957, a new era of space exploration was born when the Soviet Union successfully launched the first man-man satellite into Earth orbit and started the space age as we know it.[3] The first geosynchronous satellite was launched in 1963 [50], and thus began dedicated studies of the orbital motion of geosynchronous objects, whether man-made or natural.

One of the pioneering researchers who developed theory relevant to geosynchronous motion was R. R. Allan [8], whose work included the study of how the Earth's gravitational field affects objects that are in resonance with the Earth's rotation rate. Building on the initial gravitational work by Kaula [41], Allan developed a disturbing function to model the long-period pendulum effect on a satellite's longitude. This disturbing function essentially models the libration about the gravity wells located at 75.1 degrees East longitude and 105.3 degrees West longitude.[90]

Geosynchronous orbit perturbation modeling was expanded by Kamel [38; 39; 40], who used a simple Hamiltonian pendulum system to approximate a low degree and order Earth gravitational field with luni-solar gravitational effects. The disturbing functions were developed for the mean equinoctial elements[38], which were then converted into osculating equinoctial elements[40]. The model was an approximation due to the limited Earth, Sun and Moon gravitational coefficients included, but provided a simple analytic model that is useful for quick consideration of two of the primary perturbations on a geosynchronous satellite. Earlier work by Kamel included the study of the effect of solar radiation pressure of the mean eccentricity of a geosynchronous orbit.[39] His work developed an analytic model of the mean eccentricity evolution and strategies for eccentricity control. A major finding of Kamel is that under the influence of solar radiation pressure, the mean eccentricity vector evolution is dependent on the spacecraft shape and size.

Throughout the past two decades, the interest in geosynchronous dynamic modeling has primarily revolved about the operational hazards introduced by debris objects in or passing through the geosynchronous orbit. Friesen, et. al. [27] simulated the motion of large and satellites in storage orbits above and below the nominal geosynchronous altitude, small debris objects initially in the circular geosynchronous orbit and small debris originating in the geosynchronous transfer orbit. The simulations were performed over a period of 100 years. The results showed that the large satellites did not exhibit large altitude changes but did show inclination oscillation due to the luni-solar perturbations. The smaller particles, however, were primarily driven by the solar radiation pressure and exhibit both eccentricity and inclination oscillations.

Most recently the long-term evolution of high area-to-mass debris objects has been studied extensively.[53; 99; 100; 101]. Valk, et. al. [100] have developed a semi-analytical Hamiltonian dynamic modeling theory which averages the geosynchronous motion over one day, and has been proven to be useful for long-term evolution studies on the order of several decades. The model included perturbations due to the J_2 gravity term, luni-solar gravity, and solar radiation pressure. The model was used to study the perturbed motion of high area-to-mass debris objects, and in particular, models coupling between the eccentricity and inclination evolution due to solar radiation

pressure. Follow-on work investigated the long-term evolution of the orbit altitude[99] and the equilibria, stability and fundamental frequencies of the resonant motion[101]. In addition to the Earth resonance, Valk, et. al. [53] introduced a secondary resonance between the object's position and the longitude of the Sun. The impact of the secondary resonances is directly proportional to the object's area-to-mass ratio.

In contrast to the long-period models, this research focuses on modeling the osculating element short-period dynamics (on the order of several days). This chapter discusses why neither a Cartesian position and velocity nor classical orbit element representation is ideal for geosynchronous representation and introduces coordinates that are designed to exploit the peculiarities of the geosynchronous orbit regime. The synchronous elements, defined by Soop [90], are a specialized set defined specifically for low inclination, low eccentricity, 24-hour period orbits. The development of a geosynchronous dynamic model presented in this chapter investigates perturbation modeling with the synchronous elements and a hybrid set of synchronous and equinoctial elements (known as the GEO elements) as compared to the Keplerian and Cartesian coordinates. A nonlinear synchronous element dynamic model is developed for arbitrary perturbations, and the validity of small inclination and eccentricity approximations is explored. A nonlinear GEO element dynamic model is also developed and assessed. Additionally, an overview of the dominant orbital perturbations acting on geosynchronous objects is presented.

2.2 Conventional Dynamic Modeling

2.2.1 Cartesian Coordinates

Traditional dynamic modeling, including that of some commercial software packages such as the Orbit Determination ToolKit (ODTK) and the Goddard Trajectory Determination System (GTDS), uses Cartesian three-dimensional position and velocity vectors to represent an object's motion.[55; 1] As geosynchronous orbits remain largely stationary relative to an observer on the Earth, an Earth-Centered Earth-Fixed (ECEF) Cartesian coordinate representation does not vary

greatly over time. In contrast, coordinates in an Earth-Centered Inertial (ECI) Cartesian reference frame change rapidly with respect to time. Neither of these Cartesian coordinate representations is particularly well-suited for geosynchronous dynamic modeling.

As discussed by Junkins [37], the choice of coordinate representation should be made in order to take advantage of the linearity or near-linearity of motion. Geosynchronous object motion is highly nonlinear as seen by an ECI frame, while the ground-based observations are nearly constant. This high level of nonlinearity obscures the simplicity of the geosynchronous motion and requires small integration time steps for propagation, which in turn may cause numerical issues when including small perturbing forces over long time periods.

In contrast, a geosynchronous object remains primarily fixed as seen by an ECEF frame; this slowly-varying motion is mirrored by the near constancy of ground-based observations. While this representation is well-suited for the linearity of the geosynchronous motion, unnecessary dynamic model error is introduced by transforming all perturbing forces precisely to ECEF rotating frame.

2.2.2 Classical Orbit Elements

The widely-used classical orbit elements are defined as the semi-major axis, a, eccentricity, e, inclination, i, ascending node, Ω, argument of perigee, ω, and true anomaly, ν. Fig. 2.1 presents the physical definition of each of the elements in the orbit reference plane and the Earth-Centered Inertial frame. Note that the argument of perigee and mean anomaly angular elements become undefined for a circular orbit. Additionally, for a zero inclination orbit the ascending node becomes undefined.

The poor definition of the classical orbit elements for near circular equatorial orbits makes such elements a poor choice to represent geosynchronous orbits. Furthermore, the classical orbit element equations of motion are not well formulated for zero inclination or zero eccentricity. The orbit element variational equations are given by [83]:

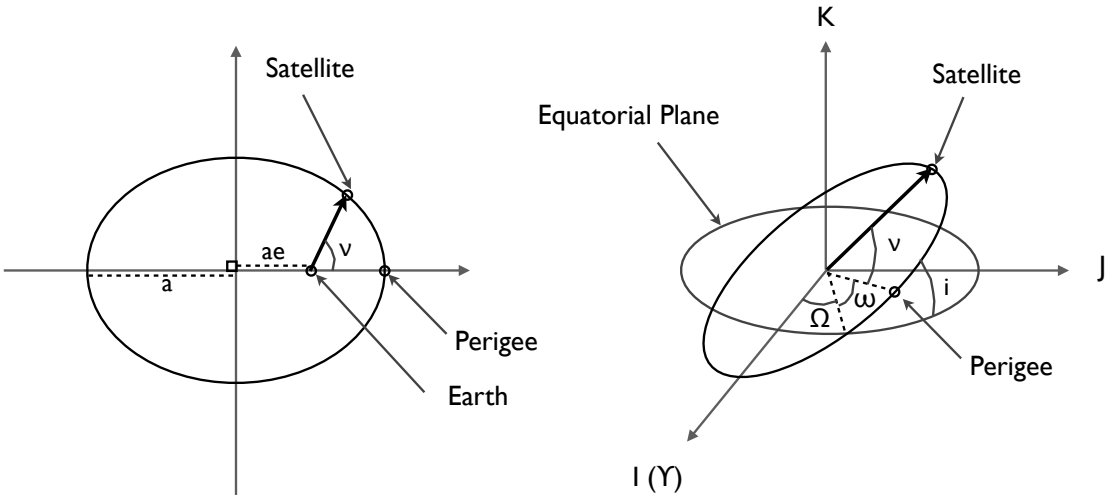

Figure 2.1: Definition of Classical Orbit Elements

$$\dot{a} = \frac{2a^2}{h}\left\{e\sin(\nu)a_r + \frac{p}{r}a_\theta\right\} \tag{2.1}$$

$$\dot{e} = \frac{1}{h}\left\{p\sin(\nu)a_r + \left[(p+r)\cos(\nu) + re\right]a_\theta\right\} \tag{2.2}$$

$$\dot{i} = \frac{r\cos(\theta)}{h}a_h \tag{2.3}$$

$$\dot{\Omega} = \frac{r\sin(\theta)}{h\sin i}a_h \tag{2.4}$$

$$\dot{\omega} = \frac{1}{he}\left\{-p\cos(\nu)a_r + (p+r)\sin(\nu)a_\theta\right\} - \frac{r\sin(\theta)\cos i}{h\sin i}a_h \tag{2.5}$$

$$\dot{\nu} = \frac{h}{r^2} + \frac{1}{he}\left\{p\cos(\nu)a_r - (p+r)\sin(\nu)a_\theta\right\} \tag{2.6}$$

in which θ is the argument of latitude, r is the radial distance of the satellite from the center of the Earth, p is the semi-latus rectum, and h is the angular momentum magnitude.

The differential equation for the ascending node (Eq. 2.4) is singular for zero inclination and the differential equations for the argument of perigee (Eq. 2.5) and true anomaly (Eq. 2.6) are singular for zero eccentricity. Although near zero eccentricity and inclination values will not produce strict singularities, these conditions may cause instabilities in numerical integration of geosynchronous object dynamics. A large number of geosynchronous objects possess near zero inclination and eccentricity values. The NORAD database includes geosynchronous objects up to

15 degrees inclination and eccentricity values up to 0.01; however, approximately 70% of tracked geosynchronous objects possess inclinations smaller than 1 degree and 95% possess eccentricities smaller than 0.001.[23]

2.3 Synchronous Elements

The following section defines the synchronous element set and develops nonlinear variational equations for arbitrary orbit perturbations. Small inclination approximations are applied to the equations to simplify the dynamic model, and the resulting variational equations are linearized for the near-zero eccentricity geosynchronous condition.

2.3.1 Definition of Synchronous Elements

The synchronous elements are an approximated version of the equinoctial elements, and are defined as follows in terms of the better-known classical orbital elements.[90]

$$\lambda \triangleq (\omega + \Omega + \nu) - GA(t) \tag{2.7}$$

$$\delta\bar{a} \triangleq \frac{a - A}{A} \tag{2.8}$$

$$e_x \triangleq e\cos(\omega + \Omega) \tag{2.9}$$

$$e_y \triangleq e\sin(\omega + \Omega) \tag{2.10}$$

$$i_x \triangleq i\sin(\Omega) \tag{2.11}$$

$$i_y \triangleq -i\cos(\Omega) \tag{2.12}$$

$$s = \lambda + G(t) \tag{2.13}$$

$$GA(t) = GA_0 + \dot{\Omega}_E(t - t_0) \tag{2.14}$$

The synchronous elements are defined as the Earth-fixed sub-satellite longitude (λ), the longitudinal drift rate ($\delta\bar{a}$), eccentricity vector components (e_x, e_y), and the projection of the angular momentum vector onto the equatorial plane (i_x, i_y). The eccentricity and inclination vector components are depicted in Figs. 2.2(a) and 2.2(b), respectively. The spacecraft sidereal angle, s is defined

by Eq. (2.13). Eq. (2.14) represents the Greenwich sidereal angle at a given time, $\dot{\Omega}_E$ denotes the average Earth rotation rate, and A denotes the nominal geosynchronous semi-major axis of 42164.2 kilometers for an Earth gravitational constant (μ) of 398600.440 kilometers^3 per second^2. Note that the synchronous elements are a non-dimensional representation of the orbital state.

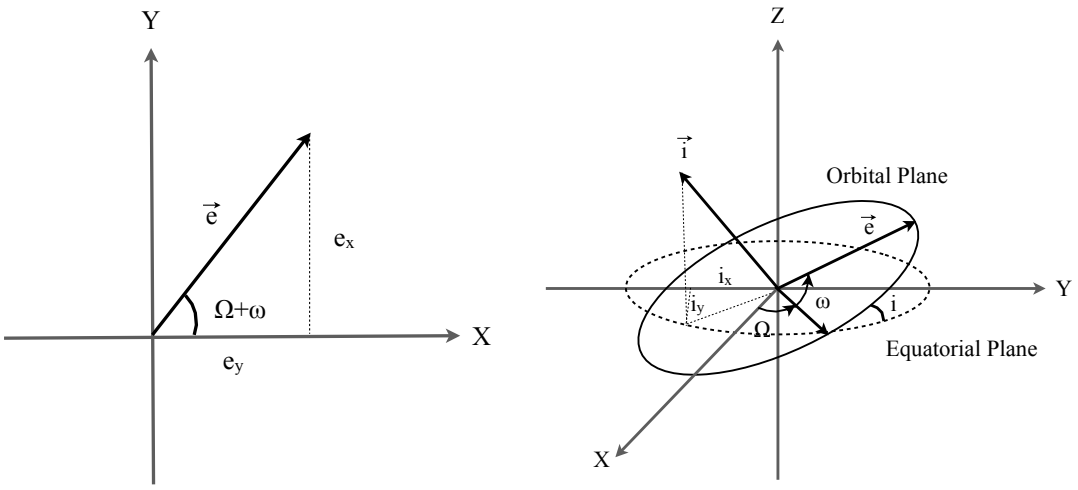

(a) Eccentricity (b) Inclination

Figure 2.2: Eccentricity and Inclination Inertial Vector Components

2.3.2 Development of Nonlinear Variational Equations

The method of Poisson brackets is employed to derive the variational equations for general perturbations. Poisson brackets relate the time rate of change of any orbital element, x, to the contribution of natural orbital motion and the contribution of disturbing forces, $\vec{a}_D$.[11]

$$\frac{dx}{dt} = \frac{\partial x}{\partial \vec{v}} \vec{a}_D + \frac{\partial x}{\partial t} \tag{2.15}$$

Alternately, the differential equations are derived by taking the time derivatives of Eq. (2.7) through (2.12) and substituting the Keplerian element time derivatives. Synchronous element equations of motion have been previously developed via the latter method to model the effects of luni-solar perturbations on inclination and solar pressure on eccentricity.[89; 7]

The full derivation of the nonlinear synchronous element variational equations via Poisson

Brackets is provided in Appendix A. The resulting nonlinear synchronous element variational equations are given in Eq. (2.16) through (2.21), in terms of the body-fixed radial, tangential, and out-of-plane disturbing forces (a_r, a_θ, and a_h).

$$\dot{\lambda} = \frac{h}{r^2} + \frac{r}{h}\tan(\frac{i}{2})\sin(\omega+\nu)a_h - \dot{\Omega}_E \tag{2.16}$$

$$\delta\dot{\bar{a}} = \frac{2(\delta\bar{a}+1)^2}{hA}\left[(e_x\sin(s) - e_y\cos(s))a_r + \frac{p}{r}a_\theta\right] \tag{2.17}$$

$$\dot{e}_x = \frac{r}{h}\left\{\frac{p}{r}\sin(s)a_r + \left[e_x + (1+\frac{p}{r})\cos(s)\right]a_\theta\right\} + e_y\frac{r}{h}\left\{\left[\tan(\frac{i}{2})\sin(\Omega)\cos(s) - \tan(\frac{i}{2})\cos(\Omega)\sin(s)\right]a_h\right\} \tag{2.18}$$

$$\dot{e}_y = \frac{r}{h}\left\{\frac{-p}{r}\cos(s)a_r + \left[e_y + (1+\frac{p}{r})\sin(s)\right]a_\theta\right\} - e_x\frac{r}{h}\left\{\left[\tan(\frac{i}{2})\sin(\Omega)\cos(s) - \tan(\frac{i}{2})\cos(\Omega)\sin(s)\right]a_h\right\} \tag{2.19}$$

$$\dot{i}_x = \left[\frac{r}{h}\sin(\Omega)\cos(\omega+\nu) + \frac{ir}{h\sin(i)}\cos(\Omega)\sin(\omega+\nu)\right]a_h \tag{2.20}$$

$$\dot{i}_y = \left[\frac{ir}{h\sin(i)}\sin(\Omega)\sin(\omega+\nu) - \frac{r}{h}\cos(\Omega)\cos(\omega+\nu)\right]a_h \tag{2.21}$$

in which r is the radial distance of the satellite from the center of the Earth, p is the semi-latus rectum of the orbit, and h is the angular momentum magnitude. These three orbital quantities are expressed in terms of the synchronous elements as follows.

$$r = \frac{A(\delta\bar{a}+1)(1-e_x^2-e_y^2)}{1+e_x\cos(s)+e_y\sin(s)} \tag{2.22}$$

$$p = A(\delta\bar{a}+1)(1-e_x^2-e_y^2) \tag{2.23}$$

$$h = \sqrt{\mu p} \tag{2.24}$$

Though these equations are not truly singular, at very small inclination angles Eq. (2.20) and Eq. (2.21) have the potential for numerical sensitivity due to the $\frac{i}{\sin i}$ terms in Eqs. 2.20 and 2.21.

2.3.3 Small Inclination Approximations

It is desirable to format the synchronous differential equations in a manner such that they provide physical insight into the effects of general perturbations. First, small inclination approximations ($\sin i \approx \tan i \approx i$, $\cos i \approx 1$) are applied to the nonlinear equations.

$$\dot{\lambda} \approx \frac{h}{r^2} + \frac{r}{2h}\left[i_y \sin(s) + i_x \cos(s)\right] a_h - \dot{\Omega}_E \tag{2.25}$$

$$\delta\dot{\bar{a}} \approx \frac{2(\delta\bar{a}+1)^2}{hA}\left[(e_x \sin(s) - e_y \cos(s))a_r + \frac{p}{r}a_\theta\right] \tag{2.26}$$

$$\dot{e}_x \approx \frac{r}{h}\left\{\frac{p}{r}\sin(s)a_r + \left[e_x + (1+\frac{p}{r})\cos(s)\right]a_\theta + \frac{e_y}{2}\left[i_x\cos(s) + i_y\sin(s)\right]a_h\right\} \tag{2.27}$$

$$\dot{e}_y \approx \frac{r}{h}\left\{\frac{-p}{r}\cos(s)a_r + \left[e_y + (1+\frac{p}{r})\sin(s)\right]a_\theta - \frac{e_x}{2}\left[i_x\cos(s) + i_y\sin(s)\right]a_h\right\} \tag{2.28}$$

$$\dot{i}_x \approx \frac{r}{h}\sin(s)a_h \tag{2.29}$$

$$\dot{i}_y \approx -\frac{r}{h}\cos(s)a_h \tag{2.30}$$

Applying the small inclination approximation has the benefit of removing the potential for numerical sensitivity at near-zero inclination.

2.3.4 Small Eccentricity Linearization

The variational equations are now linearized for near-zero eccentricity, an assumption that may be considered for geosynchronous dynamic modeling. Taking the first variation of Eq. (2.25) through (2.30) and simplifying produces the linearized equations shown in Eq. (2.31) through (2.36), in which n denotes the mean motion.

$$\dot{\lambda} \approx -\frac{1}{2}\sqrt{\frac{A(\delta\bar{a}+1)}{\mu}}\left[i_y\sin(s) + i_x\cos(s)\right]a_h + (n - \dot{\Omega}_E) + 2n\left[e_x\cos(s) + e_y\sin(s)\right] \tag{2.31}$$

$$\delta\dot{\bar{a}} \approx \frac{2}{An}\left[1 + e_x\cos(s) + e_y\sin(s)\right]a_\theta + \frac{2}{An}\left[e_x\sin(s) - e_y\cos(s)\right]a_r \tag{2.32}$$

$$\dot{e}_x \approx \sqrt{\frac{A(\delta\bar{a}+1)}{\mu}}\left[\sin(s)a_r + (\cos(s)\left[2 - e_x\cos(s) - e_y\sin(s)\right] + e_x)a_\theta\right] \tag{2.33}$$

$$\dot{e}_y \approx \sqrt{\frac{A(\delta\bar{a}+1)}{\mu}}\left[-\cos(s)a_r + (\sin(s)\left[2 - e_x\cos(s) - e_y\sin(s)\right] + e_y)a_\theta\right] \tag{2.34}$$

$$\dot{i}_x \approx \sqrt{\frac{A(\delta\bar{a}+1)}{\mu}}\left[1 - e_x\cos(s) - e_y\sin(s)\right]\sin(s)a_h \tag{2.35}$$

$$\dot{i}_y \approx \sqrt{\frac{A(\delta\bar{a}+1)}{\mu}}\left[e_x\cos(s) + e_y\sin(s) - 1\right]\cos(s)a_h \tag{2.36}$$

2.4 Hybrid Synchronous and Equinoctial Elements

2.4.1 Definition of GEO Elements

To circumvent the possibility of numerical issues when using the nonlinear synchronous element model, the synchronous inclination terms can be replaced by the equinoctial elements Q_1 and Q_2 defined in Eq. (2.37) and (2.38), producing the specialized GEO element set shown in Eq. (2.39). Like the synchronous elements, the GEO elements are also non-dimensional.

$$Q_1 = \tan(\frac{i}{2})\sin(\Omega) \tag{2.37}$$

$$Q_2 = \tan(\frac{i}{2})\cos(\Omega) \tag{2.38}$$

$$\vec{X} = [\lambda \quad \delta\bar{a} \quad e_x \quad e_y \quad Q_1 \quad Q_2]^T \tag{2.39}$$

2.4.2 Development of Nonlinear Variational Equations

The nonlinear variational equations of the GEO element set are given as:

$$\dot{\lambda} = \frac{h}{r^2} + \frac{r}{h}\left[Q_2\sin(s) - Q_1\cos(s)\right]a_h - \dot{\Omega}_E \tag{2.40}$$

$$\delta\dot{\bar{a}} = \frac{2(\delta\bar{a}+1)^2}{hA}\left[(e_x\sin(s) - e_y\cos(s))a_r + \frac{p}{r}a_\theta\right] \tag{2.41}$$

$$\dot{e}_x = \frac{r}{h}\left\{\frac{p}{r}\sin(s)a_r + \left[e_x + (1+\frac{p}{r})\cos(s)\right]a_\theta + e_y\left[Q_1\cos(s) - Q_2\sin(s)\right]a_h\right\} \tag{2.42}$$

$$\dot{e}_y = \frac{r}{h}\left\{\frac{-p}{r}\cos(s)a_r + \left[e_y + (1+\frac{p}{r})\sin(s)\right]a_\theta - e_x\left[Q_1\cos(s) - Q_2\sin(s)\right]a_h\right\} \tag{2.43}$$

$$\dot{Q}_1 = \frac{r}{2h}(1 + Q_1^2 + Q_2^2)\sin(s)a_h \tag{2.44}$$

$$\dot{Q}_2 = \frac{r}{2h}(1 + Q_1^2 + Q_2^2)\cos(s)a_h \tag{2.45}$$

The derivation of the Q_1 and Q_2 variational equations can be found in Battin [11].

2.5 Physical Insight of Variational Equations

The equations of motion presented in this section have various advantages and disadvantages. The small inclination and small eccentricity linearized synchronous element models are accurate to the first order, but provide greater physical insight than the nonlinear synchronous element model. For example, the approximated models clearly demonstrate that an out-of-plane disturbing force will primarily induce oscillations in the orbit longitude and inclination. This perturbation will also introduce small oscillations to the eccentricity elements, but this effect is minor as it is scaled by small eccentricity and inclination values. No variation in the longitudinal drift rate is induced by an out-of-plane perturbation. To verify these predicted results, a constant out-of-plane disturbing acceleration of 10^{-5} meters per second squared is applied to the nonlinear synchronous element model, which is then numerically integrated for one day. Fig. 2.3 shows the resulting synchronous elements over the one day propagation. For comparison the synchronous elements have been detrended by removing the mean elemental values, which are also shown in the figure, and have been individually scaled by the indicated amount. It is seen that the longitude and inclination terms are dominated by oscillatory behavior, while the eccentricity oscillations are at least 5 orders of magnitude smaller than the mean values. As expected, the drift rate shows no variation. Note that only perturbations that affect the drift rate term will result in an energy change.

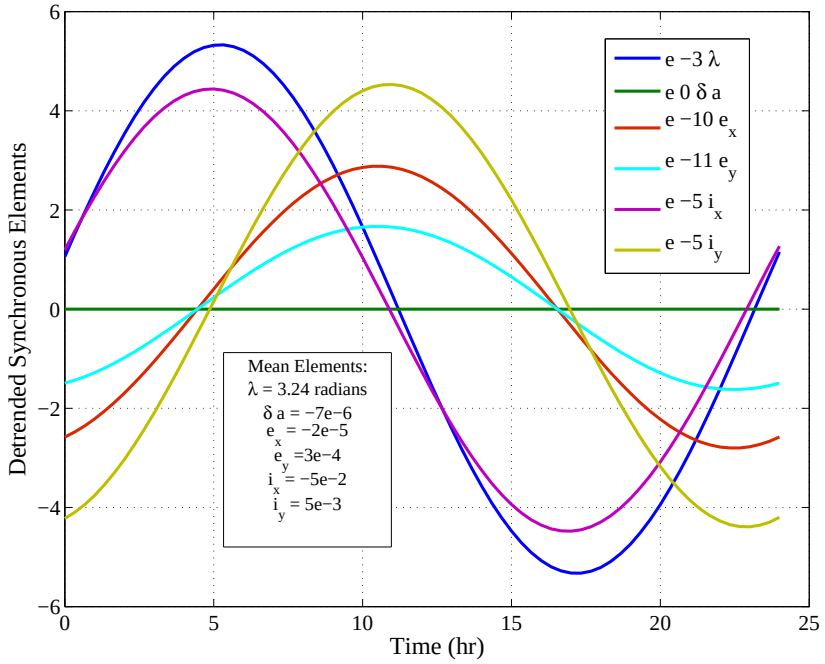

Figure 2.3: Variation in Synchronous Elements Due to a Constant Out-Of-Plane Perturbation

While the approximated models offer physical insight useful in predicting the effect of perturbations or maneuvers on orbital element variation, these models are hindered by the inherent second-order loss of accuracy. The GEO element model is a nonlinear representation of orbital motion with no accuracy loss, and still provides perturbation insight useful for analytical prediction.

2.6 Geosynchronous Orbit Perturbations

Though dominated by two-body gravitational dynamics, natural geosynchronous orbit motion is significantly affected by natural perturbations. The dominant perturbations include solar radiation pressure, Earth oblateness (J_2) and luni-solar point mass gravity.[90] The remaining orbit perturbations, including Earth albedo effects, are negligible in comparison to the dominant perturbations. The effect of solar radiation pressure depends on the position of the object relative to the sun, the sun-facing surface area, the reflectivity of the surface area and the object mass. In practice the object properties are not well known and are often solved for as estimator states. The simulated object motion presented in this chapter does not estimate the solar pressure parameters, but rather models the object as a constant mass, surface area and reflectivity object always oriented directly towards the sun. Also, it is assumed that no solar pressure disturbing force acts upon the object when it is eclipsed by the Earth. A cylindrical Earth shadow model is used to determine whether the object is sunlit or shadowed.

Perturbations due to high-order Earth gravity field harmonics are approximately two orders of magnitude smaller than the dominant disturbing forces[99]; however, certain harmonics accumulate to significant levels due to geosynchronous object resonance.[42] The non-uniform Earth mass distribution leads to a longitude-dependent tangential force that is sinusoidal in profile, meaning that there are four nodes of maximum or minimum acceleration. Two of the nodes, at approximately 75.1 degrees East and 105.3 degrees West longitudes, are stable equilibrium points. An undisturbed spacecraft at rest at the stable node will remain at this location for all time.[90] Two unstable nodes exist at 11.5 degrees West and 161.9 degrees East longitudes; an unperturbed spacecraft at rest at one of these two nodes will drift away from this point in either direction. Due to

the presence of the stable longitudes, a geosynchronous object can be in resonance with the Earth's rotation, which causes the influence of the tangential gravitational force to be non-negligible. The tangential gravitational force is dominated by terms of degree and order two (J_{22}), and causes longitudinal drift through the geosynchronous orbit.

2.7 Analysis of General Perturbation Dynamic Model

It is necessary to analyze the applicability of synchronous and GEO element dynamic modeling of geosynchronous motion under general perturbations. The model precision is tested by assessing the propagation consistency when numerically integrating with both large and small fixed time steps. The model accuracy is tested by evaluating the consistency of propagations using different coordinate representations.

2.7.1 Dynamic Model Accuracy Analysis

In order to analyze the accuracy of the equations of motion for the synchronous and GEO elements, the synchronous propagation for a fixed time-step of 60 seconds is compared to a reference propagation. The reference propagation is computed by numerically integrating inertial Cartesian elements with a variable step 5^{th}-order Runge-Kutta numerical integrator with an accuracy tolerance of 10^{-12} meters and meters per second. Fixed step propagation of the inertial Cartesian, Keplerian, GEO, nonlinear synchronous, small inclination approximated synchronous, and small eccentricity linearized synchronous equation of motion are compared to the variable step reference propagation.

The initial conditions and physical satellite parameters shown in Table 5.1, identical for each propagation, are taken from the TDRS 8 Osculating Element set for July 2, 2005.[4] The satellite physical characteristics include the spacecraft surface area, mass, and the reflectivity, C_r. A fifth-order Runge-Kutta fixed-step integrator is chosen to provide a direct comparison among the coordinate representation propagations. The integrated equations of motion include two-body dynamics, Earth oblateness, luni-solar gravity and solar pressure perturbations. The solar pres-

sure acceleration is modeled assuming that the satellite is spherical and that no solar pressure perturbation acts on the satellite when it is shadowed by the Earth.

Table 2.1: Simulation Initial Conditions and Satellite Characteristics

Epoch	2 July 2005 0:0:0 UTC
a (km)	42163.9203
e	0.00027562
i (deg)	2.6491
Ω (deg)	263.9230
ω (deg)	189.3889
M (deg)	12.5343
Surface Area (m^2)	65.65
Mass (kg)	1733.4973
C_r	1.38251

Fig. 2.4 displays the differences between each propagation and the reference propagation. The inertial Cartesian, Keplerian, nonlinear synchronous, and GEO propagations are nearly identical. The errors of these propagations are on the order of 10^{-7} to 10^{-6} meters in position and 10^{-11} to 10^{-10} meters per second in velocity. The error consistency indicates that the nonlinear nonlinear synchronous element and GEO element dynamic models are as accurate as the more traditional Keplerian and inertial position and velocity dynamic models. Furthermore, the small errors from the reference orbit indicate that a 60 second time-step is appropriate for fixed step numerical propagation of geosynchronous orbits.

Fig. 2.4 also presents the propagation error for the small inclination synchronous model. The small inclination propagation errors are approximately 10^{-4} to 1 meters in position and 10^{-9} to 10^{-5} meters per second in velocity. The initial inclination for this simulation is approximately 2.5 degrees. Additional studies are performed in which the initial inclination is decreased by one order of magnitude, which produces propagation error on the same order of magnitude as the

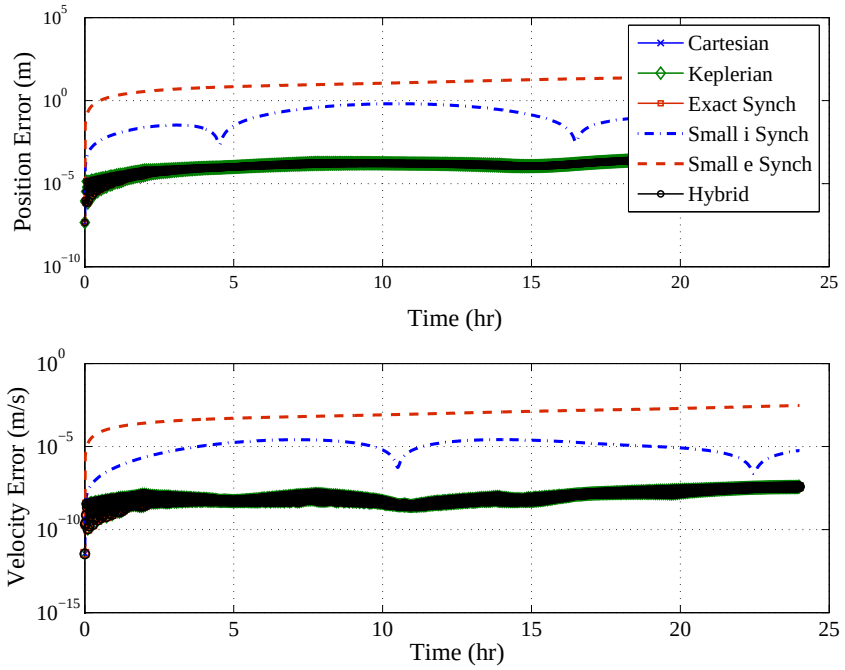

Figure 2.4: Error Relative to Reference Propagation

nonlinear synchronous elements. Of the current Space Track database, approximately 70% of the geosynchronous satellites currently tracked by NORAD are at inclinations of 1 degree or smaller.[23]

The figure also presents the error for the small eccentricity dynamic model. The error is on the order of 1 to 100 meters in position, and 10^{-5} to 10^{-3} meters per second in velocity. The linearization error will decrease if the eccentricity is smaller than the value used in this study ($e = 0.00027562$). However, an evaluation of the Space Track database reveals that only approximately 7.5% of the currently-track geosynchronous satellites have eccentricity values on the order of 10^{-5} or smaller.

2.7.2 Dynamic Model Precision Analysis

The integration time-step for geosynchronous propagation should be carefully chosen, as time steps that are too large lose dynamic fidelity while time steps that are too small may accumulate errors in the case of small perturbations due to limited numerical precision. The dynamics of a geosynchronous object are such that a set of elements that changes slowly over time is better suited for modeling than an element set that changes more dynamically. With an appropriate element set, long integration time steps adequately capture the motion.

The precision study is conducted by integrating a set of initial conditions four separate times, each with a different integration time-step. The time steps chosen for this study are 1 second, 6 seconds, 60 seconds, and 600 seconds. Inertial Cartesian, Keplerian, nonlinear synchronous and GEO elements are propagated via a fixed-step numerical integrator for each of the time steps listed. The differences between the propagated orbits of a given element set are a direct measure of the integration consistency. All propagated state differences are expressed in inertial Cartesian coordinates for comparison. For each coordinate representation, the 1 second, 6 seconds, and 600 seconds fixed time-step propagations are differenced from the 60 second propagation. The 60 second propagation is chosen as the reference as the accuracy analysis showed that the inertial, Keplerian, GEO and nonlinear synchronous element models are nearly identical at this fixed time step.

A dynamic model that is not sensitive to time-step size is clearly preferable for computational purposes. It is expected that the Cartesian model will be sensitive to the time-step as the elements are very large compared to their dynamic changes. The synchronous, GEO and Keplerian models are not expected to exhibit either inconsistent or increasing propagation error. The initial conditions, shown in Table 5.1, have been chosen such that the Keplerian equations of motion will not encounter singularities.

First, the inertial Cartesian model precision is analyzed. Fig. 2.5 presents the 1 second, 6 seconds, and 600 seconds inertial Cartesian position and velocity propagations each differenced from the 60 second propagation. The figure, which is presented on a log scale, shows that the differences change by orders of magnitude, indicating that the Cartesian propagation is not very consistent as the step size is increased from 1 second to 600 seconds. The 600 second propagation shows the largest differences, on the order of 10^{-2} meters and 10^{-6} meters per second. The differences of the 1 second propagation (10^{-7} to 10^{-5} meters in position, 10^{-11} to 10^{-10} meters per second in velocity) compared to that of the 6 second propagation (10^{-8} to 10^{-6} meters in position, 10^{-12} to 10^{-11} meters per second in velocity) indicate that the Cartesian integrator also encounters numerical issues when the time-step is too small. This is likely because the elemental variations due to perturbations is small in comparison to the dominant two-body dynamics for a geosynchronous satellite. This causes the perturbation effects to be lost through limited numerical precision.

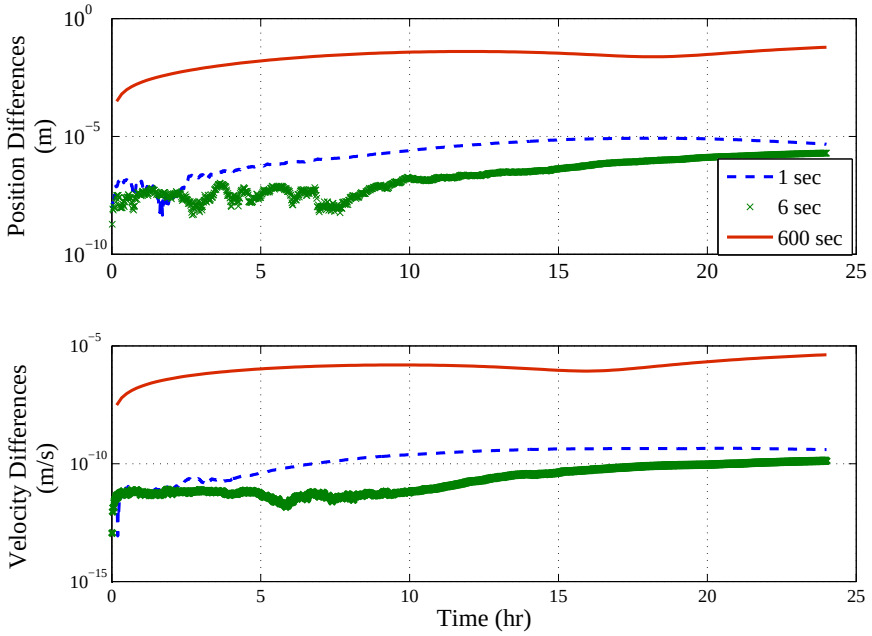

Figure 2.5: Inertial Cartesian Model Differences Relative to 60 Second Fixed Time-Step Propagation

Fig. 2.6 displays the propagation differences for the Keplerian precision analysis. The propagation differences are on the order of 10^{-7} to 10^{-5} meters in position and 10^{-11} to 10^{-9} meters per second in velocity for all cases, showing that the Keplerian model is less dependent on time-step size than the Cartesian model. Again the 1 second time-step presents the largest differences, indicating that numerical issues may exist at smaller integration steps. An additional study, in which the initial eccentricity is decreased by one order of magnitude and the precision analysis repeated, investigates the Keplerian element modeling of a satellite in a less eccentric orbit. The propagation differences are shown in Fig. 2.7. The results show that for large time steps (600 s econds) near zero eccentricity values produce offsets and discontinuities in the propagation differences due to the singularities of the Keplerian element equations of motion.

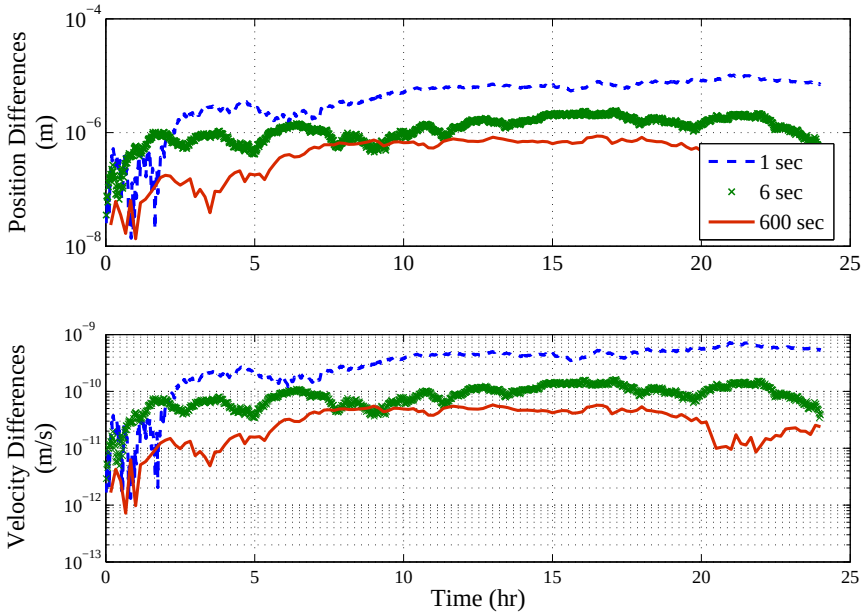

Figure 2.6: Keplerian Model Differences Relative to 60 Second Fixed Time-Step Propagation

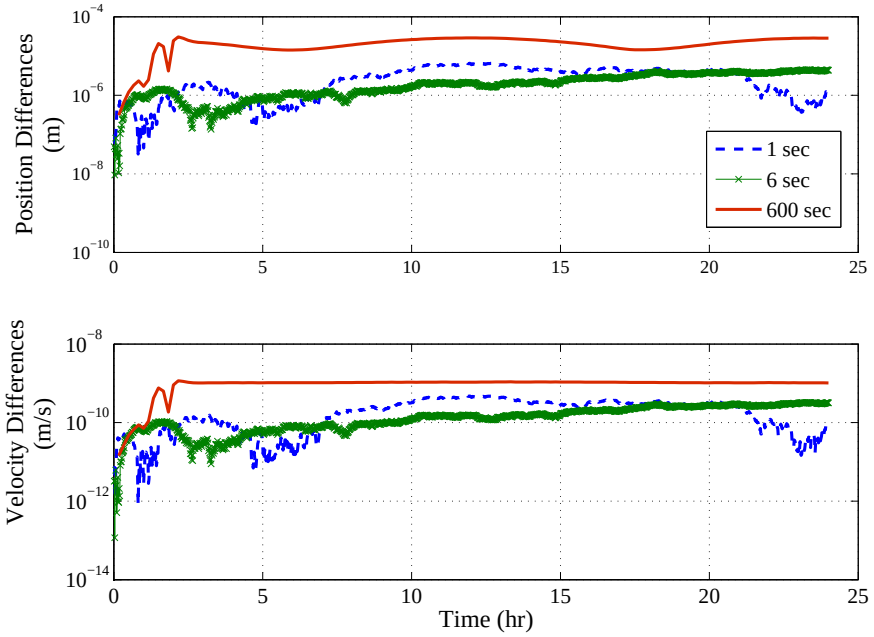

Figure 2.7: Keplerian Model Differences Relative to 60 Second Fixed Time-Step Propagation - Near Zero Eccentricity

The 1 second, 60 second, and 600 second fixed time-step propagation differences for the nonlinear synchronous element model are shown in Fig. 2.8. The differences are consistent on the order of 10^{-7} to 10^{-6} meters in position and 10^{-11} to 10^{-10} meters per second in velocity. This result is expected as the synchronous elements are designed to change by a small amount, and the singularity in the inclination component equations of motion is largely cancelled out for small inclinations. In contrast to the Cartesian and Keplerian studies, the 1 second propagation differences are the same order of magnitude as the 6 second propagation differences. However, the differences grow slowly over time, indicating that there is still a numerical issue that arises with small time steps.

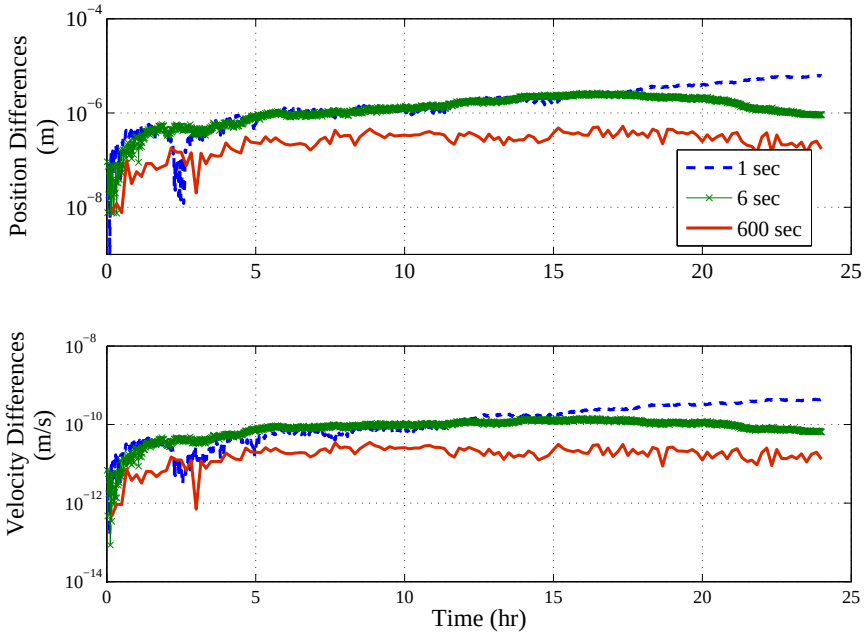

Figure 2.8: Synchronous Model Differences Relative to 60 Second Fixed Time-Step Propagation

Fig. 2.9 presents the differences of the 1 second, 6 second, and 600 second fixed time-step GEO element propagation from the 60 second propagation. The results are similar to those of the synchronous element model; the position and velocity differences are consistent to approximately one order of magnitude. The position difference is approximately 10^{-6} to 10^{-7}meters, while the

velocity difference is approximately 10^{-11} to 10^{-10} meters per second. As seen for the inertial Cartesian and Keplerian propagations, the GEO element 1 second propagation differences are slightly larger than that of the 6 second and 600 second propagations.

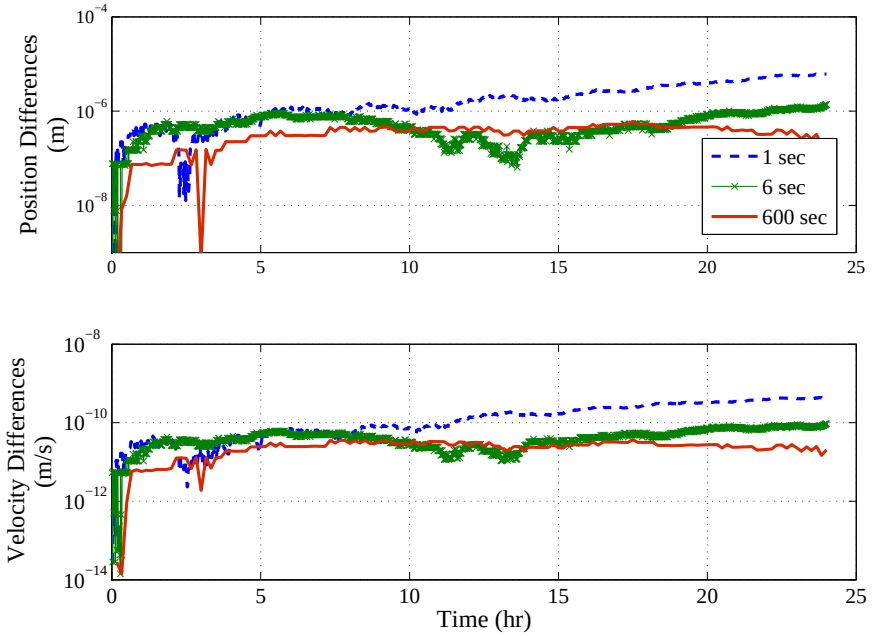

Figure 2.9: GEO Model Differences Relative to 60 Second Fixed-time-step Propagation

2.7.3 Conclusions

The numerical propagation study indicates that the time interval for a geosynchronous fixed-step 5^{th}-order Runge-Kutta numerical integrator must be chosen with care, as time steps that are too small (1 second) or too large (600 seconds) may introduce numerical issues. It must be noted that the accuracy of a higher-order fixed-step numerical integrator will not be as sensitive to time-step size, and that a variable step integrator will alter the time steps in order to meet a desired integration tolerance. Large time steps are suitable for synchronous and GEO element propagation. Small integration time steps are computationally expensive and are not generally useful for geosynchronous orbit propagation.

Comparison of various element-set propagations reveals that the nonlinear differential equa-

tions for the synchronous and GEO elements are as accurate as Keplerian and Cartesian geosynchronous propagations. However, the small inclination and eccentricity approximated synchronous equations of motion for the synchronous elements are not accurate enough for precise applications where sub-meter accuracy is required. Given their simplicity, the approximated synchronous differential equations may be suitable for applications with loose accuracy requirements such as mission planning. Furthermore, the simplified dynamic model provides physical insight into the effect of general perturbations. Given that the nonlinear synchronous equations necessary for high accuracy dynamic modeling can suffer from numerical sensitivity, there is no added benefit in using the synchronous elements over the equinoctial elements.

Based on the results of the numerical propagation analysis, the hybrid set of synchronous and equinoctial elements shown in Eq. (2.39) is chosen to accurately model the dynamics while avoiding potential singularities.

Chapter 3

Geosynchronous Orbit Estimation

3.1 Introduction

Orbit estimation is the process of determining the statistically most probable spacecraft state based on imperfect observations of the spacecraft and imperfect models of the spacecraft motion. Orbit estimation can be generally divided into two categories: batch processing and sequential filtering. Batch estimation algorithms process a time history of observations as a set to determine the spacecraft state and associated state uncertainty at an epoch time. In contrast, sequential filtering processes individual observations in order to determine the spacecraft state and uncertainty at the time of each observation. This chapter provides an overview of the least squares batch processor and Kalman filter sequential estimation algorithms. The batch processor, conventional Kalman filter, Extended Kalman filter, and smoothing algorithms presented in this chapter are all referenced from Tapley, Born and Schutz [94]. The Unscented Kalman Filter is referenced from Julier and Uhlman [36].

3.2 Batch Estimation

Batch least squares estimation, also referred to as differential correction, is typically used as a post-processing estimation tool as all available data are batch processed to determine the epoch estimate. A reference spacecraft state is propagated from the epoch time throughout the measurement period and predicted observations of the spacecraft computed. The difference between predicted observations and experimental measurements are referred to as observation residuals; the

least squares solution is the spacecraft state that minimizes the weighted sum of the squares of the observation residuals. This solution is used to update the reference state and the batch least squares is iterated until a defined convergence tolerance is met.

3.2.1 Batch Estimation Advantages and Disadvantages

An advantage to the batch processor is that the epoch solution can be mapped to any other time within the observation period. Additionally, the algorithm is generally robust to imperfect initial conditions and noisy data, producing a solution that is generally more accurate than that of a sequential estimator. Disadvantages include the fact that the estimated epoch state uncertainty cannot be accurately mapped through time, and the batch estimator may not converge if the initial reference orbit is too far from the truth orbit. Finally, the estimated covariance may be unrealistically small if a large number of observations are processed.

3.2.2 Weighted Least Squares Batch Estimator

This section presents the algorithm for the weighted least squares batch estimator. The batch estimator is initialized as shown in Eqs. 3.1 through 3.2, in which $\vec{X}^*$ denotes the reference state vector, t_i is the time at the i^{th} index, $\Phi(t_{i-1}, t_0)$ is the state transition matrix between epoch time t_0 to t_{i-1}, and I is the identity matrix. If *a priori* information is available (state covariance, $\bar{P}_0$, and state deviation, $\bar{x}_0$), the batch normal equations are initialized as shown in Eq. 3.2; if no *a priori* information is available the equations are initialized at zero.

$$i = 1, t_{i-1} = t_0, \vec{X}^*(t_{i-1}) = \vec{X}_0^*, \Phi(t_{i-1}, t_0) = \Phi(t_0, t_0) = I \tag{3.1}$$

$$\Lambda = \bar{P}_0^{-1}, N = \Lambda \bar{x}_0 \tag{3.2}$$

The reference state vector is propagated via integration of the dynamic model, $F(\vec{X}, t)$, to the time of the first observation at t_i. The state transition matrix is also numerically integrated as governed by Eq. 3.4.

$$\dot{\vec{X}}^* = F(\vec{X}^*(t), t) \tag{3.3}$$

$$A(t) = \frac{\partial F(\vec{X}^*, t)}{\partial \vec{X}^*}, \dot{\Phi}(t, t_0) = A(t)\Phi(t, t_0) \tag{3.4}$$

The observation at time t_i is assimilated into the batch solution as follows. The predicted measurement, $\vec{C}_i$, and measurement sensitivity matrix, $\tilde{H}_i$, are evaluated as shown in Eqs. 3.5 and 3.6, in which $G(\vec{X}, t)$ represents the observation model. The observation residual, $\vec{y}_i$, is the difference between the experimental and predicted measurements (Eq. 3.7). The measurement sensitivity matrix is mapped back to the epoch time (H_i).

$$\vec{C}_i = G(\vec{X}_i^*, t_i) \tag{3.5}$$

$$\tilde{H}_i = \frac{\partial G(\vec{X}^*, t)}{\partial \vec{X}^*} \tag{3.6}$$

$$\vec{y}_i = \vec{O}_i - \vec{C}_i \tag{3.7}$$

$$H_i = \tilde{H}_i \Phi(t_i, t_0) \tag{3.8}$$

The normal equations are then accumulated to include the i^{th} observation, as shown in Eqs. 3.9 and 3.10, in which W represents the measurement weighting matrix. The weighting matrix is the inverse of the measurement noise matrix, R.

$$\Lambda = \Lambda + H_i^T W H_i \tag{3.9}$$

$$N = N + H_i^T W \vec{y}_i \tag{3.10}$$

If observations remain to be processed, the time index i is set to $i = i + 1$, and Eqs. 5.30 through 3.10 are repeated. Once the final observation has been processed, the normal equations are solved to produce estimates for the epoch state deviation vector ($\hat{x}_0$) and the state covariance (P_0). The solution is used to update the epoch reference state and *a priori* information, as shown in Eqs. 3.11 and 3.12, and the entire batch process is iterated until a chosen convergence tolerance is met.

$$\Lambda \hat{x}_0 = N, P_0 = \Lambda^{-1} \tag{3.11}$$

$$\vec{X}_0^* = \vec{X}_0^* + \hat{x}_0, \bar{x}_0 = \bar{x}_0 - \hat{x}_0 \tag{3.12}$$

A disadvantage of the least squares batch estimator is that it does not easily allow for the inclusion of dynamic process noise. Process noise accounts for unmodeled dynamics acting on the spacecraft, but only enhances the estimator performance if the unmodeled dynamics are randomly distributed. Process noise can be incorporated into the batch algorithm through the weighting matrix, given that the process noise statistical distribution and propagation are known[73]. If not well characterized, these parameters may be tuned to produce the desired estimator performance.

3.3 Sequential Filtering

In contrast to the batch least squares algorithm, sequential filtering estimates the state and uncertainty at the time of each observation. Like the batch algorithm, the best estimate is that which minimizes the observation residuals in a least squares sense. The conventional Kalman filter updates the reference state until all observations have been processed, and the sequential filter is iterated until the solution convergence criteria is met.

3.3.1 Sequential Filtering Advantages and Disadvantages

Sequential filters are typically used for real-time data processing applications, and have certain advantages over batch processing. It is relatively simple to include tunable dynamic process noise in the covariance propagation, which mitigates filter saturation when processing a large number of observations. Additionally, the state and uncertainty estimates are valid at each observation time. However, there are disadvantages to the sequential filter: the state estimates cannot be accurately propagated forward or backward as the solution at time t_i depends on the number of measurements processed up to that time, and the filter measurement update is sensitive to noisy data. Furthermore, if the covariance collapses, the sequential algorithm will cease incorporating observation residuals into the solution. Because of the observations are processed in order, the estimate at the end of the tracking period is generally more accurate than that at the beginning. Like the batch processor, the conventional Kalman filter is a linearized system and may not converge for all initial conditions. Note that these disadvantages can be mitigated via modified algorithms

that will be discussed throughout this chapter.

3.3.2 Kalman Filter

The conventional Kalman filter assumes that an *a priori* reference state, error, and uncertainty are available at some epoch time. The filter is initialized to set the epoch estimated state deviation and uncertainty to the *a priori* values as shown in Eq. 3.13. As in the batch algorithm, the epoch reference state and state transition matrix are propagated to the time of the first observation (Eqs. 5.30 through 3.4). The *a priori* state deviation and state covariance matrix are propagated as shown by Eq. 3.14 and 3.15, in which Q and Γ represent the process noise covariance and transformation matrices, respectively. This step is typically referred to as the time update.

$$i = 1, t_{i-1} = t_0, \vec{X}^*(t_{i-1}) = \vec{X}_0^*, \hat{x}_{i-1} = \bar{x}_0, P_{i-1} = \bar{P}_0 \tag{3.13}$$

$$\bar{x}_i = \Phi(t_i, t_{i-1})\hat{x}_{i-1} \tag{3.14}$$

$$\bar{P}_i = \Phi(t_i, t_{i-1})P_{i-1}\Phi(t_i, t_{i-1})^T + \Gamma(t_i, t_{i-1})Q_{i-1}\Gamma(t_i, t_{i-1})^T \tag{3.15}$$

The predicted measurement, observation residual, and measurement sensitivity matrix are computed as shown in Eqs. 3.5 through 3.7; additionally, the Kalman gain value, K, is computed (Eq.3.16). Next, the measurement update is performed. The state deviation and covariance estimates at time i are updated as shown in Eq. 3.17 and 3.18. Note that the estimated covariance matrix formulation shown is prone to numerical issues with finite computational precision; this can be mitigated by using alternate formulations of the covariance matrix measurement update.

$$K_i = \bar{P}_i\tilde{H}_i^T(\tilde{H}_i\bar{P}_i\tilde{H}_i^T + R_i)^{-1} \tag{3.16}$$

$$\hat{x}_i = \bar{x}_i + K_i(\vec{y}_i - \tilde{H}_i\bar{x}_i) \tag{3.17}$$

$$P_i = (I - K_i\tilde{H}_i)\bar{P}_i \tag{3.18}$$

After processing the observation at time t_i, the *a priori* values of $\bar{x}_i$ and $\bar{P}_i$ are set to the estimated quantities $\hat{x}_i$ and P_i, and Eqs. 3.14 through 3.18 repeated to input the next observation

until all observations are processed. For a nonlinear system, the entire sequential process may be iterated until a convergence criteria is reached; in this case the reference orbit is updated after each iteration of the Kalman filter.

3.3.3 Extended Kalman Filter

The Extended Kalman filter follows the algorithm for the conventional Kalman filter up to the measurement update, at which point the reference orbit ($\vec{X}^*$) is updated at each observation time by the estimated state deviation as shown by Eq. 3.19. It follows that the *a priori* state vector deviation is set to zero for all time. In this manner, the Extended Kalman filter is more robust to initial conditions that are outside of the linearity region of the Kalman filter algorithm.

$$\vec{X}_i^* = \vec{X}_i^* + \hat{x}_i \tag{3.19}$$

3.3.4 Filter Smoothing

The estimated state and uncertainty produced by the conventional or Extended Kalman filters are generally not as accurate as those of a batch processor because sequential algorithms are more susceptible to observation noise. However, this issue can be mitigated by applying a filter smoother after convergence of the Kalman filter. A smoother is a method of time-series processing which reduces the impact of noise on the solution.

The filter smoother determines the state estimate at time t_i that maximizes the state conditional probability based on all observations through time t_k, where $k > i$. This recursive algorithm sequentially updates the state deviation estimate backwards throughout the tracking period. Assuming the state estimates, pre- and post-measurement update covariance matrices and state transition matrices are known at all observations times, the filter smoother steps backwards from the total number of observations, N, to the first observation as shown by Eqs. 3.20 and 3.21, in which a quantity x_i^k indicates the value of x at time t_i given observations through time t_k.

$$S_{k-1} = P_{k-1}^{k-1}\Phi^T(t_k, t_{k-1})(P_k^{k-1})^{-1} \tag{3.20}$$

$$\hat{x}_{k-1}^{k} = \hat{x}_{k-1}^{k-1} + S_{k-1}\left[\hat{x}_{k}^{k} - \Phi(t_k, tk-1)\hat{x}_{k-1}^{k-1}\right] \tag{3.21}$$

3.3.5 Unscented Kalman Filter

Another formulation of sequential filtering is the Unscented Kalman filter which uses nonlinear sigma point propagation as the filter time update.[36] A discretely sampled set of points, with mean equal to the *a priori* state and standard deviation equal to the *a priori* uncertainty, is propagated via a nonlinear dynamic model. The propagated set of points is then statistically assessed to determine the new predicted state (the weighted mean of the propagated sample) and the predicted state covariance (the weighted distribution of the sample). The propagated state sample is then transformed into a sample of measurements. The sample measurement mean is used to compute the predicted measurement and therefore the observation residual. The measurement update is performed in a manner similar to that of the conventional Kalman filter.

By parameterizing the mean and covariance in this manner, the Unscented Kalman filter is not hindered by linearization issues that affect the Kalman filter time update and the estimates are accurate to second order. Like the Kalman filter, the nonlinear propagation allows for inclusion of process noise; however, the Unscented Kalman filter algorithm is not restricted to assuming a Gaussian noise distribution. The Unscented, conventional and Extended Kalman filters demonstrate similar performance for linear and near-linear systems, but the Unscented Filter outperforms both the conventional and Extended Kalman filters for nonlinear dynamic systems.[36]

3.4 Covariance Matrix

The single most importance piece of information output by an estimator may be the state error covariance matrix. The covariance matrix contains information regarding the quality of the estimated state. This is particularly useful for the general case in which the true spacecraft trajectory is unknown, and the estimation error cannot be assessed by comparing the recovered orbit to a reference orbit. The covariance matrix provides a metric for the expected performance of the estimator and indicates the level of confidence to which the orbit is known. Furthermore,

the covariance matrix may be analyzed to determine which estimated parameters are limiting the orbit knowledge, as well as how the state errors are correlated to one another and how this may affect the estimation accuracy.

3.4.1 Covariance Matrix Components

The covariance matrix comprises the variances of the estimated state error distribution and the correlations between the state error distributions. An example covariance matrix is given by:

$$P = \begin{bmatrix} \sigma_\alpha^2 & \rho_{\alpha\beta}\sigma_\alpha\sigma_\beta \\ \rho_{\alpha\beta}\sigma_\alpha\sigma_\beta & \sigma_\beta^2 \end{bmatrix} \tag{3.22}$$

in which α and β represent the estimated states, the variances (1σ standard deviation) of the state errors are denoted by σ_α and σ_β, and the correlation coefficient is $\rho_{\alpha\beta}$. The correlation coefficient, a value between positive and negative 1, represents the level of linearity between the estimated state errors ($|\rho_{\alpha\beta}| = 1$ indicates a linear relationship). In general, parameters that are highly correlated can be less accurately estimated.

3.4.2 Representation of Uncertainty Distribution

Given n estimated states, the covariance matrix represents an n-dimensional uncertainty distribution in the estimated state space. This uncertainty distribution is commonly referred to as the "error ellipsoid" or "uncertainty ellipsoid" for a three-dimensional state. Information about the size and orientation of the error ellipsoid is contained within the covariance matrix; the size of the uncertainty ellipsoid along each state axis is dictated by the error variances and the orientation of the principal axes with respect to the state frame is governed by the correlation coefficients. If there is no correlation between the states, the uncertainty distribution will be oriented such that all principal axes lie in the direction of the states. Non-zero correlation effectively rotates the error ellipsoid relative to the state frame.

An example of a three-dimensional error ellipsoid defined in the orthogonal RIC (Radial, In-track, Cross-track) reference frame is given by Eq. 3.23 and shown in Figure 3.1. The uncertainties in

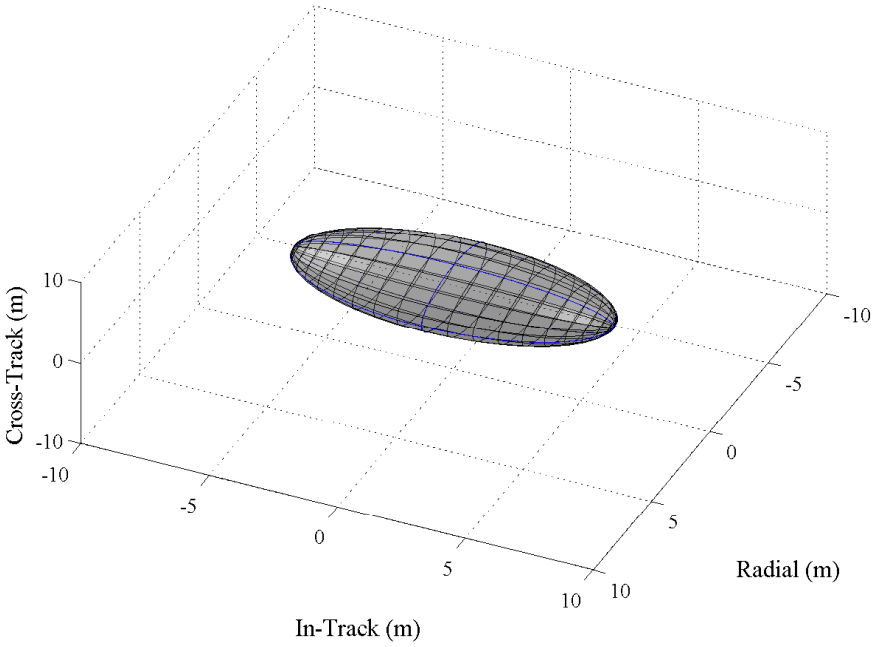

Figure 3.1: Example RIC Frame Error Ellipsoid ($\rho_{RI} = \rho_{RC} = \rho_{IC} = 0$)

each of the three directions are approximately 2.80 meters, 6.25 meters and 2.80 meters, respectively, and all correlation coefficients are zero. The gray ellipsoid represents the uncertainty distribution, and the blue lines represent its projection onto the RIC axes. Note that the ellipsoid is elongated along the in-track direction due to the larger in-track uncertainty, and is oriented such that the principal axes are aligned with the RIC frame due to the uncorrelated state errors.

$$P_1 = \begin{bmatrix} 7.8 & 0 & 0 \\ 0 & 39.0 & 0 \\ 0 & 0 & 7.8 \end{bmatrix} \tag{3.23}$$

To illustrate the frame rotation governed by the correlation between state errors, the covariance matrix given by Eq. 3.23 is now altered such that the radial and in-track correlation correlation is 0.8, as shown in Eq. 3.24. The resulting error ellipsoid is shown in Fig. 3.2. The error ellipsoid has been elongated and rotated about the cross-track axis. A method to compute the ellipsoid size and the rotation of the principal axes relative to the state frame via an eigendecomposition

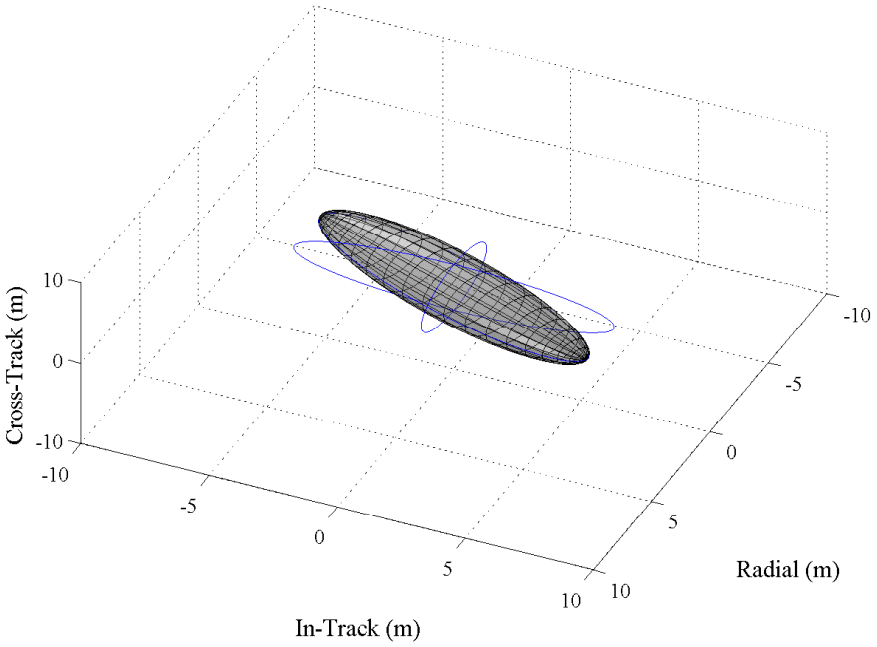

Figure 3.2: Example RIC Frame Error Ellipsoid ($\rho_{RI} = 0.8, \rho_{RC} = \rho_{IC} = 0$)

technique may be found in Reference [94].

$$P_2 = \begin{bmatrix} 7.8 & 14 & 0 \\ 14 & 39.0 & 0 \\ 0 & 0 & 7.8 \end{bmatrix} \tag{3.24}$$

3.4.3 Covariance Matrix Transformation

It is at times useful to assess the covariance matrix in state spaces other than that of the estimated parameters. Two examples of the neccessity for such transformations are now given. First, the uncertainty as expressed in the orbit RIC frame may provide insight into the system dynamics that is not detectable when the uncertainty is expressed in the Earth-Centered Inertial (ECI) frame. For example, large uncertainty in the in-track direction may indicate mismodeling of the perturbing drag force, which must then be corrected in order to recover a more accurate orbit estimate. Secondly, it may be desirable to compare the covariance matrices produced by estimation in various state spaces, for example, in order to assess how linearization affects the solution. In

order to compare the error ellipsoids, all covariance matrices must be transformed into a common element set.

The covariance matrix may be mapped between coordinate systems via linear or nonlinear transformations. The general linear transformation from coordinate set A to coordinate set B is as follows:[94]

$$P_B = \frac{\partial B}{\partial A} P_A \frac{\partial B}{\partial A}^T \tag{3.25}$$

This linear mapping is advantageous for simple linear systems in which the linearization of coordinate set B with respect to coordinate set A does not significantly misconstrue the relationship between the two state spaces. However, linearly transforming the covariance matrix will introduce large errors when the relationships between the state spaces are highly nonlinear.

Another covariance mapping option which maintains the accuracy of the covariance matrix given linear or nonlinear coordinate transformations is the sigma-point method. An arbitrary truth set of elements in coordinate frame A is selected ($\vec{A}_0$), and n number of deviated sets are created by perturbing the truth set by random values ($\vec{q}_n$) within the variance limit. Assuming a Gaussian uncertainty distribution, the random values are normally distributed with zero mean and a standard deviation of 1. Each deviated set is given by:

$$\vec{A}_p = \vec{A}_0 + \sigma_A \vec{q}_p, p = 1, 2, 3....n \tag{3.26}$$

As governed by the Central Limit Theorem, the distribution of the deviated sets approaches a Gaussian distribution as n approaches infinity.[94]

The truth coordinate set $\vec{A}_0$ is transformed via the exact nonlinear mapping to the B state space to form the truth set $\vec{B}_0$. Each set of deviated states is also transformed via the nonlinear mapping to create a set of deviated state vectors in the B frame ($\vec{B}_p$). The covariance as expressed in the B frame is then computed as follows:

$$\vec{\epsilon}_p = \vec{B}_p - \vec{B}_0 \tag{3.27}$$

$$P_B = \sum_{p=1}^{n} \vec{\epsilon}_p \vec{\epsilon}_p^T \tag{3.28}$$

3.4.4 Eigendecomposition of the Covariance Matrix

When analyzing the physical significance of a fully-populated matrix, it is often useful to break the matrix down into its eigenvectors and eigenvalues, a process known as eigendecomposition. The benefit of eigendecomposition is that the covariance matrix can be represented as a diagonal matrix in the eigenvector frame, and provides insight into the size and shape of the uncertainty distribution regardless of the coordinate set in which the covariance matrix is expressed. Note that the eigenvectors will constitute an orthogonal set because the covariance matrix is symmetric.

The scale and orientation of the error uncertainty distribution can be assessed via the eigenvalues and eigenvectors of the covariance matrix, respectively. The eigenvectors represent how the principal directions of the uncertainty distribution are aligned relative to the state frame, and the principal angle of rotation is computed from the normalized eigenvectors.[94] The eigenvalues represent the level of uncertainty along the corresponding principal axes. The general shape of the uncertainty distribution can be determined from this information. For example, a three-dimensional football-shaped distribution will have two eigenvalues of similar magnitudes, and a third maximum eigenvalue.

The technique of eigendecomposition is particularly useful for straightforward comparison of uncertainty distributions within a given element space. The eigenvalues may be directly compared to determine how the scale of multiple uncertainty distributions compare with one another. The eigenvectors may be used to easily compare the orientation of the distributions; computing the dot product of corresponding eigenvectors, such as the eigenvectors representing the semi-major axes of two error ellipsoids, reveals how closely aligned those unit vectors are. Dot products that are positive or negative 1 indicate that the eigenvectors are parallel, while dot products that are zero indicate that the eigenvectors are orthogonal.

Eigendecomposition of the covariance matrix may also be useful in the analysis of error ellipsoid evolution as it is propagated over time. A covariance matrix defined as a sphere may not remain that way as the dynamics of the system are propagated; in the general orbit case, the

uncertainty ellipsoid inflates in all directions and elongates along the velocity vector. Inspecting the evolution of the eigenvalues and eigenvectors over time may reveal information regarding the manner in which the system dynamics affect the state error uncertainties, taking into account the three-dimensional scale and orientation of the full error ellipsoid.

3.5 Geosynchronous Estimation Algorithm

Based on an assessment of the advantages and disadvantages of the described estimation algorithms as well as the behavior of geosynchronous object motion and ground-based observations of geosynchronous objects, the weighted least squares batch estimator is chosen for this work. The least squares batch processor is well suited to near-linear dynamic motion and observation models; perturbed geosynchronous dynamics have been demonstrated to be slowly varying when expressed by the GEO elements, and Earth-fixed optical observations do not vary significantly throughout the observation period. The unmodeled dynamics, such as solar pressure modeling error, are not randomly behaved so process noise will not be included. Furthermore, given the limited geometry variation in sequential geosynchronous observations, random and systematic observation error, and the data gaps inherent in multi-day tracking, it is desirable to attempt to extract as much information as possible from the entire observation pass rather than from individual observations. As such, batch estimation is chosen to process multiple passes of geosynchronous optical data rather than a sequential estimation algorithm. The following section develops and validates an angles-only batch estimator using the GEO elements.

3.6 GEO Batch Estimator

The specialized GEO element dynamic model is developed and then validated via an estimation analysis, in which a 60 second fixed-step numerical integration of the exact nonlinear dynamics (Eq. (2.40) through (2.44)) is used to model the satellite motion. A batch processor is developed to estimate the GEO state vector (Eq. (2.39)) by processing multiple nights of experimental optical data of TDRS 8. The performance of the GEO batch estimator is analyzed by comparison to a

multi-day reference orbit produced by NASA's Flight Dynamics Facility (FDF) as well as comparison to the FDF osculating element sets. An inertial Cartesian batch estimator with identical dynamic and measurement model parameters is also used to process the optical observations of TDRS 8.

3.6.1 Batch Estimator Development

The batch estimator is developed for the GEO elements by deriving the state transition matrix, Φ, the measurement model, $G(\vec{X}, t)$, and the measurement sensitivity matrix, $\tilde{H}$. The state transition matrix is a linearized temporal mapping of the state vector and state uncertainty from time $k-1$ to time k, and is computed by numerically integration. The time derivative of the state transition matrix is given by:

$$\dot{\Phi}(t_k, t_{k-1}) = [A]\,\Phi(t_k, t_{k-1}) = \left[\frac{\partial \dot{\vec{X}}(t_k)}{\partial \vec{X}(t_k)}\right] \Phi(t_k, t_{k-1}) \tag{3.29}$$

in which the $[A]$ matrix is the partial derivatives of the state time derivatives with respect to the states.

For this study, the state transition matrix is used only to propagate the state covariance matrix, P. Unlike inertial Cartesian perturbed motion, the time variation of perturbed GEO elements is always small in comparison to the elements themselves. Thus a two-body propagation model can be used in the state transition matrix, and the resulting A matrix has non-zero elements only in the first row, as follows:

$$[A] = \begin{bmatrix} A_{11} & A_{12} & A_{13} & A_{14} & 0 & 0 \\ 0 & 0 & 0 & 0 & 0 & 0 \\ 0 & 0 & 0 & 0 & 0 & 0 \\ 0 & 0 & 0 & 0 & 0 & 0 \\ 0 & 0 & 0 & 0 & 0 & 0 \\ 0 & 0 & 0 & 0 & 0 & 0 \end{bmatrix} \tag{3.30}$$

$$A_{11} = \frac{2h}{rp}\left[e_y \cos(s) - e_x \sin(s)\right] \tag{3.31}$$

$$A_{12} = \frac{-3h}{2r^2(\delta\bar{a}+1)} \tag{3.32}$$

$$A_{13} = \frac{h}{r^2 p}\left[3Ae_y(\delta\bar{a}+1) + 2r\sin(s)\right] \tag{3.33}$$

$$A_{14} = \frac{h}{r^2 p}\left[3Ae_x(\delta\bar{a}+1) + 2r\cos(s)\right] \tag{3.34}$$

For the batch estimator dynamic model the state vector is propagated via numerical integration of the exact nonlinear variational equations (Eq. (2.40) through (2.45)). The two-body state transition matrix is used for propagation of the covariance matrix from time $k-1$ to time k as follows:

$$P_k = \Phi(t_k, t_{k-1}) P_{k-1} \Phi(t_k, t_{k-1})^T \tag{3.35}$$

This approach is numerically validated by comparing a one-day covariance propagation via the simplified state transition matrix with a nonlinear sigma point propagation[36]. The two covariance matrices are compared via the size and orientation of each matrix.

The eigenvalue decomposition of both propagated covariance matrices are shown in Table 3.1, in which e_k $(k = 1...6)$ denotes the principal components. The similarity of the matrix eigenvalues shows that the uncertainty scale is similar. The principal directions of the covariance matrices are compared by vector dot product multiplication of corresponding eigenvectors; a value of ± 1 indicates that the principal axes are co-aligned. Table 3.1 displays the results of the eigenvector multiplication, showing that the two covariance matrices are nearly aligned in orientation, with the strongest orientation alignment corresponding to the maximum eigenvalue. While the eigenvectors corresponding to eigenvalues e_4 and e_5 appear to not be as closely aligned as the remaining eigenvectors, the magnitude of the eigenvalues are very similar. This indicates that the cross-section of the covariance in the plane of the fourth and fifth eigenvectors is circular, and it follows that the principal directions are arbitrary. The results of the eigenvalue decomposition show that propagating the covariance matrix via a simple two-body dynamic model captures the realistic uncertainty scale and orientation of a nonlinear, fully perturbed dynamic model.

To continue the batch estimator development, azimuth (β) and elevation (ε) angular measurements of satellite position are modeled. The measurement model, $G(\vec{X}, t)$, is generated by

Table 3.1: Eigenvalue Decomposition of the Propagated Covariance Matrices

Principal Component	Two-Body Eigenvalue	Sigma Point Eigenvalue	Eigenvector Dot Product
e_1	5.5 x 10^{-8}	5.3 x 10^{-8}	0.98
e_2	6.5 x 10^{-8}	5.6 x 10^{-8}	0.98
e_3	1.3 x 10^{-7}	1.3 x 10^{-7}	-0.99
e_4	7.0 x 10^{-5}	7.0 x 10^{-5}	-0.72
e_5	7.6 x 10^{-5}	8.0 x 10^{-5}	0.72
e_6	1.3 x 10^{-3}	1.2 x 10^{-3}	0.99

expressing the Earth-Centered Earth-Fixed (ECEF) position of the satellite as a function of the GEO elements as given by:

$$\vec{R}_{ECEF} = \begin{bmatrix} R_x \\ R_y \\ R_z \end{bmatrix} = \left[T_{ECEF}^{ECI}\right] \vec{R}_{ECI}$$

$$= \left[T_{ECEF}^{ECI}\right] \frac{r}{1+Q_1^2+Q_2^2} \begin{bmatrix} (1+Q_2^2-Q_1^2)\cos(s) + 2Q_1Q_2\sin(s) \\ (1+Q_1^2-Q_2^2)\sin(s) + 2Q_1Q_2\cos(s) \\ 2(Q_2\sin(s) - Q_1\cos(s)) \end{bmatrix} \quad (3.36)$$

The ECEF position vector is then rotated into a topocentric frame and the measurement angles geometrically computed. T_{ECI}^{ECEF} denotes the transformation matrix from the Earth-Centered Inertial (ECI) frame to the ECEF frame, including precession, nutation, and non-constant Earth rotation rate. T_{ECEF}^{ENU} represents the geometric rotation from the ECEF frame to the East-North-Up topocentric frame.

$$\vec{\rho}_{ENU} = \begin{bmatrix} \rho_E \\ \rho_N \\ \rho_U \end{bmatrix} = \left[T_{ENU}^{ECEF}\right] (\vec{R}_{ECEF} - \vec{R}_{site,ECEF}) \quad (3.37)$$

$$G(\vec{X}, t) = \begin{bmatrix} \beta \\ \varepsilon \end{bmatrix} = \begin{bmatrix} \tan^{-1}(\frac{\rho_E}{\rho_N}) & \sin^{-1}(\frac{\rho_U}{|\vec{\rho}_{ENU}|}) \end{bmatrix}^T \quad (3.38)$$

The measurement model includes normally distributed random noise with a mean of zero arcseconds and standard deviation of two arcseconds. Measurement corrections to account for the light transit time from the satellite to the ground-based sensor are also incorporated in the model. The measurement model does not account for aberration of the optical signal.

Finally, the measurement sensitivity matrix, $\tilde{H}$, is determined by evaluating the partial derivatives of the measurement model with respect to the GEO elements. For simplicity the measurement sensitivity matrix is separated into its partial derivative components as follows:

$$\tilde{H} = \frac{\partial G(\vec{X}, t)}{\partial \vec{\rho}_{ENU}} \frac{\partial \vec{\rho}_{ENU}}{\partial \vec{R}_{ECEF}} \frac{\partial \vec{R}_{ECEF}}{\partial \vec{X}} \tag{3.39}$$

The partial derivative components are given by:

$$\frac{\partial G(\vec{X}, t)}{\partial \vec{\rho}_{ENU}} = \begin{bmatrix} \left[\rho_N(\frac{\rho_E^2}{\rho_N^2} + 1)\right]^{-1} & -\rho_E \left[\rho_N(\frac{\rho_E^2}{\rho_N^2} + 1)\right]^{-1} & 0 \\ \frac{-\rho_E \rho_N}{\rho^2 \sqrt{\rho^2 - \rho_U^2}} & \frac{-\rho_U \rho_N}{\rho^2 \sqrt{\rho^2 - \rho_U^2}} & \frac{\sqrt{\rho^2 - \rho_U^2}}{\rho^2} \end{bmatrix} \tag{3.40}$$

$$\frac{\partial \vec{\rho}_{ENU}}{\partial \vec{R}_{ECEF}} = \left[T_{ENU}^{ECEF}\right] \frac{\partial (\vec{R}_{ECEF} - \vec{R}_{site,ECEF})}{\partial \vec{R}_{ECEF}} = \left[T_{ENU}^{ECEF}\right] \tag{3.41}$$

$$\frac{\partial \vec{R}_{ECEF}}{\partial \vec{X}} = \left[T_{ECEF}^{ECI}\right] \frac{\partial \vec{R}_{ECI}}{\partial \vec{X}} \tag{3.42}$$

The performance of the GEO batch estimator is compared against the more conventional inertial Cartesian batch estimator. To ensure an appropriate comparison, the dynamic model is identical between both estimators. As was demonstrated in Section 2.7.1 and Fig. 2.4, at a 60 second fixed time-step the numerical propagation in GEO and inertial Cartesian state spaces are comparable.

It is anticipated that the inertial Cartesian batch estimator will not perform as well as the GEO element batch estimator due to the linearization of the measurement sensitivity matrix, H. For a geosynchronous object the longitudinal state, λ, is highly correlated with the azimuthal angle measurement, whereas the ECI positions X and Y are position vector components primarily in the azimuth plane. Due to this non-direct relationship between X and Y and the azimuth measurement,

the linearized inertial Cartesian measurement sensitivity matrix is more affected by a loss of second-order terms than the GEO element measurement sensitivity matrix. This inaccuracy of the inertial Cartesian measurement sensitivity matrix manifests as a poor longitudinal estimate and larger estimated uncertainty when compared to that of the GEO batch estimator.

3.6.2 Experimental Performance of Batch Estimator

The GEO element batch estimator is validated by processing multiple nights of ground-based optical observations of TDRS 8. The estimator uses a reduced dynamic model including a 4x4 Earth gravity field, luni-solar gravity perturbations, and solar radiation pressure. TDRS 8 is chosen as a reference satellite because the FDF computes and publishes daily high-accuracy osculating elements (30-40 meters accuracy) as well as multi-day long term ephemerides (kilometer-level accuracy) for this satellite.[57; 59] The spacecraft parameters provided in the osculating element sets are used to model the solar pressure perturbation. From July 2, 2005 to July 8, 2005, six nights of TDRS 8 optical data were provided by the Air Force Maui Optical and Supercomputing Site (AMOS). During the observation time period, FDF has verified maneuvers on the first and fifth days. To avoid data reduction over maneuvers, only the second through fourth and six through eighth nights of data are used in this analysis. Throughout the data period, two consecutive nights of optical data are processed by the GEO and inertial Cartesian estimators. The following data sets are processed: July 2 and July 3 (Case 1), July 3 and July 4 (Case 2), July 6 and July 7 (Case 3), and July 7 and July 8 (Case 4). A pictorial summary of the analysis timeline is shown in Fig. 3.3.

First, the impact of using the simplified two-body state transition matrix for uncertainty propagation is revisited and further analyzed by using two batch estimators to process the July 2, 2005 and July 3, 2005 data and comparing the GEO state solutions. The first batch estimator uses the two-body state transition matrix while the second batch estimator uses a fully perturbed state transition matrix. All initial conditions and dynamic model parameters are identical for both estimations. The difference between the two solutions is on the order of millimeters in inertial position and micrometers per second in inertial velocity, indicating that use of the simplified state

transition matrix does not significantly affect the estimator solution accuracy over the two day propagation period.

Several metrics are generated to test the GEO and inertial Cartesian estimates. The error between the postfit solution and the multi-day reference ephemeris is computed for both state space solutions for each of the four batch fits. As the FDF osculating elements are more accurate than the multi-day reference ephemeris, the batch solution is propagated forward and backward to the available osculating element sets directly before and after the solution epoch. The error between the propagated solution and reference osculating elements is transformed into the radial, in-track, cross-track (RIC) reference frame. Finally, postfit residuals are compared with predicted residuals for the reference orbit. These metrics serve to evaluate the utility of GEO element orbit estimation and compare the GEO element batch performance with inertial Cartesian estimation.

The *a priori* satellite state for both the GEO and inertial Cartesian batch estimators is initialized with the FDF multi-day ephemeris interpolated at the observation epoch of each case. The *a priori* ephemeris for Case 1 is shown in Table 3.2 in GEO elements and inertial Cartesian coordinates. The initial conditions of Cases 2 through 4 are shown in inertial Cartesian coordinates in Table. 3.3. The GEO and inertial Cartesian batch solutions for Cases 1 through 4, also shown in inertial Cartesian coordinates, are presented in Table 3.4.

Table 3.2: Initial Conditions for Case 1

GEO Elements	λ (rad)	$\delta\bar{a}$	e_y	e_x	Q_1	Q_2
	3.239042	2.0 x 10^{-6}	-6.17 x 10^{-5}	2.03 x 10^{-4}	-2.2723 x 10^{-2}	-2.496 x 10^{-3}
ECI	X (km)	Y (km)	Z (km)	V_x (km/s)	V_y (km/s)	V_z (km/s)
	-38607.028	-16870.673	-1671.236	1.227676	-2.817972	0.069896

Table 3.3: Initial Conditions for Cases 2 Through 4

	X (km)	Y (km)	Z (km)	V_x (km/s)	V_y (km/s)	V_z (km/s)
Case 2	-39502.150	-14638.188	-1720.661	1.065057	-2.883369	0.062724
Case 3	-36211.215	-21560.852	-1527.459	1.568735	-2.642071	0.084087
Case 4	-31578.943	-12923.965	-1282.913	2.032161	-2.303849	0.103245

Table 3.4: Solution for Cases 1 Through 4

		X (km)	Y (km)	Z (km)	V_x (km/s)	V_y (km/s)	V_z (km/s)
Case 1	GEO	-38579.232	-16934.479	-1669.699	1.232320	-2.815933	0.070114
	Cartesian	-38579.383	-16934.135	-1669.608	1.232295	-2.815944	0.070113
Case 2	GEO	-39504.664	-14638.772	-1720.748	1.065095	-2.883537	0.062746
	Cartesian	-39504.775	-14638.390	-1720.752	1.065068	-2.883550	0.062744
Case 3	GEO	-36213.514	-21561.988	-1527.471	1.568815	-2.642234	0.084108
	Cartesian	-36213.654	-21561.587	-1527.471	1.568789	-2.642257	0.084108
Case 4	GEO	-31580.609	-27925.193	-1282.885	2.032249	-2.303969	0.103265
	Cartesian	-31580.843	-27924.889	-1282.893	2.032228	-2.303990	0.103265

The Case 2 GEO and Cartesian postfit solutions are each differenced from the FDF multi-day reference orbit. Fig. 3.4 shows the inertial position and velocity error magnitudes for this fit, which are representative of the error magnitudes for Cases 1, 3 and 4. The GEO solution position and velocity errors are on the order of 600 meters and 3 centimeters per second, respectively. The inertial Cartesian errors are on the order of 1 kilometer in position and 7 centimeters per second in velocity. As both estimators employ identical dynamic parameters and initial conditions and the dynamic propagations are of comparable accuracy, the error differences shown in Fig. 3.4 demonstrate that the two state space estimators converge on significantly different solutions. As the multi-day reference orbit is only accurate to the kilometer level and both position error magnitudes are less than 1 kilometer, conclusions cannot be drawn about the accuracy of each batch fit.

The Case 1 solutions are propagated back to the previous osculating element epoch (July 3, 2005 0:0:0 UTC) and forward to the next available osculating element epoch (July 4, 2005 0:0:0 UTC). Table 3.5 displays the difference between the propagated solutions and the FDF osculating element sets in the RIC position and velocity. Tables 3.6 through 3.8 present the RIC frame errors from the osculating element sets for Cases 2, 3 and 4. The solution for Case 4 is only compared to the previous osculating element set as a high accuracy osculating element set for July 8 is not available. Each case shows that the GEO element batch performs considerably better than the inertial Cartesian batch in estimating in-track position and radial velocity.

Table 3.5: Comparison of Case 1 Solutions to FDF Osculating Elements

Epoch		R (m)	I (m)	C (m)	V_r (cm/s)	V_i (cm/s)	V_c (cm/s)
0:0:0 UTC July 2, 2005	GEO	10.110	-203.985	-227.187	1.0	0.7	-0.3
	Cartesian	10.666	-579.404	-227.214	3.7	0.7	-0.4
0:0:0 UTC July 3, 2005	GEO	6.603	-131.226	-228.759	1.3	-0.1	-0.1
	Cartesian	7.157	-506.651	-228.786	4.0	-0.1	-0.1

Table 3.6: Comparison of Case 2 Solutions to FDF Osculating Elements

Epoch		R (m)	I (m)	C (m)	V_r (cm/s)	V_i (cm/s)	V_c (cm/s)
0:0:0 UTC July 3, 2005	GEO	59.403	0.075	-215.707	-0.4	0.1	-0.6
	Cartesian	45.840	-484.717	-216.407	2.8	0.3	-0.5
0:0:0 UTC July 4, 2005	GEO	22.378	31.678	-246.666	0.4	-0.1	0
	Cartesian	8.321	-441.992	-247.307	3.7	-0.1	0

Table 3.7: Comparison of Case 3 Solutions to FDF Osculating Elements

Epoch		R (m)	I (m)	C (m)	V_r (cm/s)	V_i (cm/s)	V_c (cm/s)
0:0:0 UTC July 6, 2005	GEO	84.296	-114.922	-182.363	0.0	-0.8	0.1
	Cartesian	57.628	-805.466	-184.911	4.3	-0.7	0.1
0:0:0 UTC July 7, 2005	GEO	-21.582	-149.947	-220.089	1.0	0.1	0.4
	Cartesian	-49.825	-855.204	-222.514	5.8	0.3	0.4

Table 3.8: Comparison of Case 4 Solutions to FDF Osculating Elements

Epoch		R (m)	I (m)	C (m)	V_r (cm/s)	V_i (cm/s)	V_c (cm/s)
0:0:0 UTC July 7, 2005	GEO	133.173	-71.469	-179.006	-0.3	-1.5	0.0
	Cartesian	122.717	-559.841	-180.112	3.0	-1.4	0.01

The postfit residuals for Case 2 are compared to residuals generated using the multi-day reference ephemerides in order to assess how well each orbit fits the experimental data. The reference orbit is interpolated to the observations times. Fig. 3.5 displays the residuals for the three days of measurements and is representative of each case's results. The residual RMS values are approximately 0.7 arcseconds in right ascension and 0.4 arcseconds in declination for all four cases. The systematic error seen in the GEO estimator residuals is due to unmodeled solar pressure. The FDF reference residuals do not display such systematic behavior; however, there is evidence of measurement bias. The azimuth reference residuals possess a time-varying offset, and there is a constant offset of approximately 1 arcsecond in elevation. Note that 1 arcsecond is approximately 200 meters at the geosynchronous altitude. These offsets indicate sensor bias which can alias error into the batch solution.

Because of the systematic measurement error as well as unmodeled dynamics in the experimental data, the GEO element and inertial Cartesian batch estimators are also compared by processing simulated data. Simulated data are created to mimic the data sets of Cases 1 and 2. A variable step numerical propagator is initialized with the FDF osculating element sets for July 2 and July 3. The dynamic model includes the 4x4 gravity field, luni-solar gravity, and solar radiation pressure. A simulated reference orbit is used to compute azimuth and elevation measurements at the same times as the experimental observations. The simulated observations are degraded with 2 arcseconds of Gaussian noise.

The GEO and inertial Cartesian estimators, which now include perfect measurement and dynamic models, are initialized with the FDF multi-day reference orbit interpolated to the observation epoch. The postfit solutions of each batch estimator are then differenced from the simulated reference orbit. Figs. 3.6 and 3.7 present the RIC frame position and velocity errors relative to the reference orbit for the fit to simulated July 3 and July 4 data (experimental data Case 2). The simulation of Case 1 produces similar results. The results show that the radial and cross-track position and in-track and cross-track velocity errors are the same order of magnitude for both estimators, indicating that the GEO and batch are able to similarly recover these components. However, the in-track position and radial velocity errors are orders orders of magnitude larger for the inertial Cartesian estimator. The significant discrepancy in estimated solutions cannot be attributed to dynamic or measurement mismodeling or accuracies of the reference orbit; the inertial Cartesian estimator cannot recover the azimuthal motion as well as the GEO element estimator due to the linearization of the measurement sensitivity matrix.

In order to assess the impact of the measurement sensitivity matrix linearization on the estimation solution, the estimated state uncertainties for the inertial Cartesian and GEO element estimators are compared. The estimated state uncertainties for the simulation of experimental data Cases 1 and 2, obtained from the batch estimated covariance matrix, are shown in GEO element space in Table 3.9 and in ECI space in Table 3.10. The results show that the λ estimated uncertainty is one order of magnitude larger for the inertial Cartesian estimator than the GEO estimator; all other GEO element uncertainties are very similar. At the nominal geosynchronous altitude, the difference between the GEO and ECI estimated longitudinal uncertainties is approximately 1kilometer. However, this significant longitudinal uncertainty difference is not visible in the ECI-space uncertainty, for which all state uncertainties are similar for both estimators.

Table 3.9: Estimated GEO State Uncertainties of Simulation Analysis

Case 1		λ (rad)	$\delta\bar{a}$	e_y	e_x	Q_1	Q_2
	GEO	1.12 x 10^{-6}	8 x 10^{-8}	3.6 x 10^{-7}	1.07 x 10^{-6}	3.7 x 10^{-7}	2.9 x 10^{-7}
	Cartesian	2.436 x 10^{-5}	8 x 10^{-8}	5.9 x 10^{-7}	9.6 x 10^{-7}	3.8 x 10^{-7}	2.9 x 10^{-7}
Case 2		λ (rad)	$\delta\bar{a}$	e_y	e_x	Q_1	Q_2
	GEO	1.15 x 10^{-6}	1.7 x 10^{-7}	5.6 x 10^{-7}	1.25 x 10^{-6}	4.2 x 10^{-7}	3.5 x 10^{-7}
	Cartesian	2.900 x 10^{-5}	1.7 x 10^{-7}	1.13 x 10^{-6}	7.8 x 10^{-7}	34.2 x 10^{-7}	2.9 x 10^{-7}

Table 3.10: Estimated ECI State Uncertainties of Simulation Analysis

Case 1		X (m)	Y (m)	Z (m)	V_x (cm/s)	V_y (cm/s)	V_z (cm/s)
	GEO	26.763	53.434	27.131	0.3	0.4	0.2
	Cartesian	26.808	56.485	27.129	0.3	0.4	0.2
Case 2		X (m)	Y (m)	Z (m)	V_x (cm/s)	V_y (cm/s)	V_z (cm/s)
	GEO	33.750	60.691	31.334	0.3	0.5	0.3
	Cartesian	33.766	60.721	31.336	0.3	0.5	0.3

Finally, the scales of the covariance matrices produced via the two batch estimators are analyzed and compared through eigendecomposition. For comparison, the inertial Cartesian covariance matrices are transformed into the GEO element space by nonlinear sigma-point propagation. Table 3.11 displays the eigenvalues (e_1 through e_6, in descending order) of the batch estimated covariance matrices for each of the four cases. The maximum eigenvalue of the covariance matrix estimated by the inertial Cartesian batch processor is consistently on the order of 1×10^{-11}, while the maximum eigenvalue produced by the GEO element estimator is on the order of 1×10^{-12}. Furthermore, the minimum eigenvalues are on the order of 1×10^{-13} and 1×10^{-15} for the inertial Cartesian and GEO element estimators, respectively. The eigenvalue comparison shows that the scale of the GEO element covariance matrix is smaller than the inertial Cartesian covariance matrix. This result demonstrates that geosynchronous estimation in the GEO element state space better recovers the GEO element state compared to estimation in the Cartesian state space.

Table 3.11: Eigenvalues of Estimated Covariance Matrices

Case 1		e_1	e_2	e_3	e_4	e_5	e_6
	GEO	2.6×10^{-12}	5.6×10^{-13}	1.8×10^{-13}	1.2×10^{-13}	5.1×10^{-14}	7.3×10^{-15}
	Cartesian	2.7×10^{-11}	4.4×10^{-12}	5.8×10^{-13}	2.8×10^{-13}	1.7×10^{-13}	1.4×10^{-13}
Case 2		e_1	e_2	e_3	e_4	e_5	e_6
	GEO	2.0×10^{-12}	5.0×10^{-13}	1.8×10^{-13}	5.6×10^{-14}	4.7×10^{-14}	1.3×10^{-15}
	Cartesian	1.8×10^{-11}	3.5×10^{-12}	4.7×10^{-13}	1.8×10^{-13}	1.3×10^{-13}	1.1×10^{-13}
Case 3		e_1	e_2	e_3	e_4	e_5	e_6
	GEO	5.8×10^{-12}	1.1×10^{-12}	5.7×10^{-13}	1.6×10^{-13}	9.9×10^{-14}	9.1×10^{-15}
	Cartesian	5.5×10^{-11}	6.4×10^{-12}	1.1×10^{-12}	7.4×10^{-13}	3.4×10^{-13}	2.3×10^{-13}
Case 4		e_1	e_2	e_3	e_4	e_5	e_6
	GEO	3.6×10^{-12}	1.2×10^{-12}	4.6×10^{-13}	1.6×10^{-13}	1.6×10^{-13}	2.3×10^{-15}
	Cartesian	3.6×10^{-11}	4.0×10^{-12}	1.1×10^{-12}	3.4×10^{-13}	2.6×10^{-13}	1.8×10^{-13}

3.6.3 Conclusions

Comparison of a GEO batch estimator with an inertial Cartesian batch estimator showed that the GEO estimator is able to capture the in-track position and radial velocity of the orbit significantly better than the inertial Cartesian estimator (hundreds of meters in position and a few centimeters per second in velocity). Simulation studies, conducted to eliminate the presence of mismodeled dynamics and measurements, confirmed that the in-track position and radial velocity estimation discrepancy between the two element sets is a direct result of the estimation process. The batch performance discrepancy is due to the linearization of the azimuth and elevation measurement sensitivity matrix. The results of this work demonstrate that the GEO element set is an appropriate choice for the dynamic modeling of geosynchronous satellites.

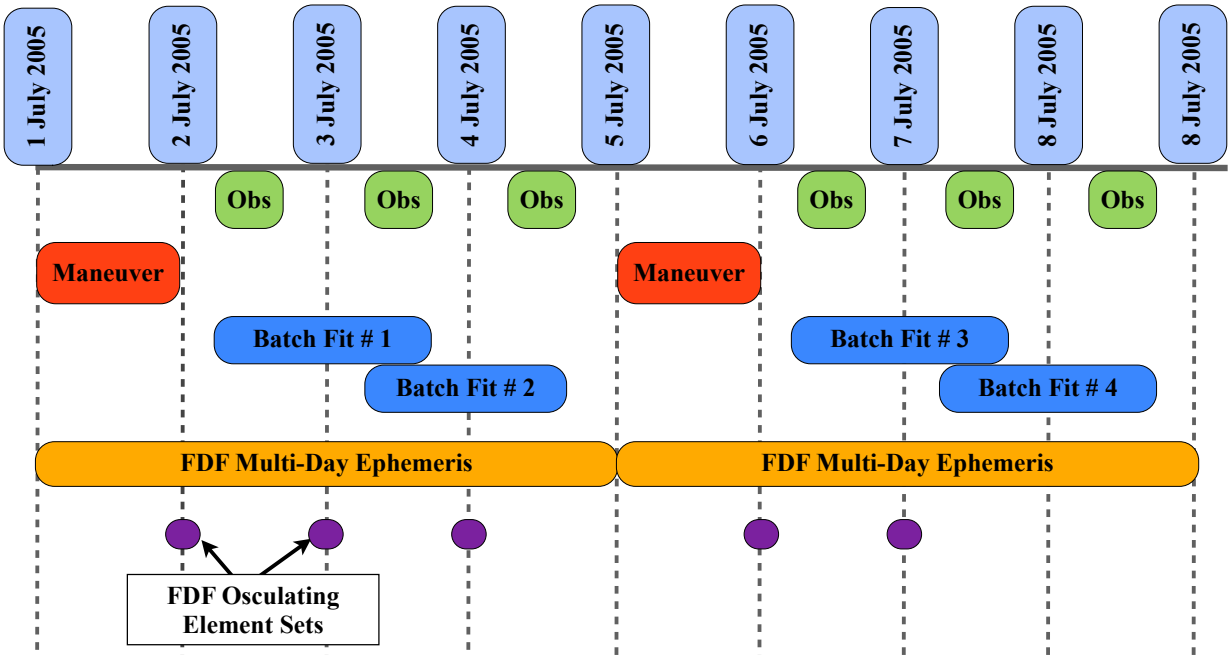

Figure 3.3: Graphical Representation of Batch Analysis Timeline

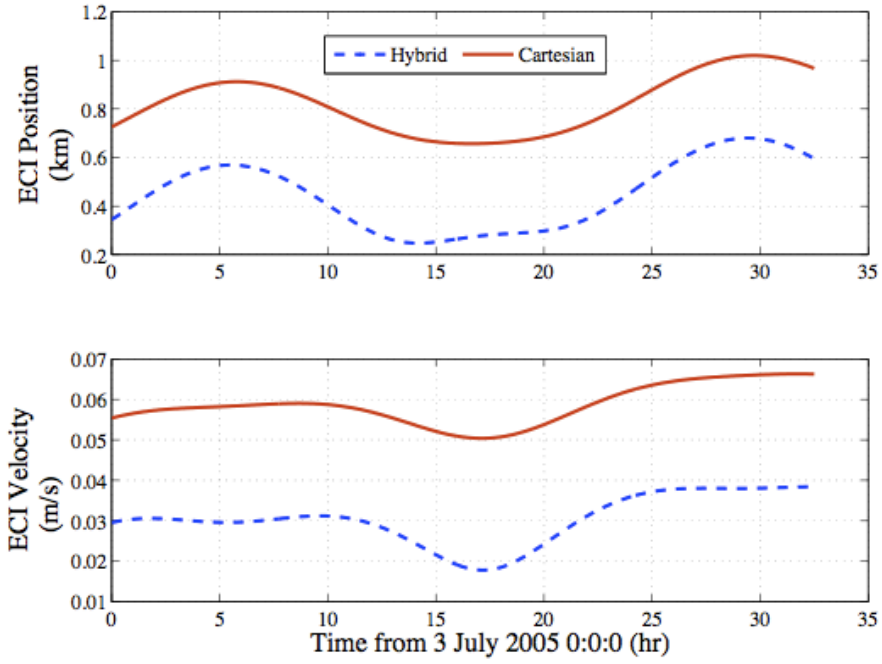

Figure 3.4: Postfit Solution Error Relative to Multi-Day Reference Orbit

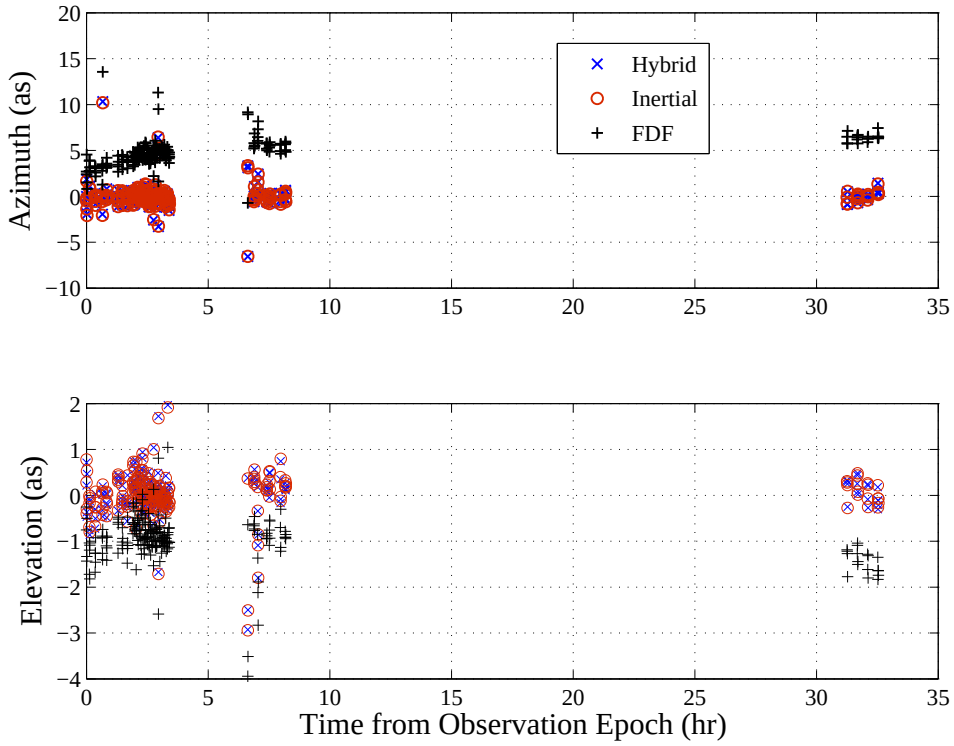

Figure 3.5: Measurement Residuals of Multi-Day Reference Orbit and Batch Solutions

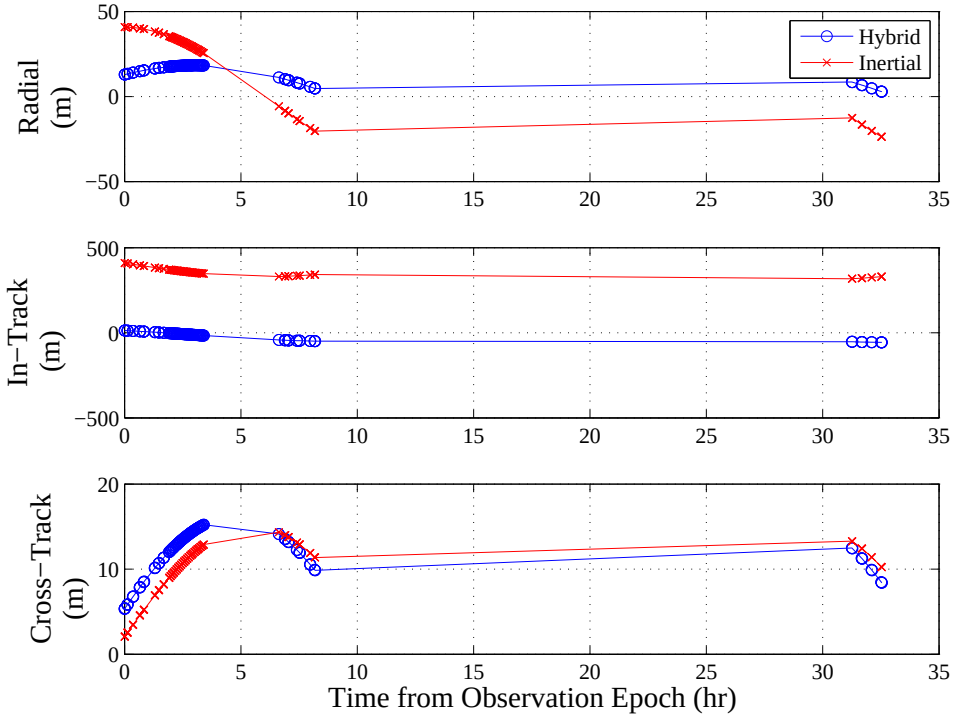

Figure 3.6: Postfit RIC Position Error from Simulated Reference Orbit

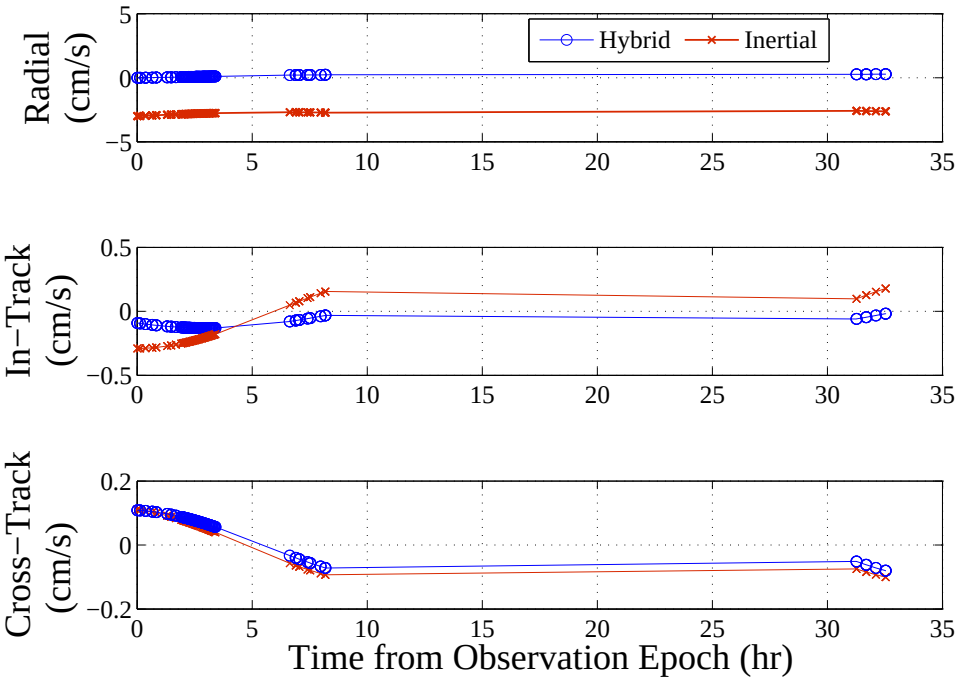

Figure 3.7: Postfit RIC Velocity Error from Simulated Reference Orbit

Chapter 4

Ground-Based Angles-Only Tracking

4.1 Introduction

The estimation of geosynchronous orbits using ground-based angles-only measurements is a challenge due to the very slight geometrical variation of the observations, uncertainties in the dynamic model, and the temporal and weather limitations to ground-based optical tracking. Fortunately, in many cases an orbit solution is required after only a day or two of optical tracking and is not required in real time. It is therefore of interest to characterize the short-term tracking requirements necessary to obtain a specified geosynchronous orbit accuracy using optical tracking from a single ground station; conversely, it is desirable to understand the orbit accuracy possible given limited tracking coverage and observation sampling rates. This knowledge is essential for track planning and resource allocation. This work investigates the impact of nightly track length, sampling interval, orbit epoch location, and realistically mismodeled spacecraft dynamics on estimation accuracy.

Angles-only geosynchronous orbit estimation with data arcs on the order of 1 week have been well characterized by Sabol and Culp [76; 77]. Simulation studies showed that due to the difficulty in estimating the radial position using optical data, 10 meter accuracy estimates are possible with 1 week of tracking. In particular, the semi-major axis cannot be accurately estimated given only one night of tracking as the offset from the nominal geosynchronous semi-major axis is manifested only in the slowly drifting azimuth measurement. Ranging data allow for a more accurate and quicker estimate of the orbit states, including the semi-major axis. The addition of range measurements

to the angular data resulted in 5 meter orbit accuracy.[77] Follow-on research by Sabol, et. al. [78] and Visser, et. al. [107] used optical observations of TDRS 5 collected with a high-accuracy optical sensor. Comparisons to TDRS reference osculating element sets are made. The position errors were shown to be approximately 5 meters in the radial direction and 10 meters in both cross-track and along-track components.

Recent research by Vallado and his colleagues on geosynchronous debris has focused on the orbit estimation accuracy achievable using angles-only optical observations and the fusion of international data sources for collision avoidance.[105; 106] Their work used optical observations collected by the International Scientific Observing Network (ISON), a cooperative network of global sensors capable of providing ground-based coverage of the entire geosynchronous belt.[6] Experimental optical observations of several individual objects were processed with an initial orbit determination, the results of which were fed into a least-squares batch processor followed by a filter-smoother. It was shown that 10 to 15 observations per day over the course of 3 to 4 days produced orbit accuracy on the order of a few kilometers.

Research on sparse angles-only geosynchronous orbit estimation has also been conducted by Sawada Kawase of the Kashima Space Communications Center, Communications Research Laboratory, Japan.[47] Kawase theoretically computed optical orbit determination error for geosynchronous satellites using one to two consecutive nights of line-of-sight measurements collected only once or twice per evening. Using first order linearized equations of unperturbed satellite motion, theoretical expressions were developed which express orbit element estimation uncertainty as a function of the angular separation between observations. Given one day of data collected over a six hour period and measurement noise on the order of 1 arcsecond, Kawase found the expected orbit uncertainty to be on the order of 1 kilometer.

Finally, recent angles-only orbit determination research involving geosynchronous space debris has been performed by Musci and Schildknecht, et. al.[63; 64; 84; 85] The high area-to-mass geosynchronous debris evolution studied by Valk, et. al. ([99; 100]) has been validated with angles-only optical measurements collected over long periods (on the order of years).[63] By fitting to

long arcs of optical data, it was shown that a population of high-eccentricity debris objects with mean motion of approximately one revolution per day exists in the geosynchronous region.[85] It was observed that the eccentricity oscillation amplitude is proportional to the object's area-to-mass ratio.

This work empirically determines the relationship between tracking parameters and estimation accuracy when using variational equations to model realistically perturbed geosynchronous dynamics. High-precision reference ephemerides of the Wide Area Augmentation System (WAAS) satellites provide a unique opportunity to investigate orbit estimation techniques with publicly-available experimental data that are accurate to the meter level. This is a significant accuracy improvement over the commonly-used TDRS reference osculating elements, which are provided for a single epoch and are accurate to approximately 30 to 40 meters.[57] The nonlinear variational equations used in this study have been developed for a set of GEO elements. The achievable accuracy of angles-only orbit estimation is determined by fitting to two consecutive days of optical measurements while varying the tracking parameters of nightly track length, observation sampling interval, and orbit epoch location. Two consecutive days of data are processed in order to accurately recover the semi-major axis. To assess the short-term orbit determination accuracy it is necessary to compare the estimated orbit solution and uncertainty against a reference orbit. While simulation studies can provide a perfectly-known reference orbit and observations of the object, simulated observations do not capture the complexities of actual measurements and geosynchronous orbital dynamics. Conversely, experimental measurements reflect realistic dynamics but can be degraded with unknown time-varying and constant biases, which in turn introduce unexpected error into the orbit solution. To overcome the respective drawbacks of simulated and experimental observations, this work builds a simulation study around the daily point solutions of WAAS satellites.

4.2 Wide Area Augmentation System Satellites

WAAS is an augmentation to GPS provided by the Federal Aviation Administration (FAA) to improve the integrity and accuracy of GPS for aviation use. WAAS nominally comprises a net-

work of ground-based Wide-Area Master Stations and Reference Stations spanning North America, and two geosynchronous satellites which transmit pseudorandom ranging signals and position, clock and atmospheric corrections to North American user receivers.[60] Fig. 4.1 presents an artistic representation of the WAAS space and ground resources.[2] The Reference Stations track the WAAS satellites pseudorange signals, and from this tracking data the WAAS reference position and velocity point solutions are estimated.[25] The reference ephemerides are produced using a high-precision GPS solution code, which was based on the Real Time Gipsy code from the Jet Propulsion Laboratory.[16] The typical accuracy of these solutions is reported to be as good as meter-level per axis, and the accuracy level of a specific reference ephemerides is indicated by the User Range Accuracy index.[26] WAAS users who incorporate the additional ranging measurement from the geostationary satellite, rely on these orbit predictions in their position solutions. Many users only depend on the WAAS for corrections and integrity for the GPS satellites, and are completely unaffected by the accuracy of the WAAS orbits.

Figure 4.1: Ground and Space Resources Comprising the WAAS Network[2]

The Earth-Centered Earth-Fixed (ECEF) position and velocity point-solutions of each WAAS satellite are provided 24 hours per day at 256 second intervals.[26] An archive of the reference point-

solutions is publicly accessible through the FAA.[2] Though sensitive to measurement noise, the reference ephemerides are reported to be accurate to better than 10 meters, even over spacecraft maneuvers.[25]

As of November 2010, three WAAS satellites are on orbit: Anik F1R, Inmarsat 4F3, and Galaxy 15. Galaxy 15 failed on orbit on April 5, 2010, and has subsequently been operationally replaced for WAAS transmissions by Inmarsat 4F3.[66] It is believed that the spacecraft failure was caused by intense solar activity.[66] The failure is unusual in that it resulted in the satellite being unresponsive to ground commands, but still capable of broadcasting valid WAAS signals. After the failure Galaxy, 15 drifted within close proximity of several active geosynchronous satellites and continued to drift through the geosynchronous belt until December 23, 2010.[65; 67; 92] At that time, the onboard battery completely drained and the satellite reset itself, allowing Galaxy 15 to begin accepting control commands once again.[92] During the time it was inactive, Galaxy 15 was a unique uncontrolled satellite in that it was not maneuvering, but it continued to actively broadcast its GPS-like pseudoranging signal. Additionally, the WAAS ground segment continued to observe these signals and to estimate the satellite's orbit. The WAAS reference ephemerides provided between April 5 and December 23 can therefore be used to assess the estimation accuracy of uncontrolled WAAS satellites.

4.3 Approach

This empirical analysis constructs simulated optical measurements based on the high-accuracy WAAS reference ephemerides. First, simulated optical observations are generated from a two-day span of the reference ephemeris. Subsets of the simulated continuous observations are then created for a given set of nightly track length, sampling interval, and observation epoch time. A GEO element batch estimator is used to process each observation subset individually, and the estimated solution is differenced from the reference ephemeris. The three-dimensional (3D) ECEF position errors over the two day fit period, quantified by the Root Mean Square (RMS), are compared for all subset solutions.

4.3.1 Track Length and Sampling Interval Variation

Simulated azimuth and elevation measurements of Anik F1R and Galaxy 15 are generated from the reference ECEF ephemerides of May 2010. The reference observations, generated at the reference sampling interval of 256 seconds, are interpolated at the selected sampling rate for the chosen nightly track length. Gaussian noise with a mean of zero arcseconds and a standard deviation of 1 arcsecond is added to the observations to replicate the measurement noise expected in experimental observations.[77].

The tracking parameters varied for this study are shown in Table 4.1. The shorter sampling intervals (10 to 30 seconds) are practical assuming dedicated tracking of a single object, while the longer sampling intervals (1800 to 10800 seconds) are applicable in a tracking scenario where more than one object must be tracked through the night and the sensor is able to revisit the objects. Track lengths of 30 minutes to 6 hours per night are reasonable for optical tracking which depends on the proper lighting conditions and clear skies. Cases in which fewer than 3 observation pairs are available are not processed as the number of estimated parameters would be greater than the number of observations.

Table 4.1: Variation Parameters for Batch Estimation Analysis

Nightly Track Length	Sampling Interval
10 minutes	10 seconds
30 minutes	30 seconds
1 hour	256 seconds
3 hour	1800 seconds
6 hour	3600 seconds

4.3.2 Observed Orbit Geometry Variation

A geosynchronous object traces out an elliptical pattern that drifts slowly in azimuth relative to an Earth-fixed vantage point. An example of this motion is depicted in Fig. 4.2, which shows the azimuth and elevation measurements of Anik F1R on May 2 and 3, 2010 as seen by an observer in Albuquerque, New Mexico. It takes approximately 24 hours for the satellite to traverse one ellipse. The motion is largely repeatable and the entire azimuth and elevation span is less than 0.2 degrees. For comparison, Fig. 4.3 displays the azimuth and elevation measurements of Galaxy 15 as seen from the same ground station. The observations are plotted for 1 May through 5 May, 2010, approximately one month after the spacecraft's failure. Unlike Anik F1R, the drift rate of Galaxy 15 is significantly faster than that of the Earth and it shifts in both azimuth and elevation. This behavior is typical of an inactive geosynchronous satellite that is not controlled to remain near its nominal mean longitude and radial distance. Reference measurements corresponding to five epochs for Anik F1R are marked in the figure. The epochs are listed in Table 4.2.

Table 4.2: Shifted Observation Epochs for Anik F1R

Epoch Number	UTC on 5.2.2010
1	00:01:04
2	03:01:04
3	06:01:04
4	09:01:04
5	12:01:04

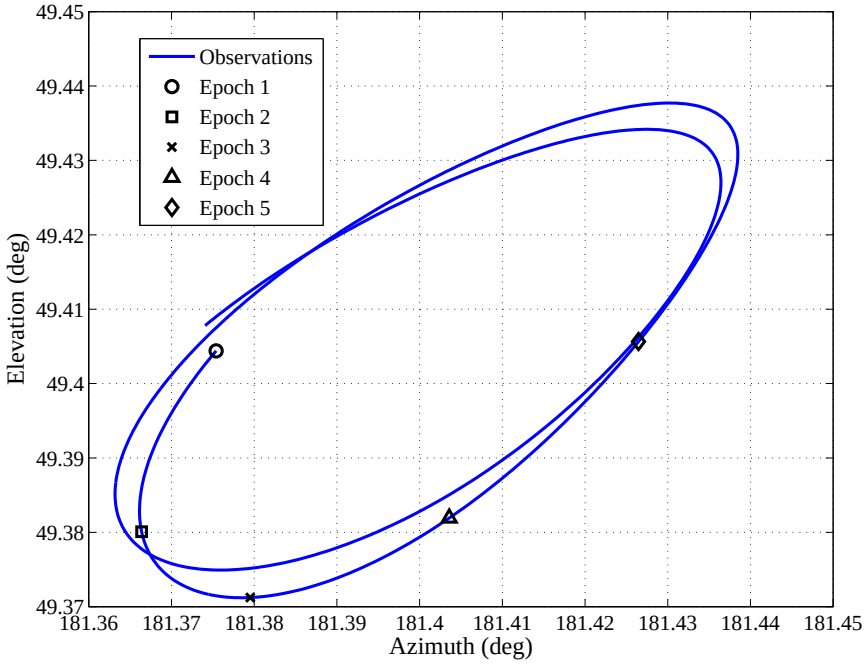

Figure 4.2: Anik F1R Reference Observations and Selected Epoch Locations (May 2 - May 3, 2010)

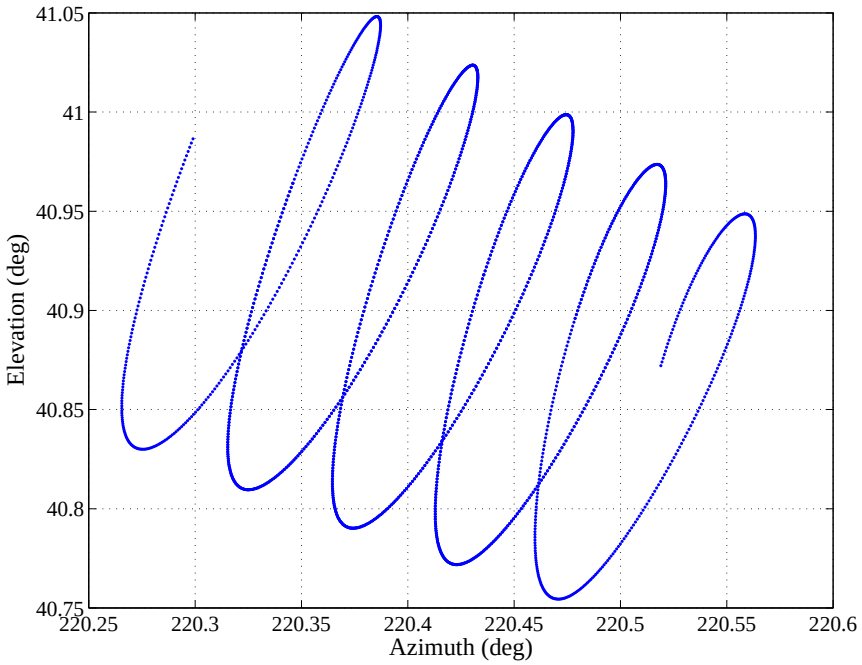

Figure 4.3: Galaxy 15 Reference Observations (May 1 - May 2, 2010)

The geosynchronous orbit location, shape and drift are dictated by the satellite's orbital elements; the semi-major axis offset from the nominal geosynchronous semi-major axis is directly proportional to the azimuthal drift, the inclination sets the tilt angle relative to the azimuth plane, and the eccentricity determines the ellipse proportions. The mean azimuth is set by the mean longitude and the ellipse pinching, or nodal crossing point, is a function of right ascension of the ascending node and semi-major axis.[90] The observation geometry may affect the accuracy of the estimated orbit as the ellipse characteristics are tied to different orbit elements. For example, the semi-major axis can only be recovered accurately by observing the time-variation of the azimuth measurements. To see this effect we will shift the observation epoch to vary the orbit section that is observed and compare the respective estimated solutions. The observations shown in Fig. 4.2 begin at Epoch 1, which corresponds to a UTC time of 00:01:04 on May 2. Results will be shown for a range of observation epochs shifted by 3 hour increments. This ensures that track lengths beginning at each of the five selected epochs provide unique geometries, including the nodal crossing point. This epoch shifting covers only one-half of the orbit ellipse due to the near-symmetry about the minor and major ellipse axes.

4.3.3 GEO Element Batch Estimation

The batch estimator is initialized for each case by interpolating the reference ephemerides to the observation epoch time. The *a priori* covariance is set to an uncertainty level of 1 kilometer in each ECI position component and 1 centimeter per second in each velocity component. To map the *a priori* covariance into the GEO element state space, 1000 randomly-sampled ECI state vectors, deviated from the truth vector according to the defined covariance, are transformed into GEO element state vectors. The error distribution mapping is performed instead of a linear covariance transformation because the relationship between the GEO elements and ECI components is very nonlinear. The distribution of the error from the expected GEO element state vector represents the *a priori* non-diagonal covariance matrix. The equations of motion are numerically integrated to propagate the satellite's orbit over the two day observation period. The dynamic model includes perturbations due to the Earth gravity field, luni-solar point mass gravity, and solar radiation pressure acting on a spherical satellite of constant reflectivity with the Earth shadow modeled cylindrically. The effective area-to-mass ratios of Anik F1R and Galaxy 15 are determined empirically.

4.3.4 Determination of Effective Area-to-Mass Ratio

The reported surface area and launch mass of Anik F1R and Galaxy 15 are shown in Table 4.3.[15; 68] Galaxy 15's surface area is not provided by Reference 68 and is assumed to be scaled by the mass ratio of Galaxy 15 to Anik F1R, a viable assumption for geosynchronous communication satellites.

Table 4.3: Physical Parameters of Anik F1R and Galaxy 15

Satellite	Area (m^2)	Mass (kg)	Reflectivity Coefficient	Effective Area-to-Mass Ratio (m^2/kg)
Anik F1R	121.25	3015	0.985	0.040
Galaxy 15	76.08	1892	0.547	0.022

A priori knowledge of the spacecraft physical parameters that affect the solar pressure per-

turbation leads to a more accurate dynamic model. The reflectivity values of high-gain antennas and solar panels, which make up the bulk of the communication spacecraft surface area, have been experimentally found to be approximately 1.2 to 1.3.[62] As the reflectivity coefficients of Anik F1R and Galaxy 15 are not perfectly known, batch estimation is used to determine an appropriate solar reflectivity coefficient for each satellite. It is expected that the reflectivity coefficients of Anik F1R and Galaxy 15 will be near the range of typical communication satellites. The Anik F1R ECEF position vector components over two days in January 2010 are processed as observations by a batch estimator to solve for the reflectivity coefficient. Given the physical parameters shown in Table 4.3, a simple cannonball with a cylindrical Earth shadow is used to model the solar pressure orbit perturbation. Additionally, a 4x4 Earth gravitational field and luni-solar third body point mass gravitational forces are included in the dynamic model. An 8x8 gravity field is known to be sufficient for most geosynchronous orbit estimation applications.[90] The inclusion of an 8x8 gravity field was investigated, and it was determined that a gravity field of order and degree larger than 4 is unnecessary due to the dynamic model accuracy limitations introduced by the solar pressure error. The 3D ECEF position error RMS value is computed and stored; the batch estimator is then re-initialized and repeated with a new reflectivity coefficient. In this manner, the batch processor sweeps through reflectivity coefficients between 0 and 2 at intervals of 0.1.

Figs. 4.4 and 4.5 present the 3D ECEF position and velocity error RMS of Anik F1R as a function of reflectivity coefficient for a more refined search grid. A reflectivity coefficient of 0.985 produces the minimum position error RMS value of 8 meters and the minimum velocity error of 3.325 millimeters per second. This reflectivity value is now assigned as Anik F1R's reflectivity coefficient throughout the remainder of the analysis. Likewise, using two days of data from May 2010, Galaxy 15's reflectivity coefficient is determined to be 0.547. Note that the reflectivity coefficient of Galaxy 15 determined with pre-failure data is approximately 0.65, indicating that Galaxy 15's solar panels may have been pointed off-nominal prior to the failure. Numerous two-day fits were performed for both Anik F1R and Galaxy 15, and the reflectivity coefficient profiles do not significantly depend on which two-day data sets are processed. The effective reflectivity coefficients

for the simplified solar radiation pressure model are lower than the more nominal values of 1.2 to 1.3 possibly due to the satellite's solar arrays not pointing directly at the sun.

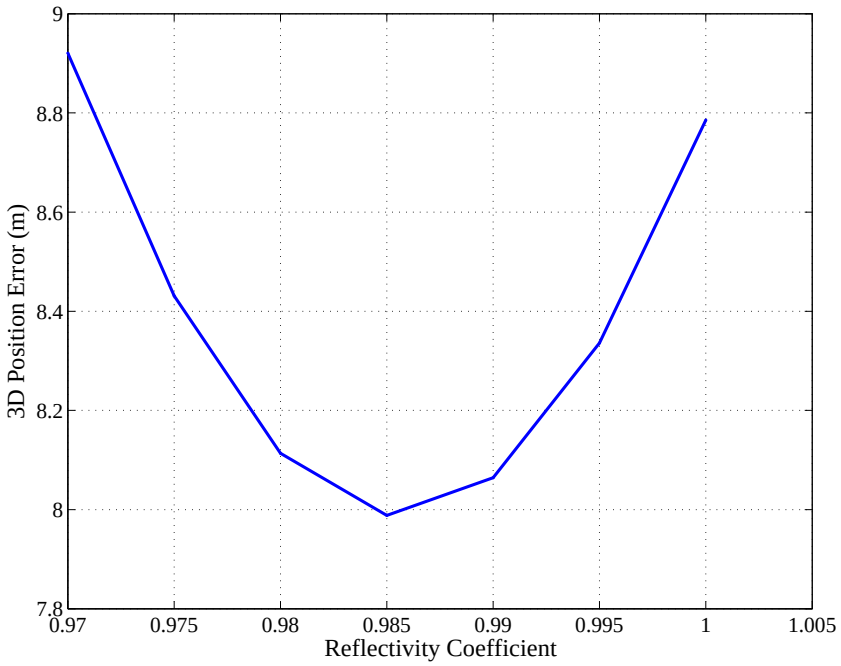

Figure 4.4: Effect of Reflectivity Coefficient on Anik F1R 3D ECEF Position Error RMS

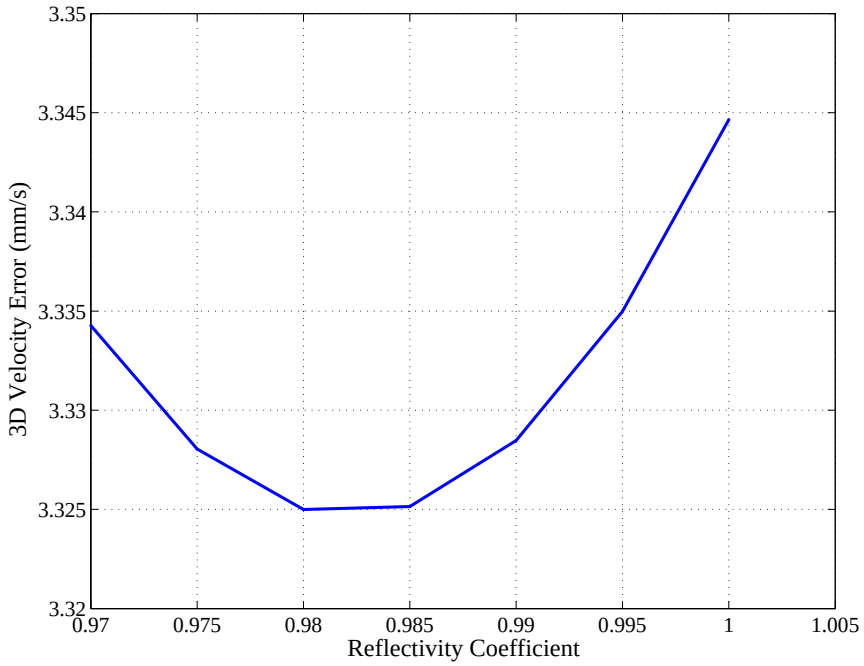

Figure 4.5: Effect of Reflectivity Coefficient on Anik F1R 3D ECEF Velocity Error RMS

4.3.5 Anik F1R and Galaxy 15 Analyses

Initially, observations of Anik F1R spanning May 2 and 3, 2010 are processed. The ECEF 3D RMS position error values for each estimate are inspected to determine the achievable estimation accuracy for a given sampling interval and track length. The impact of epoch location is analyzed by comparing the 3D position error RMS values for each epoch given a selected track length.

To best evaluate the batch performance, position solutions from the batch estimator are compared to the reference ephemerides. While the batch processor does provide a formal covariance that can be propagated to any time within the data set, the formal statistics do not capture the dynamic model uncertainty. Therefore the error distribution will be empirically determined using a large set of results for each sampling interval and track length combination. The mean error and error uncertainty are experimentally determined by processing sliding two-day data windows over the course of one month and examining the average and deviation of the estimation accuracy for each tracking parameter combination. Controlled geosynchronous satellites typically perform large stationkeeping maneuvers every one to three weeks.[90] To avoid estimation issues due to fitting over such maneuvers, the uncertainty analysis is performed by fitting to the reference observations of Galaxy 15 from May 2 to May 30, 2010. The tracking parameters of coverage arc length and sampling rate are varied as shown in Table 4.1. Due to the significant drift rate of Galaxy 15 relative to the Earth, any epoch-dependent estimation effects will be averaged out over one month and the observation epoch variation is not included in the Galaxy 15 analysis.

4.4 Analysis of Satellite Dynamics

The Anik F1R continuous two-day reference ephemeris is processed by the batch estimator in order to assess how well the dynamic model captures realistic satellite dynamics. The position and velocity component errors throughout the fit period are shown in Figs. 4.6 and 4.7. The solution error is on the order of 10 meters in all three position components, and less than 1 centimeter per second in velocity. The 3D position error RMS is 6.7 meters. The systematic difference between the

estimated solution and reference point solution is due to unmodeled dynamics; in particular, the cannonball solar pressure model is not ideal for the geometry of a GEO communication satellite, in which the surface area is typically dominated by large solar panels. The fit error lies predominantly in the Z component most likely due to the cannonball solar pressure model not incorporating out-of-plane effects.

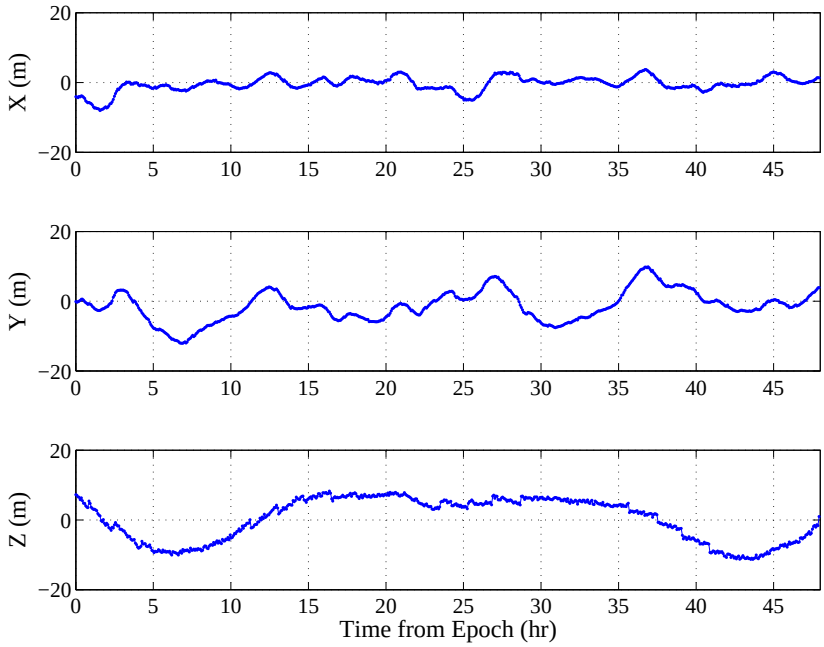

Figure 4.6: ECEF Position Error for Two Day Anik F1R Batch Estimation

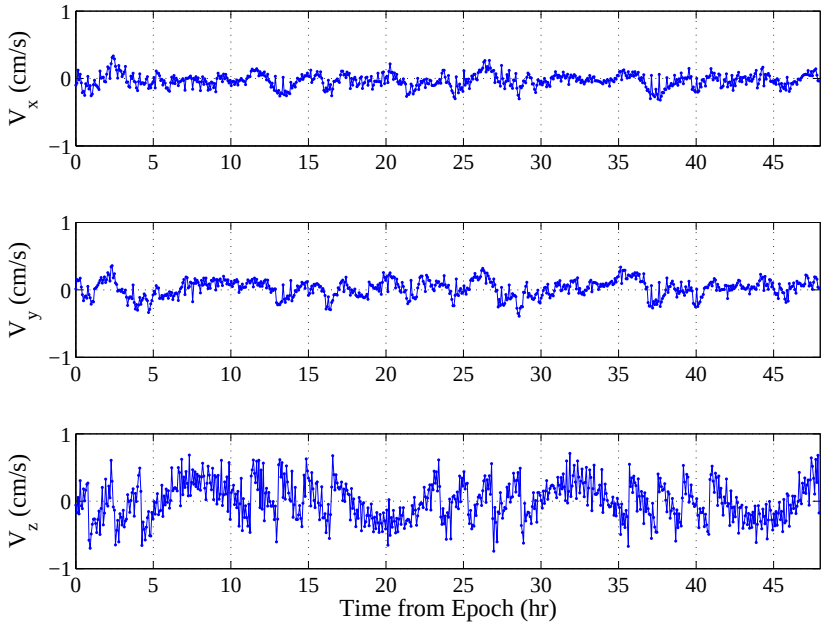

Figure 4.7: ECEF Velocity Error for Two Day Anik F1R Batch Estimation

It can be seen that the Z direction velocity error is dominated by discontinuities on the order of 1 centimeter per second. The Z position error also displays meter-level discontinuities. Since the batch solution is continuous by definition, the discontinuities must exist in the reference point solutions. Given the periodic nature of the discontinuities, it was hypothesized that they are introduced via either the estimation process used to form the WAAS reference ephemerides or by actual spacecraft maneuvers.

Inspection of the Galaxy 15 two-day batch fit error before and after the April 5, 2010 on-orbit failure allows a unique opportunity to experimentally determine the discontinuity source by contrasting fit errors for a controlled object to an identical uncontrolled object. Tenth-order polynomials are fit to Galaxy 15 one-day reference orbits before and after the spacecraft failure. Applying a general polynomial fit rather than batch estimating the fit ensures that no errors are introduced by inaccuracies of the batch dynamic model. Fig. 4.8 presents the Z component reference velocity and the detrended January 19, 2010 reference orbit, and Fig. 4.9 shows the Z component reference velocity and the detrended May 24, 2010 reference ephemeris. The velocity discontinuities are significant prior to the satellite failure, but do not exist in the post-failure data. This result indicates that the data discontinuities are due to regular maneuvers of the satellite and not to the method of data processing. It is confirmed that the Galaxy 15 reference ephemerides do not contain discontinuities after April 5, 2010.

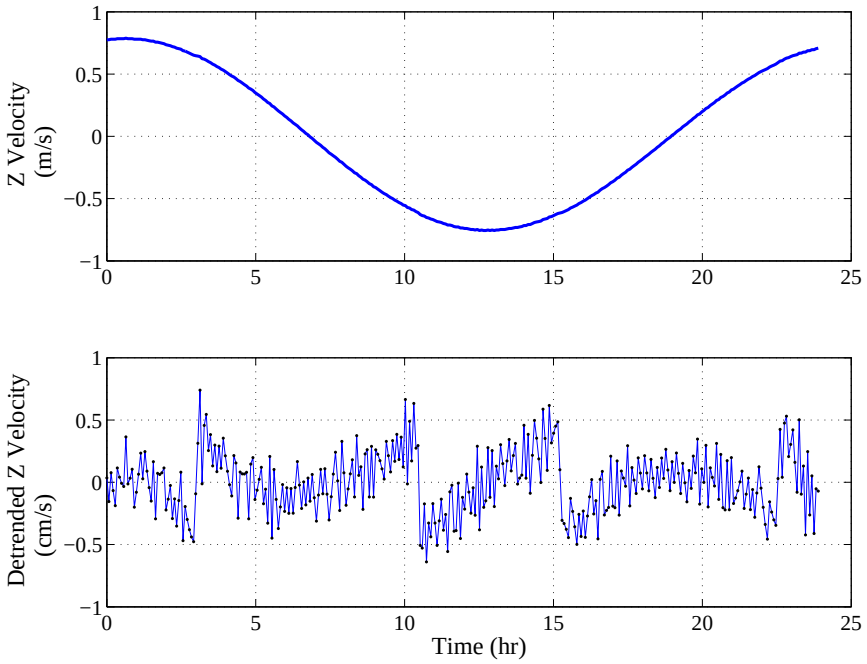

Figure 4.8: Galaxy-15 Z Velocity and Detrended Velocity (January 19, 2010)

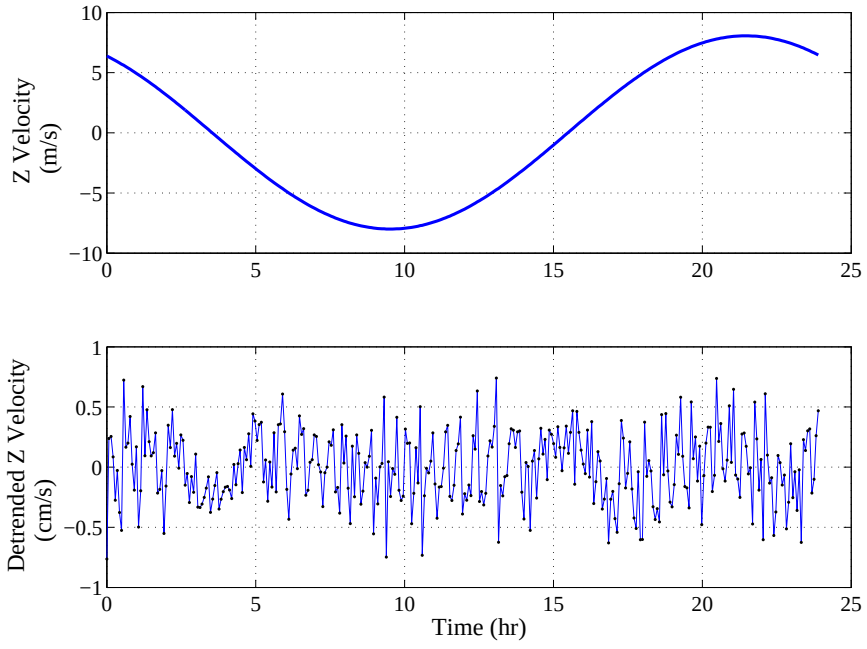

Figure 4.9: Galaxy-15 Z Velocity and Detrended Velocity (May 24, 2010)

It is of interest to note that Galaxy 15's motion out of the equatorial plane increases significantly after the spacecraft fails. Fig. 4.10 compares the Z position before (January 1, 2010) and after (May 1, 2010) the spacecraft failure. The significant increase in out-of-plane motion is primarily due to the luni-solar gravitational perturbations that are not being corrected by ground control.[90] The effect of this perturbation on the orbit inclination can be investigated by approximating the inclination as the ratio of the maximum Z position to the corresponding orbit radius. The orbit radius is computed as the norm of the ECEF position vector reported by the WAAS data files at the epoch of the maximum out-of-plane position. The pre-failure inclination is computed to be approximately 0.04 degrees, and the inclination increases to approximately 0.09 degrees by May 1. Recall that Galaxy 15 was controlled until April 5, 2010; the results show that by May 1 the orbit perturbations increased the inclination by a factor of about 2.25.

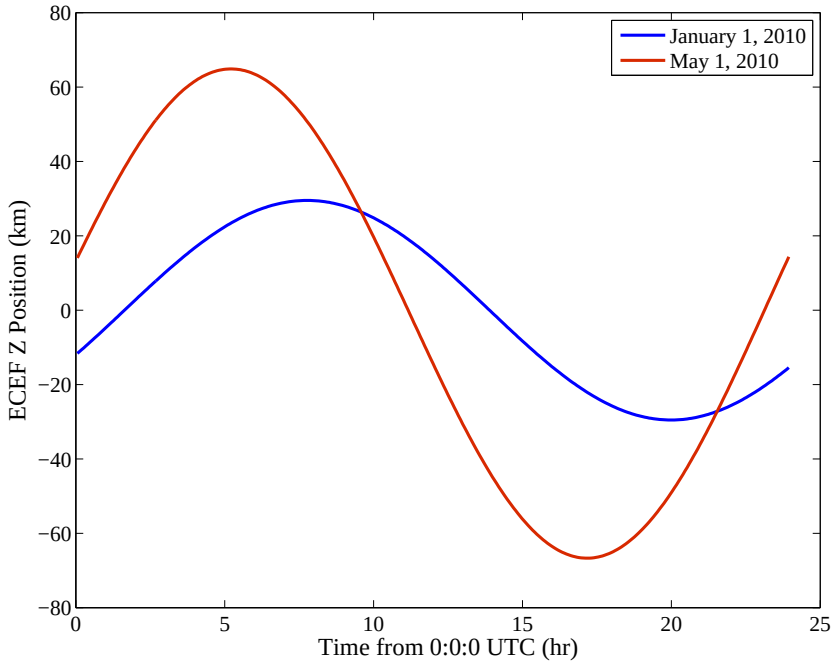

Figure 4.10: Galaxy 15 Z Position Before and After Failure

4.5 Achievable Angles-Only Orbit Estimation Accuracy

Observations of Anik F1R for May 2 through 3, 2010 are processed for all possible combinations of the tracking parameters. Two-day sliding windows of Galaxy 15 observations from May 2 through 30, 2010 are processed for all sampling intervals and nightly track length variations. Comparing the estimation accuracy for each tracking parameter combination allows for the empirical assessment of the impact of tracking duration, sampling frequency, and epoch location on estimation accuracy. Statistically assessing solutions over one month provides a metric of the solution distribution.

4.5.1 Anik F1R Analysis

Observations of Anik F1R spanning May 2 and 3, 2010 are processed to assess the estimator's performance while fitting over small, frequent maneuvers in the presence of mismodeled solar radiation pressure dynamics. The results are therefore an appropriate metric for determining the amount of tracking required for a given accuracy when observing an active geosynchronous communication satellite. The initial conditions for each epoch of May 2, 2010, produced by interpolating the reference ephemerides at the selected observation epoch, are shown in Table 4.4.

Table 4.4: Anik F1R Initial Conditions for Estimator Initialization (ECEF Frame)

Epoch (UTC on 5.2.2010)	X (km)	Y (km)	Z (km)	V_x (m/s)	V_y (m/s)	V_z (m/s)
00:01:04	-12526.484	-40255.336	-0.514	0.594	-0.693	-1.700
03:01:04	-12524.927	-40262.145	-16.777	-0.299	-0.494	-1.156
06:01:04	-12531.658	-40265.047	-23.142	-0.862	-0.037	0.036
09:01:04	-12541.629	-40263.335	-16.238	-0.912	0.319	1.175
12:01:04	-12550.042	-40258.757	-0.387	-0.594	0.503	1.609

Figure 4.11 displays the 3D ECEF position error RMS values for Epoch 1 as a function of sampling time, where the curves represents different track lengths. In general, the position error increases as coverage arc length and sampling rate decrease. Track lengths of 1 to 6 hours produce

very similar results. Ten meter accuracy is achievable at short sampling intervals of 10 seconds and at least 3 hours of nightly track length. Tracking for only 10 minutes per night produces kilometer-level accuracy. Several tracking scenarios are able to achieve orbit accuracy on the order of 100 meters. For example, tracking continuously for 30 minutes at intervals of 10 to 30 seconds achieves 100 meter accuracy, and the same accuracy can be achieved by increasing the track length while decreasing the sampling interval. A long sampling interval of 3 hours is equivalent to tracking the object once at the beginning of the night and once again at the end, and 100-meter accuracy is possible even with this limited tracking scenario.

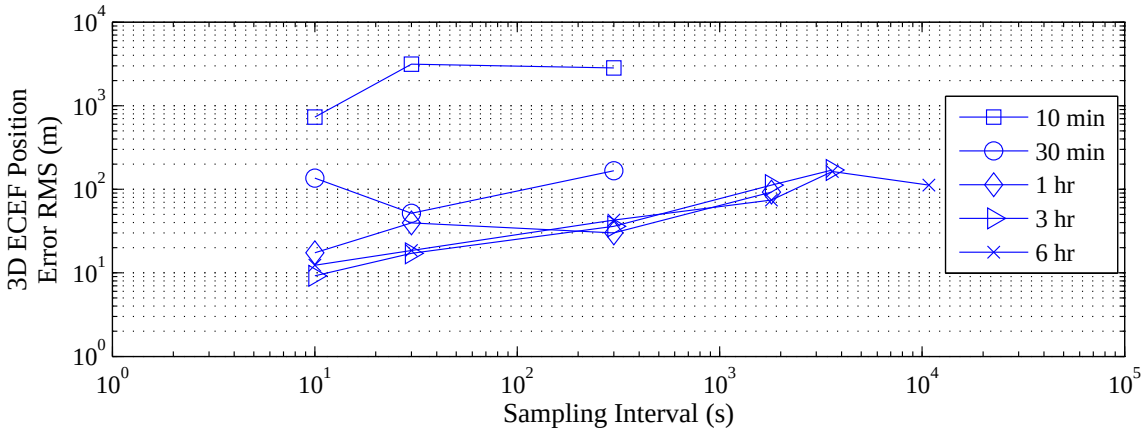

Figure 4.11: 3D ECEF Position Error RMS Value - Anik F1R

Fig. 4.12 shows the 3D position error RMS values for the five observation epochs given a nightly track length of 3 hours. Tracking beginning at each epoch will cover a different portion of the entire orbit with no overlap. It is seen that the estimation accuracy is not significantly dependent on orbit epoch. This is expected as the unmodeled solar pressure, which is the primary source of error and directly affects the orbit eccentricity, does not significantly distort any sections of the orbit over the two-day period.

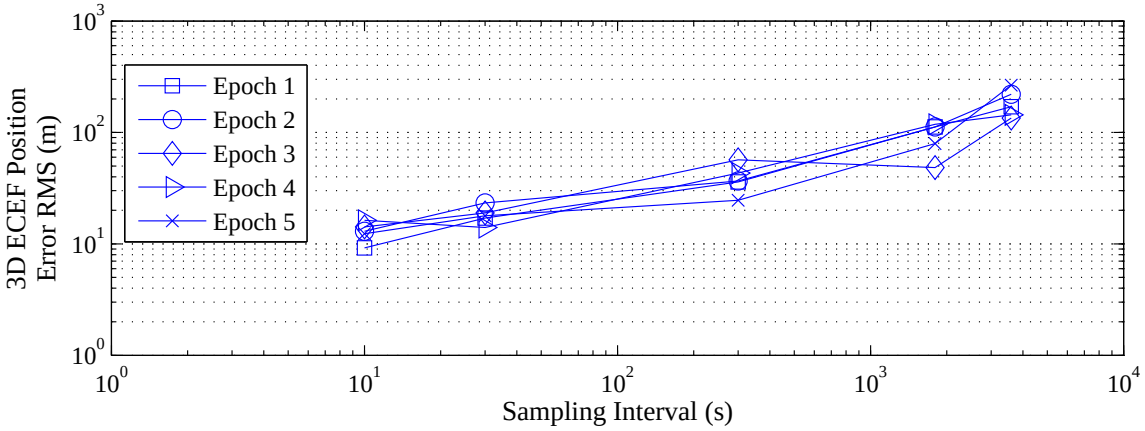

Figure 4.12: Mean 3D ECEF Position Error RMS Value for Different Epochs - Anik F1R

The Anik F1R analysis demonstrates that the batch estimator is capable of fitting over small maneuvers and can achieve excellent accuracy in the presence of realistically unmodeled dynamics. However, this analysis is a single case and provides no information regarding the solution error distribution.

4.5.2 Galaxy 15 Analysis

Next, one month of Galaxy 15 data is analyzed to avoid fitting over large stationkeeping maneuvers while providing a set of two-day solutions. The mean position error and the error uncertainty is determined experimentally by statistically assessing the mean and standard deviation of a month of two-day fits. The May 2010 reference observations of Galaxy 15 are processed in sliding two-day windows such that the estimation statistics are determined from data sets covering May 1 and 2, May 2 and 3, etc. The data from May 7, May 16 and May 31 are discarded because the reference ephemerides are indicated to be of worse accuracy than desired. The accuracy must be at worst 10 meters for the data to be accepted for this analysis.

Fig. 4.13 presents the mean 3D position error RMS values as a function of sampling interval and nightly track length. The 1σ uncertainty bounds for each track length are denoted by the dashed lines. The direct dependence of increased accuracy on shorter sampling interval and longer track length is strongly demonstrated in Fig. 4.13. The error uncertainty also decreases as the sampling interval decreases and track length increases. The uncertainty is on the order of the mean position error; for example, given a 3 hour track length and a sampling interval of 300 seconds, the mean error is approximately 100 meters with 1σ uncertainty bounds of approximately 20 meters to 200 meters.

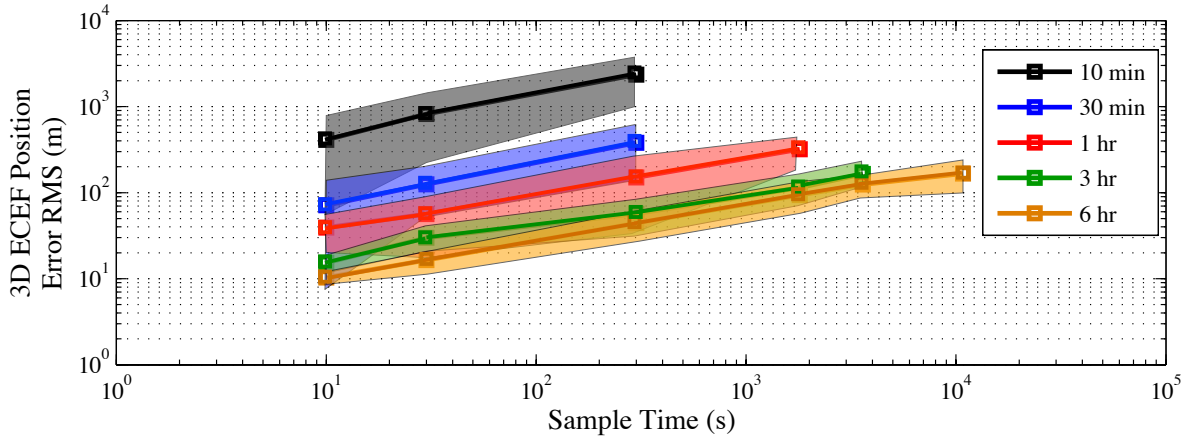

Figure 4.13: Mean 3D ECEF Position Error RMS Value and 1σ Uncertainty Bounds - Galaxy 15

The best possible accuracy is approximately 10 meters and is achievable given 6 hours of dedicated nightly tracking and a sampling interval of 10 to 30 seconds. The uncertainty for this case is on the order of a few meters. Tracking for only 10 minutes per night can produce solution accuracy on the order of several hundred meters given short sampling intervals, and this error can be reduced below 100 meters if the track length is increased to 30 minutes per night. It is shown that several tracking scenarios can meet a given accuracy requirement between approximately 10 meters and 100 meters. Finally, tracking for longer than 3 hours per night does not provide a significant improvement in orbit accuracy, and 30 minutes to 1 hour of night tracking is sufficient to meet requirements for many geosynchronous operations.[72]

4.6 Conclusions

This work has demonstrated the use of publicly-available accurate high-rate position and velocity point solutions for the characterization of geosynchronous orbit estimation accuracy given two days of ground-based optical observations. Novel case studies of two WAAS satellites, Anik F1R and Galaxy 15, enabled a true test of accuracy using realistic vehicle motions for both controlled and drifting vehicles. As expected, longer tracking arcs and shorter observation intervals generally produced more accurate results; however, it was shown that arc lengths in excess of 3 hours and intervals shorter than 30 seconds have only marginal benefit. We estimate that 10-meter orbits can be readily generated using at least 3 hours of observations at intervals of at most 30 seconds for two nights, and 100 meter accuracy can be produced using at least 30 minutes of observations at intervals of 30 seconds.

These findings provide useful information for ground telescope operator planning, allowing for multiple geosynchronous objects to be tracked by a non-dedicated sensor over the course of the night without compromising accuracy. Short-term tracking is extremely useful when the sensor is unable to track the target object for longer than two days, such as when weather interrupts, or when an orbit solution is required in a short period of time.

Chapter 5

Space-Based Angles-Only Tracking

5.1 Introduction

Space-based optical tracking of spacecraft is a desirable capability for relative motion missions including spacecraft formation maintenance, rendezvous and docking, and passive tracking for orbit estimation. Optical sensors are attractive for spacecraft operations as they are typically small and lightweight and can be extremely useful for on-board autonomous navigation.[13; 14; 20; 51; 93; 74] As such, relative spacecraft state estimation given space-based angles-only observations has received much attention in recent years.[18; 49; 86; 111; 112; 116]

Woffinden, et. al. [112] demonstrated that the position of a deputy spacecraft relative to a chief spacecraft is not observable when processing optical observations and modeling the relative motion via the rectilinear Hill's (Clohessy-Wiltshire)[32; 22] model of linearized Keplerian relative motion. The linear representation of the in-plane dynamics combined with the rectilinear coordinate representation of the angular measurements resulted in a system in which the intersatellite range is not estimable. The lack of observability can only be overcome by breaking the constraint of a linear measurement model combined with a linearized dynamic model.

Several methods have been investigated to mitigate the Hill's observability issue when only optical data are available. Woffinden, et. al. [112] showed that maneuvering one satellite provided enough observability to recover the full relative state, including the along-track separation. Follow-on work by Woffinden, et. al. [113; 114] developed criteria to determine the optimal maneuvering to enhance the observability conditions, and demonstrated observability by including differential

perturbations. To produce a partial solution that does not involve spacecraft maneuvers, Schmidt, et. al. [86] substituted a set of elements describing the elliptical motion of the deputy relative to the chief into the rectilinear Hill's Keplerian dynamic model. A set of perfect unique measurement equations were then solved for a subset of relative elements. While the relative elements were not fully observable, Schmidt, et. al. showed that an element subset can determine a family of orbits to which the tracked spacecraft belongs.

The concept of introducing observability of a state of one craft relative to another via maneuvers has also been explored in the context of underwater craft formations. Hammel, et. al. [30] investigated the observability requirements given bearings-only (angles-only) tracking data, and developed a framework for how the chief craft must maneuver in order for the relative state to become observable. Hammel outlined a special case for which chief maneuvering is not required: when the relative craft depth is a known constant, the number of estimated states is reduced and the remaining states may be recovered.

Relevant work has also been conducted in the estimation of deputy and chief spacecraft inertial position and velocity vectors given relative line-of-sight measurements.[18; 49; 116] Yim, et. al. [116] looked specifically at satellites in high eccentricity and inclination Low Earth Orbits. The authors demonstrated the full observability of a two-spacecraft system when only Keplerian dynamics were modeled and the spacecraft were in co-planar orbits, provided the inclination was non-zero for both spacecraft and the eccentricity was non-zero for at least one of the spacecraft. The inclusion of the J_2 perturbation was shown to increase the level of observability due to the introduction of relative out-of-plane motion.

Qiang [54] presented a similar orbit estimation simulation study. For the case of a high-altitude satellite tracking a low-altitude satellite in a circular orbit, the J2000 ECI frame position and velocity vectors of the low-altitude satellites were recovered by processing angles-only azimuth and elevation measurements with an EKF. The primary goal of this work was to demonstrate that the ECI state of a satellite in a circular, low-altitude orbit is observable given space-based angles-only measurements. The spacecraft were not in co-planar orbits and the high-altitude spacecraft's

orbit eccentricity was 0.1. In addition to demonstrating the feasibility of this tracking concept through simulation studies, the measurement sensitivity matrix and state transition matrix were clearly developed and presented.

This section explores the full observability of the relative GEO elements of two objects in Keplerian orbits using only space-based angular measurements and a spherical coordinate representation of the relative position. Employing the spherical measurement model effectively breaks the linear relationship of the measurement model and relative dynamics, resulting in the ability to fully recover the relative spacecraft state. The following sections show that by using spherical rather than rectilinear coordinates, the relative state can be observed for two spacecraft in close proximity, provided that there exists some time-varying relative motion. First, the spherical coordinate relative dynamic model is derived in terms of the relative GEO elements. A nonlinear model of space-based azimuth and elevation measurements is then developed in terms of the spherical coordinates. Given unique observations at several epochs and a batch estimator designed to solve for the epoch relative GEO elements based on a linearized dynamic model of the unperturbed relative motion, the observability Gramian is derived and the observability analytically assessed. Numerical studies are performed to demonstrate the observability of the full relative state. Finally, the impact of linearizing the spherical relative coordinates is investigated.

5.2 Spherical Coordinate Representation of Relative Motion

Fig. 5.1 presents a graphical representation of a rectilinear and spherical coordinates of a deputy spacecraft relative to the chief spacecraft for two Earth-orbiting closely-located spacecraft. The rectilinear Cartesian coordinates ($\begin{bmatrix} x' & y' & z' \end{bmatrix}$) are defined in the Local Vertical Local Horizontal (LVLH) frame centered at the chief. The spherical coordinates ($\begin{bmatrix} x & y & z \end{bmatrix}$) are defined by the projection of the deputy spacecraft onto a sphere centered on the Earth and with radius equal to the chief spacecraft's orbital radius. The x coordinate is the perpendicular distance between the surface of the reference sphere and the true deputy location, y is the curvilinear along-track

separation, and z is the curvilinear out-of-plane separation.[52]

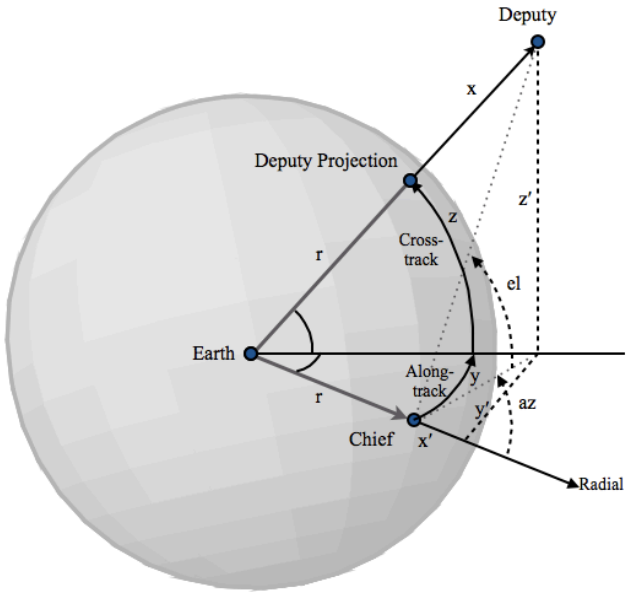

Figure 5.1: Relative Coordinates as Defined in the Chief LVLH Reference Frame

A linearized, two-body dynamic model for spherical coordinate propagation, analogous to the Hill's linearized relative motion model is next derived in terms of the relative GEO elements. The relative GEO element state is defined as the difference between the deputy and chief GEO element sets.

$$\Delta\vec{\lambda} = \begin{bmatrix} \Delta\lambda & \Delta\delta\bar{a} & \Delta e_y & \Delta e_x & \Delta Q_1 & \Delta Q_2 \end{bmatrix}^T = \vec{\lambda}_d - \vec{\lambda}_c \tag{5.1}$$

Assuming small orbit deviations from the chief spacecraft, the spherical coordinate dynamic model is obtained by deriving the sensitivity of the spherical relative position components with respect to the epoch relative GEO elements.[52] The development begins by determining the sensitivity of the ECI (Earth-Centered Inertial) position vector components to the GEO elements via linearizing the position vector about the chief spacecraft's GEO elements at the epoch.

The ECI position vector is defined in terms of the GEO elements at time t as:

$$\vec{r} = \begin{bmatrix} X \\ Y \\ Z \end{bmatrix} = \frac{r}{1+Q_1^2+Q_2^2} \begin{bmatrix} \cos s + (Q_2^2 - Q_1^2)\cos s + 2Q_1Q_2 \sin s \\ \sin s + (Q_1^2 - Q_2^2)\sin s + 2Q_1Q_2 \cos s \\ 2Q_2 \sin s - 2Q_1 \cos s \end{bmatrix} \tag{5.2}$$

where s is the spacecraft sidereal angle ($s = \lambda + GA$). The sensitivity matrix S_{ECI}, constructed by the partial derivatives of the position vector with respect to the estimated states, is given by:

$$S_{ECI} = \begin{bmatrix} \frac{\partial \vec{r}}{\partial \lambda} & \frac{\partial \vec{r}}{\partial \delta \bar{a}} & \frac{\partial \vec{r}}{\partial e_y} & \frac{\partial \vec{r}}{\partial e_x} & \frac{\partial \vec{r}}{\partial Q_1} & \frac{\partial \vec{r}}{\partial Q_2} \end{bmatrix} \tag{5.3}$$

Partial differentiation of Eq. 5.2 with respect to each of the GEO elements produces the following:

$$\frac{\partial X}{\partial \lambda} = \frac{a(1-e_y^2-e_x^2)\left[-e_y + e_yQ_1^2 + 2e_xQ_1Q_2 - e_yQ_2^2 + 2Q_1Q_2\cos s + (Q_1^2 - Q_2^2 - 1)\sin s\right]}{(1+Q_1^2+Q_2^2)(1+e_y\sin s + e_x \cos s)^2} \tag{5.4}$$

$$\frac{\partial Y}{\partial \lambda} = \frac{a(1-e_y^2-e_x^2)\left[e_x + e_xQ_1^2 - 2e_yQ_1Q_2 - e_xQ_2^2 - 2Q_1Q_2\sin s - (Q_2^2 - Q_1^2 - 1)\cos s\right]}{(1+Q_1^2+Q_2^2)(1+e_y\sin s + e_x \cos s)^2} \tag{5.5}$$

$$\frac{\partial Z}{\partial \lambda} = \frac{2a(1-e_y^2-e_x^2)\left[e_yQ_1 + e_xQ_2 + Q_2\cos s + Q_1 \sin s\right]}{(1+Q_1^2+Q_2^2)(1+e_y\sin s + e_x \cos s)^2} \tag{5.6}$$

$$\frac{\partial X}{\partial \delta \bar{a}} = \frac{A(1-e_y^2-e_x^2)\left[(1+Q_2^2-Q_1^2)\cos s + 2Q_1Q_2\sin s\right]}{(1+Q_1^2+Q_2^2)(1+e_y\sin s + e_x \cos s)} \tag{5.7}$$

$$\frac{\partial Y}{\partial \delta \bar{a}} = \frac{A(1-e_y^2-e_x^2)\left[(1-Q_2^2+Q_1^2)\sin s + 2Q_1Q_2\cos s\right]}{(1+Q_1^2+Q_2^2)(1+e_y\sin s + e_x \cos s)} \tag{5.8}$$

$$\frac{\partial Z}{\partial \delta \bar{a}} = \frac{2A(1-e_y^2-e_x^2)\left[Q_2\sin s - Q_1 \cos s\right]}{(1+Q_1^2+Q_2^2)(1+e_y\sin s + e_x \cos s)} \tag{5.9}$$

$$\frac{\partial X}{\partial e_y} = \frac{a\left[2e_y + 2e_ye_x\cos s + (1+e_y^2-e_x^2)\sin s\right]\left[(Q_1^2 - Q_2^2 - 1)\cos s - 2Q_1Q_2\sin s\right]}{(1+Q_1^2+Q_2^2)(1+e_y\sin s + e_x \cos s)^2} \tag{5.10}$$

$$\frac{\partial Y}{\partial e_y} = \frac{-a\left[2e_y + 2e_ye_x\cos s + (1+e_y^2-e_x^2)\sin s\right]\left[(Q_1^2 - Q_2^2 + 1)\sin s + 2Q_1Q_2\cos s\right]}{(1+Q_1^2+Q_2^2)(1+e_y\sin s + e_x \cos s)^2} \tag{5.11}$$

$$\frac{\partial Z}{\partial e_y} = \frac{2a\left[2e_y + 2e_ye_x\cos s + (1+e_y^2-e_x^2)\sin s\right]\left[Q_1\cos s - Q_2\sin s\right]}{(1+Q_1^2+Q_2^2)(1+e_y\sin s + e_x \cos s)^2} \tag{5.12}$$

$$\frac{\partial X}{\partial e_x} = \frac{a\left[2e_x + 2e_ye_x\sin s + (1-e_y^2+e_x^2)\cos s\right]\left[(Q_1^2 - Q_2^2 - 1)\cos s - 2Q_1Q_2\sin s\right]}{(1+Q_1^2+Q_2^2)(1+e_y\sin s + e_x \cos s)^2} \tag{5.13}$$

$$\frac{\partial Y}{\partial e_x} = \frac{-a\left[2e_x + 2e_ye_x\sin s + (1-e_y^2+e_x^2)\cos s\right]\left[(Q_1^2 - Q_2^2 + 1)\sin s + 2Q_1Q_2\cos s\right]}{(1+Q_1^2+Q_2^2)(1+e_y\sin s + e_x \cos s)^2} \tag{5.14}$$

$$\frac{\partial Z}{\partial e_x} = \frac{2a\left[2e_x + 2e_y e_x \sin s + (1 - e_y^2 + e_x^2)\cos s\right]\left[Q_1 \cos s - Q_2 \sin s\right]}{(1 + Q_1^2 + Q_2^2)(1 + e_y \sin s + e_x \cos s)^2} \tag{5.15}$$

$$\frac{\partial X}{\partial Q_1} = \frac{-2a(1 - e_y^2 - e_x^2)\left[2Q_1(1 + Q_2^2)\cos s + Q_2(Q_1^2 - Q_2^2 - 1)\sin s\right]}{(1 + Q_1^2 + Q_2^2)^2(1 + e_y \sin s + e_x \cos s)} \tag{5.16}$$

$$\frac{\partial Y}{\partial Q_1} = \frac{2a(1 - e_y^2 - e_x^2)\left[2Q_1 Q_2^2 \sin s + Q_2(Q_2^2 - Q_1^2 + 1)\cos s\right]}{(1 + Q_1^2 + Q_2^2)^2(1 + e_y \sin s + e_x \cos s)} \tag{5.17}$$

$$\frac{\partial Z}{\partial Q_1} = \frac{2a(1 - e_y^2 - e_x^2)\left[-2Q_1 Q_2 \sin s + (Q_1^2 - Q_2^2 - 1)\cos s\right]}{(1 + Q_1^2 + Q_2^2)^2(1 + e_y \sin s + e_x \cos s)} \tag{5.18}$$

$$\frac{\partial X}{\partial Q_2} = \frac{2a(1 - e_y^2 - e_x^2)\left[2Q_1^2 Q_2 \cos s + Q_1(Q_1^2 - Q_2^2 + 1)\sin s\right]}{(1 + Q_1^2 + Q_2^2)^2(1 + e_y \sin s + e_x \cos s)} \tag{5.19}$$

$$\frac{\partial Y}{\partial Q_2} = \frac{2a(1 - e_y^2 - e_x^2)\left[-2(1 + Q_1^2)Q_2 \sin s + Q_1(Q_1^2 - Q_2^2 + 1)\cos s\right]}{(1 + Q_1^2 + Q_2^2)^2(1 + e_y \sin s + e_x \cos s)} \tag{5.20}$$

$$\frac{\partial Z}{\partial Q_2} = \frac{2a(1 - e_y^2 - e_x^2)\left[2Q_1 Q_2 \cos s + (Q_1^2 - Q_2^2 + 1)\sin s\right]}{(1 + Q_1^2 + Q_2^2)^2(1 + e_y \sin s + e_x \cos s)} \tag{5.21}$$

Reference 104 investigated the amount of relative state observability provided by various relative motion scenarios, and it was shown that increased relative motion produces increased observability. Objects in circular, co-planar leader-follower orbits exhibit less pronounced relative motion than objects with different eccentricities, and as such this relative motion configuration possess the more limiting observability conditions. Furthermore, the out-of-plane relative motion is dictated by the differential inclination, and two objects with a certain Δi value display the same relative motion independently of the chief inclination. It is now assumed that the chief spacecraft is in a zero eccentricity, zero inclination orbit in order to obtain a simplified set of partial derivatives, but the validity of this analysis is not limited to this simplified case. The ECI sensitivity matrix for a circular equatorial chief orbit is reduced to:

$$S_{ECI} = \begin{bmatrix} -a\sin s & A\cos s & -a\sin s\cos s & -a\cos^2 s & 0 & 0 \\ a\cos s & A\sin s & -a\sin^2 s & -a\cos s\sin s & 0 & 0 \\ 0 & 0 & 0 & 0 & -2a\cos s & 2a\sin s \end{bmatrix} \tag{5.22}$$

The ECI sensitivity matrix is transformed into the spherical RSW (Radial, Along-Track, Cross-track) reference frame by:[103]

$$S_{RSW} = TS_{ECI} \tag{5.23}$$

in which

$$T = \begin{bmatrix} \cos\Omega\cos\theta - \sin\Omega\cos i\sin\theta & \sin\Omega\cos\theta + \cos\Omega\cos i\sin\theta & \sin i\sin\theta \\ -\cos\Omega\sin\theta - \sin\Omega\cos i\cos\theta & -\sin\Omega\sin\theta + \cos\Omega\cos i\cos\theta & \sin i\cos\theta \\ \sin\Omega\sin i & -\cos\Omega\sin i & \cos i \end{bmatrix} \tag{5.24}$$

Assuming small deviations from the chief spacecraft's GEO elements, the spherical relative position coordinates are defined as:

$$\vec{x} = S_{RSW}\Delta\vec{\lambda} = TS_{ECI}\Delta\vec{\lambda} \tag{5.25}$$

The spherical relative position coordinates at time t are mapped to the epoch relative GEO element state via the state transition matrix, which is derived by linearizing the Keplerian dynamic model about the chief spacecraft. Given a chief spacecraft with zero eccentricity, the GEO element state transition matrix is defined as:[98]

$$\Phi(t,t_0) = \begin{bmatrix} 1 & -\frac{3n(t-t_0)}{2(\delta\bar{a}+1)} & 0 & 0 & 0 & 0 \\ 0 & 1 & 0 & 0 & 0 & 0 \\ 0 & 0 & 1 & 0 & 0 & 0 \\ 0 & 0 & 0 & 1 & 0 & 0 \\ 0 & 0 & 0 & 0 & 1 & 0 \\ 0 & 0 & 0 & 0 & 0 & 1 \end{bmatrix} \tag{5.26}$$

The spherical relative dynamic model given a circular equatorial chief orbit is now defined as:

$$x = A\Delta\delta\bar{a} - a\sin s\Delta e_y - a\cos s\Delta e_x \tag{5.27}$$

$$y = a\Delta\lambda_0 - \frac{3na(t-t_0)}{2(\delta\bar{a}+1)}\Delta\delta\bar{a} \tag{5.28}$$

$$z = -2a\cos s\Delta Q_1 + 2a\sin s\Delta Q_2 \tag{5.29}$$

$$\dot{x} = -an\cos s\Delta e_y + an\sin s\Delta e_x \tag{5.30}$$

$$\dot{y} = \frac{-3na}{2(\delta\bar{a}+1)}\Delta\delta\bar{a} \tag{5.31}$$

$$\dot{z} = 2an\sin s\Delta Q_1 + 2an\cos s\Delta Q_2 \tag{5.32}$$

Note that the spherical coordinate relative dynamic model presented in Eqs. 5.27 through 5.32 has been derived by applying the same assumptions as the Hill's relative motion model: the dynamics are linearized for small deviations from the chief spacecraft, the two spacecraft are in unperturbed orbits, and the chief spacecraft is in a circular orbit. Furthermore, the chief spacecraft is assumed to be in a zero inclination orbit.

5.3 Space-Based Optical Measurements

The space-based angular measurements used for this analysis are the azimuth and elevation measurements defined in the chief spacecraft's LVLH frame. As shown in Fig. 5.1, the azimuth measures the in-plane angular separation while the elevation measures the out-of-plane separation.

The angular measurements are defined in terms of the rectilinear Hill's coordinates as:

$$\vec{G}(\vec{X},t) = \begin{bmatrix} \tan(az) \\ \tan(el) \end{bmatrix} = \begin{bmatrix} \frac{y'}{x'} \\ \frac{z'}{\sqrt{(x')^2+(y')^2}} \end{bmatrix} \tag{5.33}$$

The measurements need to be expressed in terms of the spherical coordinates to connect the measurement and dynamic models. As shown in Fig. 5.1, the spherical coordinates are geometrically related to the rectilinear coordinates by:

$$x' = [r+x]\cos\frac{z}{r}\cos\frac{y}{r} - r \tag{5.34}$$

$$y' = [r+x]\cos\frac{z}{r}\sin\frac{y}{r} \tag{5.35}$$

$$z' = [r+x]\sin\frac{z}{r} \tag{5.36}$$

The angular measurements are expressed in terms of the spherical coordinates as:

$$\vec{G}(\vec{X},t) = \begin{bmatrix} \tan(az) \\ \tan(el) \end{bmatrix} = \begin{bmatrix} \frac{[r+x]\cos\frac{z}{r}\sin\frac{y}{r}}{[r+x]\cos\frac{z}{r}\cos\frac{y}{r}-r} \\ \frac{[r+x]\sin\frac{z}{r}}{\left([r+x]^2\cos^2\frac{z}{r}-2r[r+x]\cos\frac{z}{r}\cos\frac{y}{r}+r^2\right)^{1/2}} \end{bmatrix} \tag{5.37}$$

5.4 Batch Estimator Measurement Sensitivity Matrix

Batch estimation accumulates information from a time series of measurements to determine an estimate of the state at the epoch time.[95] This section derives the measurement sensitivity matrix that is accumulated for a batch estimator recovering the epoch relative GEO element state. The sensitivity of the measurements to the estimated states is defined as:

$$\tilde{H} = \frac{\partial \vec{G}}{\partial \Delta \vec{\lambda}_0} = \frac{\partial \vec{G}}{\partial \vec{x}} \frac{\partial \vec{x}}{\partial \Delta \vec{\lambda}_0} \tag{5.38}$$

The partial derivatives of the measurement model with respect to the epoch relative GEO elements are given by:

$$\frac{\partial \tan(az)}{\partial \Delta \lambda_0} = \frac{a(r+x)\cos\frac{z}{r}\left(-r\cos\frac{y}{r} + (r+x)\cos\frac{z}{r}\right)}{r(x')^2} \tag{5.39}$$

$$\frac{\partial \tan(az)}{\partial \Delta \delta\bar{a}} = \frac{-rA\cos\frac{z}{r}\sin\frac{y}{r}}{(x')^2} - \frac{3an(t_1)(r+x)\cos\frac{z}{r}\left(-r\cos\frac{y}{r} + (r+x)\cos\frac{z}{r}\right)}{2r(\delta\bar{a}+1)(x')^2} \tag{5.40}$$

$$\frac{\partial \tan(az)}{\partial \Delta e_y} = \frac{-ra\sin s\cos\frac{z}{r}\sin\frac{y}{r}}{(x')^2} \tag{5.41}$$

$$\frac{\partial \tan(az)}{\partial \Delta e_x} = \frac{-ra\cos s\cos\frac{z}{r}\sin\frac{y}{r}}{(x')^2} \tag{5.42}$$

$$\frac{\partial \tan(az)}{\partial \Delta Q_1} = \frac{-2a\cos s(r+x)\sin\frac{y}{r}\sin\frac{z}{r}}{(x')^2} \tag{5.43}$$

$$\frac{\partial \tan(az)}{\partial \Delta Q_2} = \frac{2a\sin s(r+x)\sin\frac{y}{r}\sin\frac{z}{r}}{(x')^2} \tag{5.44}$$

$$\frac{\partial \tan(el)}{\partial \Delta \lambda_0} = \frac{-a(r+x)^2\sin\frac{y}{r}\sin\frac{2z}{r}}{2\left((x')^2+(y')^2\right)^{3/2}} \tag{5.45}$$

$$\frac{\partial \tan(el)}{\partial \Delta \delta\bar{a}} = \frac{Ar\sin\frac{z}{r}\left((r+x)\cos\frac{y}{r}\cos\frac{z}{r} - r\right)}{\left((x')^2+(y')^2\right)^{3/2}} - \frac{3an(t_1)(r+x)^2\sin\frac{y}{r}\sin\frac{2z}{r}}{2(\delta\bar{a}+1)\left((x')^2+(y')^2\right)^{3/2}} \tag{5.46}$$

$$\frac{\partial \tan(el)}{\partial \Delta e_y} = \frac{-a\sin sr\sin\frac{z}{r}\left((r+x)\cos\frac{y}{r}\cos\frac{z}{r} - r\right)}{\left((x')^2+(y')^2\right)^{3/2}} \tag{5.47}$$

$$\frac{\partial \tan(el)}{\partial \Delta e_x} = \frac{-a\cos sr \sin\frac{z}{r}\left((r+x)\cos\frac{y}{r}\cos\frac{z}{r} - r\right)}{\left((x')^2+(y')^2\right)^{3/2}} \tag{5.48}$$

$$\frac{\partial \tan(el)}{\partial \Delta Q_1} = \frac{-2a\cos s(r+x)}{2r\left((x')^2+(y')^2\right)^{3/2}} \times \left(2\left[2r^2+2rx+x^2\right]\cos\frac{z}{r} - r(r+x)\cos\frac{y}{r}\left[3+\cos\frac{2z}{r}\right]\right) \tag{5.49}$$

$$\frac{\partial \tan(el)}{\partial \Delta Q_2} = \frac{2a\sin s(r+x)}{2r\left((x')^2+(y')^2\right)^{3/2}} \times \left(2\left[2r^2+2rx+x^2\right]\cos\frac{z}{r} - r(r+x)\cos\frac{y}{r}\left[3+\cos\frac{2z}{r}\right]\right) \tag{5.50}$$

The system observability is now assessed by inspecting the accumulated measurement sensitivity matrix comprised of the partial derivatives shown in Eqs. 5.39 through 5.50, assuming that measurements are processed at three unique times. The rows and columns of the accumulated measurement sensitivity matrix are linearly independent provided that at least one relative position component varies with time, and that the chief spacecraft sidereal angles at the measurement times are not spaced by integer multiples of 180 degrees. Examples of observable relative motion geometries include objects in orbits of different eccentricities (x is time-varying), two objects in the same elliptic orbit, separated in longitude (y is time-varying), and two objects in the circular orbits of the same altitude, separated in both longitude and inclination (z is time-varying). The accumulated measurement sensitivity matrix row and column linear independence demonstrates that the system is fully observable.

An example of a scenario that is not observable is the degenerate case of two objects in the same circular orbit and separated by a longitudinal displacement (i.e., circular leader-follower relative motion). Given this relative configuration, x and y are constants, and z is zero for all time. The first two columns of the accumulated measurement sensitivity matrix (representing the

azimuth and elevation measurement sensitivity to $\Delta\lambda_0$ and $\Delta\delta\bar{a}$) are of the form:

$$\begin{bmatrix} k_1 & 0 & k_1 & 0 & k_1 & 0 \\ \sim k_2 & 0 & \sim k_2 & 0 & \sim k_2 & 0 \end{bmatrix}^T \tag{5.51}$$

in which k_1 and k_2 are some constant value. Note that assuming small deviations from the chief spacecraft, the time-variation of the partial derivative $\frac{\partial \tan(az)}{\partial \Delta\delta\bar{a}}$ is negligible. The first two columns of the measurement sensitivity matrix are linearly dependent and the system is not fully observable. This observability issue is overcome by the introduction of a time-varying spherical position coordinate, whether it be x, y, and z.

5.5 Numerical Verification of Relative GEO Element Observability

In practice, the batch estimator accumulates the measurement sensitivity matrix at each measurement time. The rank of the accumulated matrix must be equal to the number of estimated states in order for the system to be observable. This work assesses the observability of the full relative GEO element state vector via numerical simulation. A simulation is performed in which the measurement sensitivity matrix is accumulated over a series of measurement times. The initial conditions of the chief spacecraft and the GEO element differences between chief and deputy are shown in Table 5.1. The chief is in a circular equatorial orbit, as implied by $P_1 = P_2 = Q_1 = Q_2 = 0$. The deputy is also in a circular orbit at the same altitude, and a non-zero relative inclination is defined. The measurement noise is assumed to have a Gaussian distribution with a standard deviation of 4 arcseconds about zero mean. The relative motion is bounded, and the differential inclination is non-zero to ensure sufficient observability. The relative orbit elements result in an along-track separation of approximately 26 kilometers.

Table 5.1: Simulation Initial Conditions

	λ (rad)	$\delta\bar{a}$	e_x	e_y	Q_1	Q_2
Chief Elements	4.636645	-2 x 10^{-6}	0	0	0	0
Deputy Relative Elements	5.85 x 10^{-4}	0	0	0	1.5 x 10^{-5}	8.73 x 10^{-4}

Measurements are assumed to be collected every minute over 1 day for a total of 1440 measurement pairs. An *a priori* covariance of 5×10^{-10} is set for each relative GEO element. The *a priori* uncertainty is approximately 2 kilometers in position and 20 centimeters per second in velocity. The H matrix is accumulated and the covariance is estimated at each measurement time. At the end of 1 day, the rank of the total accumulated measurement sensitivity matrix is 6, and the condition number is approximately 2000. Furthermore, the covariance of each element decreases from its *a priori* value (Fig. 5.2 shows the 1σ estimated uncertainty), demonstrating that additional measurements provide further information regarding the relative state. As expected, given the difficulty in recovering intersatellite range with optical observations only[112; 114], the uncertainty of the GEO elements that are defined by the along-track separation, $\Delta\lambda$, ΔQ_1, and ΔQ_2, requires the most time and observations to significantly decrease. The measurement sensitivity matrix rank and covariance profile demonstrate that the relative GEO elements are fully observable using only space-based angular observations.

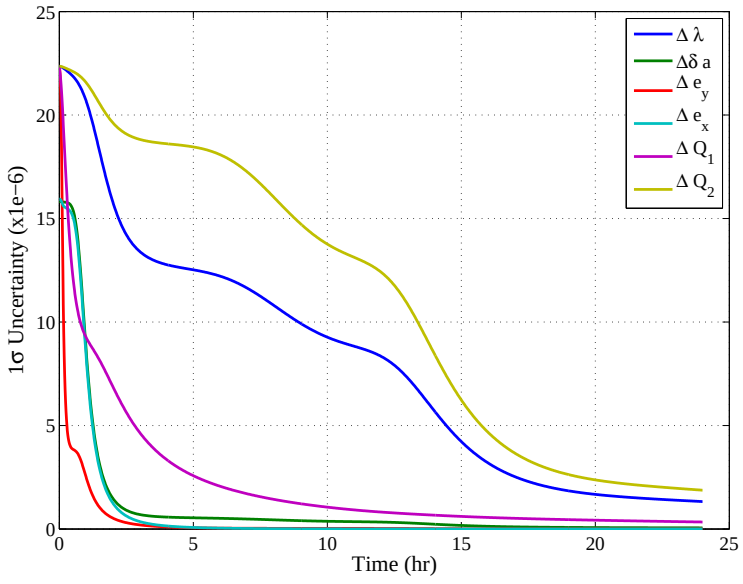

Figure 5.2: Relative GEO Element 1σ Estimated Uncertainty

5.6 Linearization of Spherical Measurement Equations

To illustrate the fact that the spherical representation is what allows for observability, we can show how the spherical case degenerates to the problematic rectilinear solution when the spherical coordinates are linearized for small x, y, and z. The azimuth measurement is approximated by:

$$\tan(az) \approx \frac{y}{x} \tag{5.52}$$

which essentially equates the spherical and rectilinear representations of the azimuth measurement model. In order to assess the observability, four unique azimuth measurement equations are solved for the four in-plane relative GEO elements ($\Delta\lambda_0$, $\Delta\delta\bar{a}$, Δe_y, and Δe_x). Using the linearized Keplerian dynamic model shown in Eqs. 5.27 through 5.29, the azimuth measurement at a given time t_j is expressed in terms of the epoch state as:

$$\tan(az(t_j)) \approx \frac{a\Delta\lambda_0}{A\Delta\delta\bar{a} - a\sin s(t_j)\Delta e_y - a\cos s(t_j)\Delta e_x}, j = 1...4 \tag{5.53}$$

Simultaneously solving the four azimuth measurement equations for the in-plane elements results in a solution that is of the form:

$$\tan(az(t_4)) \approx \frac{\gamma\Delta e_y}{\beta\Delta e_y} \tag{5.54}$$

in which γ and β are functions of the azimuth measurements and chief sidereal angle at each measurement time. The in-plane GEO elements cannot be determined explicitly given four in-plane linearized measurements, showing that the system is not observable.

A numerical simulation is performed to confirm this result. The initial conditions shown in Table 5.1 are propagated for 1 day and measurements are assumed to be collected every minute. The *a priori* covariance is again set to 5×10^{-10} for each relative GEO element. After one day, the rank of the accumulated measurement sensitivity matrix is 6; however, due to limited precision the rank of the matrix may be computed to be 6 but the matrix may be numerically ill-conditioned. The estimated uncertainty profile shown in Fig. 5.3 shows that the estimator is unable to extract information regarding the $\Delta\lambda$ and ΔQ_2 relative GEO elements from the angular measurements.

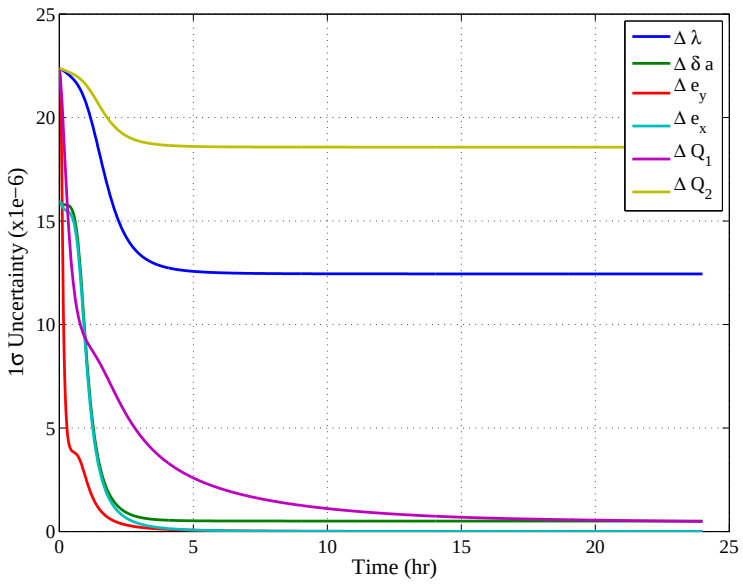

Figure 5.3: Relative GEO Element 1σ Estimated Uncertainty - Linearized Measurement Model

5.7 Conclusions

This analysis demonstrated that the relative GEO elements are fully observable given a nonlinear model of the space-based angular measurements and a linearized, unperturbed dynamic model that is analogous to Hill's model of relative motion. The use of spherical relative coordinates eliminates the observability issue that exists given a rectilinear representation of the relative dynamics. The relative GEO elements are fully observable given that there exists some time-varying relative motion and that the chief spacecraft sidereal angles at the times of observation at not spaced by integer multiples of 180 degrees. Also, out-of-plane motion is required to produce observability when the two spacecraft are in a circular leader-follower configuration. A numerical simulation showed that the relative GEO elements are observable when the spherical coordinates are used, and further confirms that linearization of the spherical coordinates removes this observability.

Chapter 6

Prediction of Along-Track Separation Uncertainty

6.1 Introduction

Relative state estimation is an orbit estimation concept that has been studied for several decades, and the achievable estimation accuracy for relative states of close-proximity geosynchronous objects given ground-based data has been investigated by several authors.[33; 45; 46; 48; 79; 82] High-accuracy WFOV space-based optical sensors are capable of simultaneously tracking multiple geosynchronous objects. Several estimation techniques have been presented which exploit the commonalities between close-proximity geosynchronous object dynamics and reduce measurement errors.[45; 46; 48; 79] Chapter 5 presented the observability challenges of angles-only relative state estimation.

Kawase [48] showed analytically that the relative orbit elements are observable given ground-based differential angle measurements, and he developed a simplified model of the expected covariance after 1 day of tracking. The expected covariance is computed as a function of the number of observations processed, the measurement noise, and the distance from the ground station to the chief satellite. A first-order linearized dynamic model is used, decoupling the out-of-plane and in-plane motion, and greatly simplifying the accumulated Gramian. Kawase [46] also developed a coupled absolute state Kalman filter to estimate the states of two simultaneously-tracked objects. The states were coupled through positive correlation of the objects' measurement errors. Simulation studies which processed 1 week of continuous radio-interferometric measurements with a coupled Kalman filter showed approximately 50 meters of estimate error. This technique was compared

to a relative estimation strategy in which differential observations were processed to estimate the state of an object relative to a reference orbit. These simulation results also showed that 50 meter estimate accuracy is possible if measurement biases are estimated in addition to the position and velocity states.

Additional theoretical and experimental research on relative state estimation has been published by Chris Sabol and Keric Hill, et. al.[79; 33] Sabol, et. al. introduced the Cluster Orbits with Perturbations of Keplerian Elements (COWPOKE) Equations, an approximated model of the relative motion of close-proximity objects.[79] Simulation results showed that the COWPOKE equations model the relative motion very well (on the order of the 50 meters seen in Kawase's theoretical developments). This relative motion model was also been investigated via experimental optical measurements of clustered geosynchronous objects. Hill, et. al. [33] processed experimental optical data spanning a period of 1 week with a relative state batch estimator. The solution was then propagated 1 day beyond the fit period, demonstrating prediction error on the order of 10 kilometers after the 1 day propagation.

Similar experimental studies using interferometric differential angle measurements were conducted by Kawase [45]. Two close-proximity geosynchronous satellites were tracked for 3 days, at observation sampling intervals of roughly 30 minutes. A sequential filter was able to recover the relative spacecraft positions to a few hundred meters. While the simulated estimation accuracy of 50 meters is promising, as of yet, experimental results at this level of accuracy have not been reported. Additionally, the above-mentioned orbit estimation results required angular metric data spanning a period of approximately 1 week, which for many applications is an unrealistically abundant number of observations.

The close of the 20th century saw the advent of passive space-based angles-only tracking, but satellite-to-satellite tracking via range and range-rate data is hardly a new concept. The TDRS and GPS satellites have been used for ranging of lower-altitude satellites for several decades.[5; 71] The possibility of geosynchronous satellite tracking via GPS positioning was proposed by Jorgensen [35] and subsequently investigated by numerous authors as a viable positioning tool.[10; 17; 115]

However, such ranging techniques are only applicable if the tracked object is outfitted with a GPS receiver or TDRS communications hardware, meaning that ranging cannot be used for passive tracking of general objects.

Space-based optical tracking of geosynchronous objects is currently performed by the Space-Based Visible (SBV) optical sensor package onboard the Midcourse Space Experiment satellite.[31] Launched in April 1996, this satellite is in a near sun-synchronous orbit at 898 kilometer altitude.[88] The WFOV (1.4 degree by 1.4 degree) visible sensor has access to the entire geosynchronous orbit regime and frequently detects multiple objects simultaneously. The SBV sensor has been proven to collect optical observations with 4 arcseconds metric accuracy.[108]

Canada's Department of National Defense has also developed a space-based space surveillance satellite, Sapphire, which will be launched in July 2011 and is planned to be fully operational by late 2011.[58] Sapphire will be in a low-altitude ($\approx$ 750 kilometers) sun-synchronous orbit and is outfitted with an electro-optical visible sensor capable of imaging objects at altitudes up to 40,000 kilometers. It is currently the intention of both the Canadian Department of National Defense and the United States Department of Defense that Sapphire will eventually serve as a contributing sensor to the US Space Surveillance Network. Initial experimental testing of the sensor's angular measurement accuracy indicated that the measurement noise standard deviation is approximately 3 arcseconds, with biases on the order of tenths of an arcsecond.[87]

Close-proximity optical tracking of geosynchronous objects, or geosynchronous-to-geosynchronous (GEO-to-GEO) tracking, is an attractive capability as is not impeded by the weather limitations of ground-based optical sensors. The majority of the literature and experimental efforts in the area of space-based space surveillance involve onboard sensors tracking objects outside of the sensor's orbital regime (such as LEO-to-GEO). However, the GEO-to-GEO tracking scenario has been studied by a few authors, including Vallado, Chen and Kawase [18; 43; 56; 104; 106]. Vallado [104] has performed extensive simulation studies of space-based angles-only tracking of geosynchronous satellites, in which he studied the effect of the chief (tracker) satellite orbital regime (low-altitude orbit, GPS orbit, and geosynchronous orbit) on the estimation accuracy of the deputy satellite's

classical orbit elements. Measurements were generated at sampling times of 30 seconds to 2 minutes over a span of twenty minutes, cycled every 360 minutes. The measurements were processed by the Orbit Determination ToolKit (ODTK) Gooding (angles-only) Initial Orbit Determination (IOD) filter. The results showed that the best orbit accuracy corresponds to the maximum relative motion between the chief and deputy satellites, and that observability issues arose for the cases where the relative motion was limited.

The concept of combining ground-based and GEO-to-GEO space-based tracking measurements was also expanded upon by Vallado, et. al. [56]. A proof-of-concept study was performed on hosting optical sensors onboard commercially-owned and operated geosynchronous satellites. Vallado presented the results of an analysis in which ODTK's sequential filter was used to process simulated ground-based and GEO-to-GEO space-based angles-only measurements. The results demonstrated that the estimated uncertainty produced by fitting to an ample amount of space-based data is not significantly affected by the inclusion of sparse ground-based data. However, the inclusion of sparse ground-based data may aide in filter convergence for cases in which the space-based observability is limited.

Chen [18] proposed employing two simultaneously-operated tracking satellites as a solution for the case of limited space-based observability. An EKF was developed to recover the relative position and velocity of the target given noisy measurements. Given only one tracker spacecraft, the target state estimated 3σ uncertainty was on the order of 1 kilometer in each position component and 1 meter per second in each velocity component, while adding a second tracker reduced the 3σ uncertainty to the order of 100 meters and 0.5 meters per second in each position and velocity component. This covariance improvement was not quite as significant as when a single tracker provided range measurements in addition to the angles-only measurements. For this case, the 3σ uncertainty was on the order of a few meters in position and 10 millimeters per second in velocity. Note that it was assumed that the second tracker orbit was known to the order of a few meters in position and a few centimeters per second in velocity.

Rather than simulate specific case studies, Kawase [43] developed analytic expressions for

the expected covariance for GEO-to-GEO tracking via range measurements, and range and angular measurements. Using a linearized dynamic model defined in non-singular orbital elements, Kawase developed an analytic prediction of the estimated covariance of a subset of the deputy spacecraft's elements given noisy range and angular measurements collected over 1 day. This simplified analytic model was derived assuming no *a priori* covariance information was provided, that a large number of measurements were collected, and that the spacecraft were in Keplerian orbits. Also, it was assumed that range measurements were used to solve for the elements representing longitude, semi-major axis, and the eccentricity vector components, and azimuth measurements were used to solved for the inclination vector components (note that Kawase's azimuthal measurement was defined as the ratio of the out-of-plane displacement to the in-track displacement, where the displacement was measured relative to the chief satellite's LVLH frame). The linearized dynamic model was then used to map the orbit element uncertainty into three error indices: intersatellite separation error, relative drift rate error, and mean periodical position error. Given Gaussian measurement noise on the order of 10 meters in range and 1 degree in azimuth, a longitudinal separation of 10 kilometers, and measurements collected every hour for 1 day, the accuracy was computed to be 6 meters, 11 meters, and 51 meters in the intersatellite separation, relative drift rate, and periodical position error indices, respectively.

Typically, covariance prediction, or propagation, is performed via linearized mapping that has been approximated about some nominal trajectory.[94] In 1971, Alspach and Sorenson [91; 9] introduced the Gaussian Mixture Modeling (GMM) technique for nonlinear covariance propagation. GMM is a method in which the non-Gaussian state error distribution is represented as a summation of individual Gaussian probability density function. Park and Scheeres [69; 70] implemented a high-order state transition tensor approximation of nonlinear system dynamics for uncertainty mapping. Invoking the constraints defined by the Fokker–Planck differential equation increased the accuracy of the uncertainty propagation compared to more traditional first-order covariance mapping, but at the cost of increased computational complexity. A novel approach for more accurate, yet not computationally intensive, covariance propagation was introduced by DeMars [24].

DeMars' Splitting Gaussian Mixture UKF essentially uses a metric of the nonlinearity of the system to determine when to implement the GMM covariance propagation rather than a standard UKF Gaussian sigma-point propagation. This technique has been proven to more accurately propagate the covariance of nonlinear dynamic systems compared to the linearized mapping methods.

This dissertation research (as well as Kawase's work) takes advantage of the simplicity of geosynchronous motion as represented by the GEO elements (non-singular orbit elements) to simplify the covariance prediction. As shown in Chapter 3, the near-linear behavior of the GEO elements means that linearly propagating the covariance via the first-order state transition matrix does not sacrifice accuracy. As such, this work leverages the simplicity of the linear covariance propagation of the batch estimation algorithm.

The work presented in this chapter develops the analytic uncertainty profile of the along-track separation given angles-only observations and *a priori* covariance information. The focus is placed on the along-track separation as this relative distance is the most difficult relative state to recover accurately from angular measurements. This work uses the linearized two-body relative motion model introduced in Chapter 5 in order to characterize the relative orbit uncertainty as a function of the *a priori* covariance, tracking duration, measurement noise and chief spacecraft mean motion. A first-order approximated solution to the Riccati differential equation is developed as an analytic covariance prediction tool which can be used to determine the amount of tracking required to reduce the estimated covariance to a desired level. The analytic uncertainty is presented as the uncertainty in the along-track separation as well as the overall uncertainty in the total distance between the chief and deputy spacecraft.

6.2 Full Relative GEO State Estimation

As shown in Chapter 5, the full set of relative GEO elements can be estimated given space-based angles-only measurements. However, certain elements are recovered at a faster rate than others, and this information can be used to simplify the development of the analytic covariance profile and accelerate the batch estimator converging to a more accurate solution. To demonstrate

this concept, a simulation is performed in which only the relative semi-major axis GEO element is zero. Requiring the semi-major axis difference to be zero ensures bounded motion of the deputy relative to the chief. The initial conditions of the chief spacecraft and the relative elements are given in Table 6.1. Note that the states are defined in the classical orbit elements in addition to the GEO elements, to provide physical intuition to the reader. The batch estimator is implemented in the GEO element space. Also, the total along-track separation is approximately 10 kilometers and is distributed evenly amongst the mean anomaly, right ascension, and argument of perigee.

Table 6.1: Tracker and Differential Epoch Orbit Elements (Epoch: Jan 1, 2010 0:03:12 UTC)

	a (km)	e	i (deg)	Ω (deg)	ω (deg)	M (deg)
Tracker	42164.812	2.47 x 10^{-4}	0.07	62.14	192.02	99.74
Differential	0	1.0 x 10^{-5}	0.01	4.530 x 10^{-3}	4.530 x 10^{-3}	4.530 x 10^{-3}
	λ (rad)	$\delta\bar{a}$	e_x	e_y	Q_1	Q_2
Tracker	4.408494	1.5 x 10^{-5}	-2.38 x 10^{-4}	-6.8 x 10^{-5}	5.40 x 10^{-4}	2.86 x 10^{-4}
Differential	2.57 x 10^{-4}	0	-1.0 x 10^{-5}	-3 x 10^{-6}	7.7 x 10^{-5}	4.1 x 10^{-5}

The GEO element batch estimator is initialized with a unitless *a priori* covariance of 5×10^{-10} in each component and it is assumed that the *a priori* covariance is not correlated between states. Space-based azimuth and elevation measurements are generated once per minute for 1 day, and the measurements are degraded with Gaussian noise of zero mean and standard deviation of 4 arcseconds. The batch estimator processes the set of measurements, and the estimated uncertainty of each GEO element as a function of time is shown in Fig. 6.1. The uncertainties in the $\Delta\delta\bar{a}$, Δe_y and Δe_x states decrease to less than 3% of their *a priori* values within roughly 1 hour of tracking. The remaining relative elements, $\Delta\lambda$, ΔQ_1 and ΔQ_2, require a significantly longer tracking arc.

The uncertainty profile suggests that once the batch estimator has converged on a steady-state solution for the eccentricity and semi-major axis terms, they can be considered to be known parameters. The GEO estimator can then be altered to recover a reduced element set consisting only of the longitude and inclination terms. This allows for the simplification of the GEO element

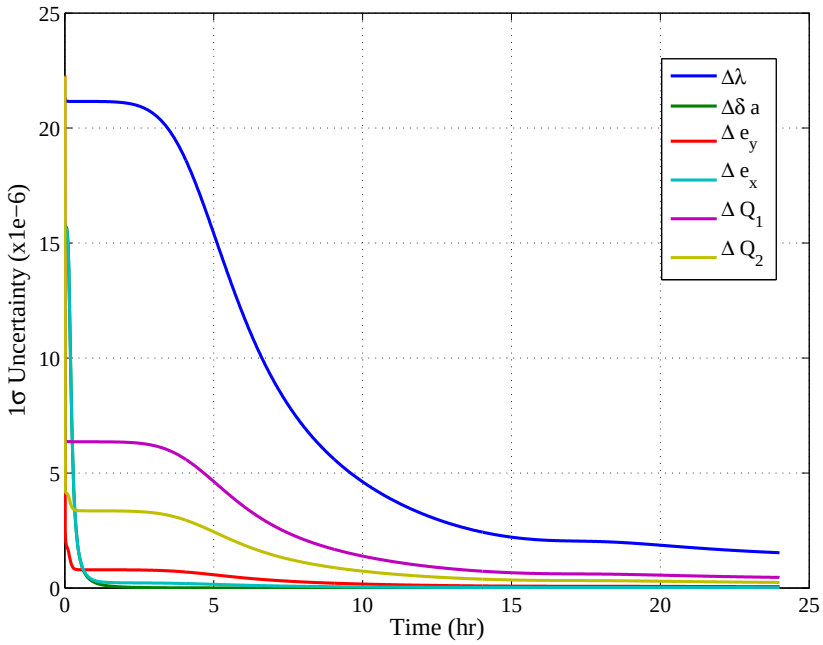

Figure 6.1: Relative GEO Element 1σ Estimated Uncertainty

batch estimator developed for the case of general relative motion, and leads to the characterization of the limiting uncertainty.

6.3 Simplification of Measurement Equations for Circular Bounded Relative Motion

The relative motion model presented in Eqs. 5.27 through 5.32 was developed by linearizing the nonlinear motion about the chief spacecraft's GEO elements. Now this linearized spherical coordinate dynamic model is further simplified to examine bounded Keplerian relative motion for two geosynchronous objects. For bounded relative motion in which both objects are in circular orbits, only the $\Delta\lambda$, ΔQ_1 and ΔQ_2 terms are non-zero. Eqs. 5.27 through 5.32 are reduced to:

$$x(t) \approx 0 \tag{6.1}$$

$$y(t) \approx r\Delta\lambda \tag{6.2}$$

$$z(t) \approx -2r\cos s(t)\Delta Q_1 + 2r\sin s(t)\Delta Q_2 \tag{6.3}$$

$$\dot{x}(t) \approx 0 \tag{6.4}$$

$$\dot{y}(t) \approx 0 \tag{6.5}$$

$$\dot{z}(t) \approx 2rn\sin s(t)\Delta Q_1 + 2rn\cos s(t)\Delta Q_2 \tag{6.6}$$

Recall that the longitude and inclination vector components are highly correlated through the right ascension of the ascending node. This coupling introduces difficulties in the development of an analytic covariance prediction, and as such it is desirable to represent the out-of-plane motion in terms of the relative inclination only. Lane [52] derives the linearized equation of motion for the spherical out-of-plane position in terms of the relative classical orbit elements as:

$$z(t) \approx r\sin\theta(t)\Delta i + r\sin i\cos\theta(t)\Delta\Omega \tag{6.7}$$

Eq. 6.7 is a first-order linearization about the chief classical orbit elements. Note that the inclination of geosynchronous objects is near-zero, and as such $\sin i\Delta\Omega$ will be second order. For

near-zero inclination orbits the out-of-plane motion is therefore dominated by the Δi contribution, so the z position can be further approximated as:

$$z(t) \approx r \sin\theta(t) \Delta i \tag{6.8}$$

The rectilinear relative position vector components can be determined by substituting Eqs. 6.1, 6.2 and 6.8 into Eqs. 5.34 through 5.36. The rectilinear position coordinates are given by:

$$x' = r \cos\left(\sin\theta \Delta i\right) \cos\Delta\lambda - r \tag{6.9}$$

$$y' = r \cos\left(\sin\theta \Delta i\right) \sin\Delta\lambda \tag{6.10}$$

$$z' = r \sin\left(\sin\theta \Delta i\right) \tag{6.11}$$

The space-based azimuth and elevation measurements, defined in terms of the rectilinear coordinates in Eq. 5.33, can now be simplified to functions of $\Delta\lambda$ and Δi only.

$$\tan\left(az\right) = \frac{\cos\left(\sin\theta \Delta i\right) \sin\Delta\lambda}{\cos\left(\sin\theta \Delta i\right) \cos\Delta\lambda - 1} \tag{6.12}$$

$$\tan\left(el\right) = \frac{\sin\left(\sin\theta \Delta i\right)}{\left[\cos^2\left(\sin\theta \Delta i\right) - 2\cos\left(\sin\theta \Delta i\right) \cos\Delta\lambda + 1\right]^{1/2}} \tag{6.13}$$

6.4 Analytic Solution to the Riccati Differential Equation

In weighted batch estimation applications the covariance is determined by inverting the accumulated Gramian matrix, $H^T W H$. The measurement sensitivity matrix, H, was developed in terms of the GEO elements in Eqs. 5.39 through 5.50. The accumulated Gramian effectively reveals how the addition of discrete measurements decreases the estimated state uncertainty. If observations can be made at will, the interval between measurements can be decreased to a point where the observations are collected near-continuously (on the order of one second). Given a continuous filter and Gaussian measurement noise, the covariance time derivative is governed by the matrix Riccati equation[28]:

$$\dot{P} = FP + PF^T + GQG^T - PH^T S^{-1} HP^T \tag{6.14}$$

in which F is the partial derivative of the dynamic model with respect to the states, Q is the dynamic process noise, and S is the measurement noise spectral density matrix. S is defined as:

$$S = R\Delta t \tag{6.15}$$

in which Δt is the discrete measurement sampling time. Given uncorrelated measurement noise, the spectral density matrix can be expressed in terms of the measurement noise standard deviation as:

$$S = \begin{bmatrix} \sigma^2(az) & 0 \\ 0 & \sigma^2(el) \end{bmatrix} \Delta t = \begin{bmatrix} S(az) & 0 \\ 0 & S(el) \end{bmatrix} \tag{6.16}$$

The batch estimator formulated for this work does not include dynamic process noise. Therefore the Riccati equation (Eq. 6.14) can be simplified by setting $Q = 0$. Further, for Keplerian circular bounded relative motion the relative longitude and inclination are constant, and the F term is therefore zero for all time. The Riccati equation is now simplified to:

$$\dot{P} = -PH^T S^{-1} H P^T \tag{6.17}$$

Integration of Eq. 6.17 produces a profile of covariance behavior as a function of tracking time. The covariance matrix is defined as:

$$P = \begin{bmatrix} P_{\Delta\lambda} & P_{\Delta\lambda\Delta i} \\ P_{\Delta\lambda\Delta i} & P_{\Delta i} \end{bmatrix} \tag{6.18}$$

in which $P_{\Delta\lambda}$ is the differential longitude variance, $P_{\Delta i}$ is the differential inclination variance, and $P_{\Delta\lambda\Delta i}$ is the covariance between the two states.

The measurement sensitivity matrix, H is defined as:

$$H = \begin{bmatrix} \frac{\partial az}{\partial \Delta\lambda} & \frac{\partial az}{\partial \Delta i} \\ \frac{\partial el}{\partial \Delta\lambda} & \frac{\partial el}{\partial \Delta i} \end{bmatrix} \tag{6.19}$$

The limiting factor in accurate knowledge of the relative state of a deputy spacecraft is the along-track separation, which has been shown to require a longer tracking arc for accurate estimation.[112] The Riccati differential equation is used to analyze the evolution of the along-track

separation, or $\Delta\lambda$, uncertainty. Substitution of Eqs. 6.16, 6.18 and 6.19 into Eq. 6.17 produces the following variance and covariance time derivatives for the $\Delta\lambda$ terms:

$$\dot{P}_{\Delta\lambda} = -S(az)^{-1}\left(\left[\frac{\partial az}{\partial \Delta\lambda}\right]^2 P^2_{\Delta\lambda} + 2\left[\frac{\partial az}{\partial \Delta\lambda}\right]\left[\frac{\partial az}{\partial \Delta i}\right] P_{\Delta\lambda}P_{\Delta\lambda\Delta i} + \left[\frac{\partial az}{\partial \Delta i}\right]^2 P^2_{\Delta\lambda\Delta i}\right) - S(el)^{-1}\left(\left[\frac{\partial el}{\partial \Delta\lambda}\right]^2 P^2_{\Delta\lambda} + 2\left[\frac{\partial el}{\partial \Delta\lambda}\right]\left[\frac{\partial el}{\partial \Delta i}\right] P_{\Delta\lambda}P_{\Delta\lambda\Delta i} + \left[\frac{\partial el}{\partial \Delta i}\right]^2 P^2_{\Delta\lambda\Delta i}\right) \quad (6.20)$$

$$\dot{P}_{\Delta\lambda\Delta i} = -S(az)^{-1}\left(\left[\frac{\partial az}{\partial \Delta\lambda}\right]^2 P_{\Delta\lambda}P_{\Delta\lambda\Delta i} + \left[\frac{\partial az}{\partial \Delta\lambda}\right]\left[\frac{\partial az}{\partial \Delta i}\right] P^2_{\Delta\lambda\Delta i}\right) - S(az)^{-1}\left(\left[\frac{\partial az}{\partial \Delta\lambda}\right]\left[\frac{\partial az}{\partial \Delta i}\right] P_{\Delta\lambda}P_{\Delta i} + \left[\frac{\partial az}{\partial \Delta i}\right]^2 P_{\Delta\lambda\Delta i}P_{\Delta i}\right) - S(el)^{-1}\left(\left[\frac{\partial el}{\partial \Delta\lambda}\right]^2 P_{\Delta\lambda}P_{\Delta\lambda\Delta i} + \left[\frac{\partial el}{\partial \Delta\lambda}\right]\left[\frac{\partial el}{\partial \Delta i}\right] P^2_{\Delta\lambda\Delta i} - S(el)^{-1}\left(\left[\frac{\partial el}{\partial \Delta\lambda}\right]\left[\frac{\partial el}{\partial \Delta i}\right] P_{\Delta\lambda}P_{\Delta i} + \left[\frac{\partial el}{\partial \Delta i}\right]^2 P_{\Delta\lambda\Delta i}P_{\Delta i}\right) \quad (6.21)$$

The measurement partial derivatives with respect to $\Delta\lambda$ are given by:

$$\frac{\partial az}{\partial \Delta\lambda} = \frac{\cos^2(\sin\theta\Delta i) - \cos(\sin\theta\Delta i)\cos\Delta\lambda}{\cos^2(\sin\theta\Delta i) - 2\cos(\sin\theta\Delta i)\cos\Delta\lambda + 1} \quad (6.22)$$

$$\frac{\partial el}{\partial \Delta\lambda} = \frac{-\sin(\sin\theta\Delta i)\cos(\sin\theta\Delta i)\sin\Delta\lambda}{[2 - 2\cos(\sin\theta\Delta i)\cos\Delta\lambda]\,[\cos^2(\sin\theta\Delta i) - 2\cos(\sin\theta\Delta i)\cos\Delta\lambda + 1]^{1/2}} \quad (6.23)$$

Likewise, the measurement partial derivatives with respect to Δi are:

$$\frac{\partial az}{\partial \Delta i} = \frac{2\sin\Delta\lambda\sin\theta\sin(\sin\theta\Delta i)}{3 - 4\cos\Delta\lambda\cos(\sin\theta\Delta i) + \cos(2\sin\theta\Delta i)} \quad (6.24)$$

$$\frac{\partial el}{\partial \Delta i} = \frac{\sin\theta\left(-4\cos(\sin\theta\Delta i) + \cos\Delta\lambda\,[3 + \cos(2\sin\theta\Delta i)]\right)}{4\,[\cos\Delta\lambda\cos(\sin\theta\Delta i) - 1]\,[1 - 2\cos\Delta\lambda\cos(\sin\theta\Delta i) + \cos^2(\sin\theta\Delta i)]^{1/2}} \quad (6.25)$$

Substitution of Eqs. 6.22 through 6.25 into Eqs. 6.20 and 6.21 produces the following differential equations:

$$\begin{aligned}
\dot{P}_{\Delta\lambda} = -S(az)^{-1}\Bigg(& \left[\frac{\cos^2(\sin\theta\Delta i) - \cos(\sin\theta\Delta i)\cos\Delta\lambda}{\cos^2(\sin\theta\Delta i) - 2\cos(\sin\theta\Delta i)\cos\Delta\lambda + 1}\right]^2 P_{\Delta\lambda}^2 \\
& + 2\left[\frac{\cos^2(\sin\theta\Delta i) - \cos(\sin\theta\Delta i)\cos\Delta\lambda}{\cos^2(\sin\theta\Delta i) - 2\cos(\sin\theta\Delta i)\cos\Delta\lambda + 1}\right]\times \\
& \left[\frac{2\sin\Delta\lambda\sin\theta\sin(\sin\theta\Delta i)}{3 - 4\cos\Delta\lambda\cos(\sin\theta\Delta i) + \cos(2\sin\theta\Delta i)}\right] P_{\Delta\lambda}P_{\Delta\lambda\Delta i} \\
& + \left[\frac{2\sin\Delta\lambda\sin\theta\sin(\sin\theta\Delta i)}{3 - 4\cos\Delta\lambda\cos(\sin\theta\Delta i) + \cos(2\sin\theta\Delta i)}\right]^2 P_{\Delta\lambda\Delta i}^2\Bigg) \\
& - S(el)^{-1}\Bigg(\left[\frac{-\sin(\sin\theta\Delta i)\cos(\sin\theta\Delta i)\sin\Delta\lambda}{[2 - 2\cos(\sin\theta\Delta i)\cos\Delta\lambda]\left[\cos^2(\sin\theta\Delta i) - 2\cos(\sin\theta\Delta i)\cos\Delta\lambda + 1\right]^{1/2}}\right]^2 \\
& \times P_{\Delta\lambda}^2 + 2\left[\frac{-\sin(\sin\theta\Delta i)\cos(\sin\theta\Delta i)\sin\Delta\lambda}{[2 - 2\cos(\sin\theta\Delta i)\cos\Delta\lambda]\left[\cos^2(\sin\theta\Delta i) - 2\cos(\sin\theta\Delta i)\cos\Delta\lambda + 1\right]^{1/2}}\right] \\
& \left[\frac{\sin\theta\Big(-4\cos(\sin\theta\Delta i) + \cos\Delta\lambda\left[3 + \cos(2\sin\theta\Delta i)\right]\Big)}{4\left[\cos\Delta\lambda\cos(\sin\theta\Delta i) - 1\right]\left[1 - 2\cos\Delta\lambda\cos(\sin\theta\Delta i) + \cos^2(\sin\theta\Delta i)\right]^{1/2}}\right] P_{\Delta\lambda}P_{\Delta\lambda\Delta i} \\
& + \left[\frac{\sin\theta\Big(-4\cos(\sin\theta\Delta i) + \cos\Delta\lambda\left[3 + \cos(2\sin\theta\Delta i)\right]\Big)}{4\left[\cos\Delta\lambda\cos(\sin\theta\Delta i) - 1\right]\left[1 - 2\cos\Delta\lambda\cos(\sin\theta\Delta i) + \cos^2(\sin\theta\Delta i)\right]^{1/2}}\right]^2 P_{\Delta\lambda\Delta i}^2\Bigg) \qquad (6.26)
\end{aligned}$$

$$\dot{P}_{\Delta\lambda\Delta i} = -S(az)^{-1}\Bigg(\left[\frac{\cos^2(\sin\theta\Delta i) - \cos(\sin\theta\Delta i)\cos\Delta\lambda}{\cos^2(\sin\theta\Delta i) - 2\cos(\sin\theta\Delta i)\cos\Delta\lambda + 1}\right]^2 P_{\Delta\lambda}P_{\Delta\lambda\Delta i} + \left[\frac{\cos^2(\sin\theta\Delta i) - \cos(\sin\theta\Delta i)\cos\Delta\lambda}{\cos^2(\sin\theta\Delta i) - 2\cos(\sin\theta\Delta i)\cos\Delta\lambda + 1}\right] \times \left[\frac{2\sin\Delta\lambda\sin\theta\sin(\sin\theta\Delta i)}{3 - 4\cos\Delta\lambda\cos(\sin\theta\Delta i) + \cos(2\sin\theta\Delta i)}\right]\left[P^2_{\Delta\lambda\Delta i} + P_{\Delta\lambda}P_{\Delta i}\right] + \left[\frac{2\sin\Delta\lambda\sin\theta\sin(\sin\theta\Delta i)}{3 - 4\cos\Delta\lambda\cos(\sin\theta\Delta i) + \cos(2\sin\theta\Delta i)}\right]^2 P_{\Delta\lambda\Delta i}P_{\Delta i}\Bigg)$$

$$- S(el)^{-1}\Bigg(\left[\frac{-\sin(\sin\theta\Delta i)\cos(\sin\theta\Delta i)\sin\Delta\lambda}{[2 - 2\cos(\sin\theta\Delta i)\cos\Delta\lambda]\left[\cos^2(\sin\theta\Delta i) - 2\cos(\sin\theta\Delta i)\cos\Delta\lambda + 1\right]^{1/2}}\right]^2 \times P_{\Delta\lambda}P_{\Delta\lambda\Delta i} + \left[\frac{-\sin(\sin\theta\Delta i)\cos(\sin\theta\Delta i)\sin\Delta\lambda}{[2 - 2\cos(\sin\theta\Delta i)\cos\Delta\lambda]\left[\cos^2(\sin\theta\Delta i) - 2\cos(\sin\theta\Delta i)\cos\Delta\lambda + 1\right]^{1/2}}\right] \left[\frac{\sin\theta\Big(-4\cos(\sin\theta\Delta i) + \cos\Delta\lambda\left[3 + \cos(2\sin\theta\Delta i)\right]\Big)}{4\left[\cos\Delta\lambda\cos(\sin\theta\Delta i) - 1\right]\left[1 - 2\cos\Delta\lambda\cos(\sin\theta\Delta i) + \cos^2(\sin\theta\Delta i)\right]^{1/2}}\right] \times \left[P^2_{\Delta\lambda\Delta i} + P_{\Delta\lambda}P_{\Delta i}\right] + \left[\frac{\sin\theta\Big(-4\cos(\sin\theta\Delta i) + \cos\Delta\lambda\left[3 + \cos(2\sin\theta\Delta i)\right]\Big)}{4\left[\cos\Delta\lambda\cos(\sin\theta\Delta i) - 1\right]\left[1 - 2\cos\Delta\lambda\cos(\sin\theta\Delta i) + \cos^2(\sin\theta\Delta i)\right]^{1/2}}\right]^2 P_{\Delta\lambda\Delta i}P_{\Delta i}\Bigg) \quad (6.27)$$

6.5 Approximation of Riccati Differential Equation for Co-Planar Orbits

Closed-form analytic solutions to the differential equation given by Eq. 6.26 and 6.27 do not exist. In particular, the $\sin(\sin\theta\Delta i)$ and $\cos(\sin\theta\Delta i)$ terms cannot be analytically integrated over θ. In order to approximate a closed-form solution, the measurement partial derivatives are linearized about $\sin\theta\Delta i = 0$. Expanding Eqs. 6.22 through 6.25 in Taylor Series and retaining first-order terms in the approximated measurement sensitivity partial derivatives yields:

$$\frac{\partial az}{\partial\Delta\lambda} \approx \frac{1}{2} \quad (6.28)$$

$$\frac{\partial el}{\partial\Delta\lambda} \approx -\frac{\sin\Delta\lambda\sin\theta\Delta i}{2\sqrt{2}(1 - \cos\Delta\lambda)^{3/2}} \quad (6.29)$$

$$\frac{\partial az}{\partial\Delta i} \approx \frac{\sin\Delta\lambda\sin^2\theta\Delta i}{2 - 2\cos\Delta\lambda} \quad (6.30)$$

$$\frac{\partial el}{\partial \Delta i} \approx \frac{\sin\theta}{(2-2\cos\Delta\lambda)^{1/2}} \tag{6.31}$$

Eqs. 6.28 through 6.31 are substituted into Eqs. 6.20 and 6.21. Again retaining first-order accuracy in $\sin\theta\Delta i$, the time derivative of the $\Delta\lambda$ variance is expressed as:

$$\dot{P}_{\Delta\lambda} \approx -S(az)^{-1}\left(\frac{1}{4}P_{\Delta\lambda}^2 + \frac{\sin\Delta\lambda\sin^2\theta\Delta i}{2-2\cos\Delta\lambda}P_{\Delta\lambda}P_{\Delta\lambda\Delta i}\right) - S(el)^{-1}\left(-\frac{\sin\Delta\lambda\sin^2\theta\Delta i}{2(1-\cos\Delta\lambda)^2}P_{\Delta\lambda}P_{\Delta\lambda\Delta i} + \frac{\sin^2\theta}{(2-2\cos\Delta\lambda)}P_{\Delta\lambda\Delta i}^2\right) \tag{6.32}$$

The $\Delta\lambda - \Delta i$ covariance time derivative is approximated as:

$$\dot{P}_{\Delta\lambda\Delta i} \approx -S(az)^{-1}\left(\frac{1}{4}P_{\Delta\lambda\Delta i}P_{\Delta\lambda} + \frac{\sin\Delta\lambda\sin^2\theta\Delta i}{4-4\cos\Delta\lambda}P_{\Delta\lambda\Delta i}^2 + \frac{\sin\Delta\lambda\sin^2\theta\Delta i}{4-4\cos\Delta\lambda}P_{\Delta\lambda}P_{\Delta i}\right) - S(el)^{-1}\left(-\frac{\sin\Delta\lambda\sin^2\theta\Delta i}{4(1-\cos\Delta\lambda)^2}P_{\Delta\lambda\Delta i}^2 - \frac{\sin\Delta\lambda\sin^2\theta\Delta i}{4(1-\cos\Delta\lambda)^2}P_{\Delta\lambda}P_{\Delta i} + \frac{\sin^2\theta}{2-2\cos\Delta\lambda}P_{\Delta\lambda\Delta i}P_{\Delta i}\right) \tag{6.33}$$

In order to reduce the approximated differential equations to a form that can be analytically integrated, the specific case of co-planar orbits is now analyzed. Evaluating at the linearization reference point ($\Delta i = 0$) reduces Eqs. 6.32 and 6.33 to:

$$\dot{P}_{\Delta\lambda} \approx -S(az)^{-2}\left(\frac{1}{4}P_{\Delta\lambda}^2\right) - S(el)^{-1}\left(\frac{\sin^2\theta}{(2-2\cos\Delta\lambda)}P_{\Delta\lambda\Delta i}^2\right) \tag{6.34}$$

$$\dot{P}_{\Delta\lambda\Delta i} \approx -S(az)^{-1}\left(\frac{1}{4}P_{\Delta\lambda\Delta i}P_{\Delta\lambda}\right) - S(el)^{-1}\left(\frac{\sin^2\theta}{2-2\cos\Delta\lambda}P_{\Delta\lambda\Delta i}P_{\Delta i}\right) \tag{6.35}$$

Note that the covariance differential equation is scaled by the *a priori* covariance. If the covariance between $\Delta\lambda$ and Δi is initialized as zero, as is generally the case in batch estimation applications, its time derivative is zero and the covariance will be zero for all time. This allows for further simplification of Eq. 6.34 to:

$$\dot{P}_{\Delta\lambda} \approx -S(az)^{-2}\left(\frac{1}{4}P_{\Delta\lambda}^2\right) \tag{6.36}$$

6.6 Closed-Form Analytic Uncertainty Model

The Riccati differential equation governing the along-track separation uncertainty has now been approximated into a form which can be integrated analytically. The integration variable is

now switched from dt to $d\theta$. Assuming that the chief spacecraft is in a circular two-body orbit, the relationship between dt and $d\theta$ is defined as:

$$dt = \frac{d\theta}{n} \tag{6.37}$$

Switching the integration variable and rearranging the derivative via the fundamental theorem of calculus allows Eq. 6.36 to be expressed as:

$$\frac{dP_{\Delta\lambda}}{-P_{\Delta\lambda}^2} \approx S(az)^{-1}\frac{1}{4n}d\theta \tag{6.38}$$

To produce a closed-form analytic solution for the $\Delta\lambda$ uncertainty, Eq. 6.38 is integrated over θ:

$$\int_{P_{\Delta\lambda,i}}^{P_{\Delta\lambda,f}} \frac{dP_{\Delta\lambda}}{-P_{\Delta\lambda}^2} \approx S(az)^{-1}\frac{1}{4n}\int_{\theta_i}^{\theta_f} d\theta \tag{6.39}$$

$$\frac{1}{P_{\Delta\lambda,f}} - \frac{1}{P_{\Delta\lambda,i}} \approx S(az)^{-1}\frac{1}{4n}\Big(\theta_f - \theta_i\Big) \tag{6.40}$$

Finally, Eq. 6.40 is rearranged to express the covariance at time t_f:

$$P_{\Delta\lambda,f} \approx \frac{4P_{\Delta\lambda,i}nS(az)}{4nS(az) + P_{\Delta\lambda,i}\Delta\theta} \tag{6.41}$$

in which $\Delta\theta = \theta_f - \theta_i$. The continuous filter uncertainty is thus an explicit function of the argument of latitude swept out by the chief spacecraft in the time passed since the epoch, the chief spacecraft's mean motion, the *a priori* uncertainty, and the measurement noise spectral density.

6.7 Numerical Verification

The first-order approximated model for predicting the $\Delta\lambda$ estimated uncertainty is a simple analytic expression useful for the planning of space-based angles-only tracking strategies. For instance, if the accuracy requirements stipulate that the relative longitude must be know to a specific covariance level, then Eq. 6.41 can be used to approximate the tracking arc necessary to meet this requirement. Next, the analytic variance profile shown in Eq. 6.41 is numerically verified using simulation studies. The linearization error is quantified for the $\Delta\lambda$ variance by comparing the analytic uncertainty to the batch estimated uncertainty as the Δi value is increased. Additionally,

a Monte Carlo analysis is used to analyze how well the first-order approximated variance profile represents the actual estimation error distribution.

6.7.1 Linearization Error

The effect of linearizing the uncertainty profile to first-order about $\sin\theta\Delta i = 0$ is characterized through a simulation study. A relative GEO element batch estimator recovers the $\Delta\lambda$, ΔQ_1 and ΔQ_2 terms. The chief spacecraft GEO elements at the epoch at shown in Table 6.2. The relative GEO elements, also shown in the table, are defined such that $\Delta\delta\bar{a} = \Delta e_y = \Delta e_x = 0$, and $\Delta\lambda =$ 10 kilometers. The batch estimator is run for values of differential inclination from 1×10^{-8} degrees to 1×10^{-2} degrees. (Table 6.2 displays the relative GEO elements for a differential inclination of 1×10^{-2} degrees.) Observations are processed once every second for 1 day, and the azimuth and elevation measurements are degraded by Gaussian noise with a standard deviation of 4 arcseconds. The estimated $\Delta\lambda$ and Δi covariance for each Δi scenario are compared to the analytic covariance model. This allows for the assessment of how the error introduced by linearizing about $\sin\theta\Delta i = 0$ impacts the accuracy of the analytic covariance model.

Table 6.2: Chief and Relative GEO Elements at Epoch (Jan 1, 2010 0:03:12 UTC)

	λ (rad)	$\delta\bar{a}$	e_x	e_y	Q_1	Q_2
Chief GEO Elements	4.40799	1.5 x 10^{-5}	0	0	1.66 x 10^{-4}	-8.8 x 10^{-5}
Relative GEO Elements	2.37 x 10^{-4}	0	0	0	7.7 x 10^{-5}	4.1 x 10^{-5}

6.7.1.1 $P_{\Delta\lambda}$ Linearization Error

Fig. 6.2 displays the relative longitude 3σ estimated uncertainty for each of the Δi scenarios, and the analytic uncertainty profile. The figure displays the results of cases for $\Delta i \geq 1 \times 10^{-3}$ degrees, as the estimated uncertainty does not noticeably deviate from the first-order approximation for $\Delta i < 1 \times 10^{-3}$ degrees. (To put the Δi value in context, a Δi of 1×10^{-2} degrees results in a maximum out-of-plane separation of approximately 7.5 kilometers.) The maximum lineariza-

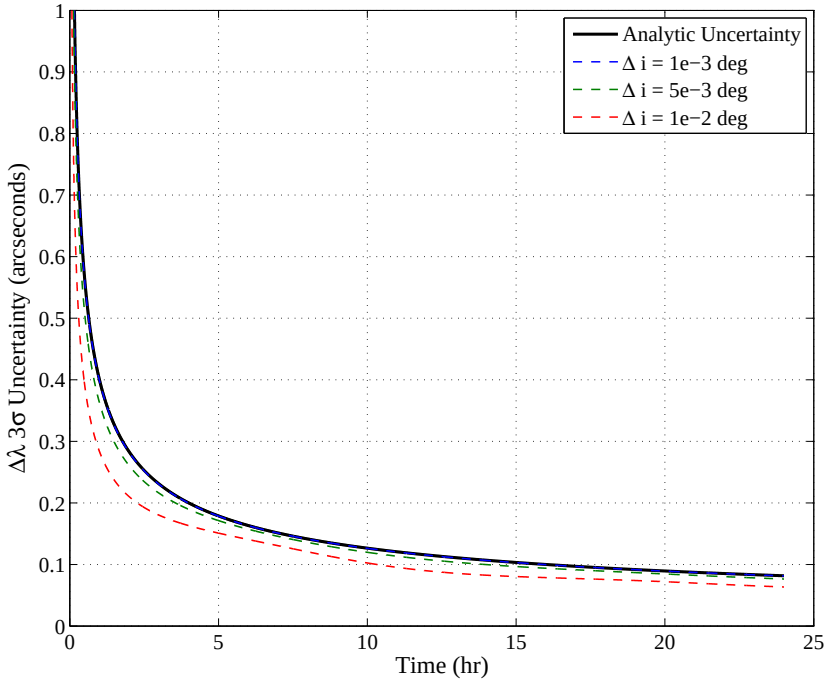

Figure 6.2: $\Delta\lambda$ 3σ Uncertainty for Varying Δi Values

tion error at this Δi value is on the order of 0.05 arcsecond, which is approximately 10 meters at the geosynchronous altitude. Note that after approximately 5 hours of tracking the discrepancy decreases to meter level.

Relative inclination values greater than 1×10^{-2} degrees produce an estimated variance profile that decreases significantly more quickly than the analytic variance. Recall that the analytic variance profile has been developed for close-proximity objects with a zero inclination difference; at a relative inclination of 1×10^{-1}degrees, the maximum out-of-plane separation is approximately 75 kilometers. Also, when the relative inclination is non-zero, the covariance ($P_{\Delta\lambda\Delta i}$) will become non-zero over time and contribute to the $\Delta\lambda$ uncertainty. The results indicate that the analytic uncertainty profile is representative of the estimated uncertainty within 10 meters given out-of-plane motion on the order of 10 kilometers. Note that the analytic covariance is more conservative than the actual batch estimator covariance for large Δi values.

6.7.2 Monte Carlo Analysis

It is ideal to validate the analytic covariance model by processing experimental optical measurements. Unfortunately, experimental space-based measurements are not available for this research. Instead, we turn to a Monte Carlo analysis to analyze the ability of the analytic covariance profile to realistically represent the estimation errors.

A scenario is set up in which the chief and deputy satellites are initialized as shown in Table 6.2. The deputy spacecraft is placed at a nominal differential longitude of 10 kilometers, and a differential inclination of 0.01 degrees. Measurements are generated once per second for 1 day and degraded with normally distributed noise at a standard deviation of 4 arcseconds. The relative GEO element batch estimator recovers $\Delta\lambda$, ΔQ_1, and ΔQ_2. The *a priori* state estimate is the true state plus some randomized error within the *a priori* uncertainty bounds, which are set at 5×10^{-10} for each state. The *a priori* cross-covariance is set to zero. The Monte Carlo analysis is set up to run the batch estimator for 100 cases in which the measurement noise and the *a priori* state are randomized. Note that the batch estimated uncertainty and analytic uncertainty model are not dependent on the randomized parameters.

Fig. 6.3 displays the estimated $\Delta\lambda$ error for each of the 100 cases, and the analytic and estimated 3σ uncertainty bounds. The errors are well bounded by the estimated batch uncertainty, indicating that the estimated covariance is a realistic representation of the actual estimation error. The errors are also well bounded by the analytic $\Delta\lambda$ uncertainty model, and as such it can be concluded that the first-order $\Delta\lambda$ variance model is an accurate representation of the estimation error for close-proximity relative motion.

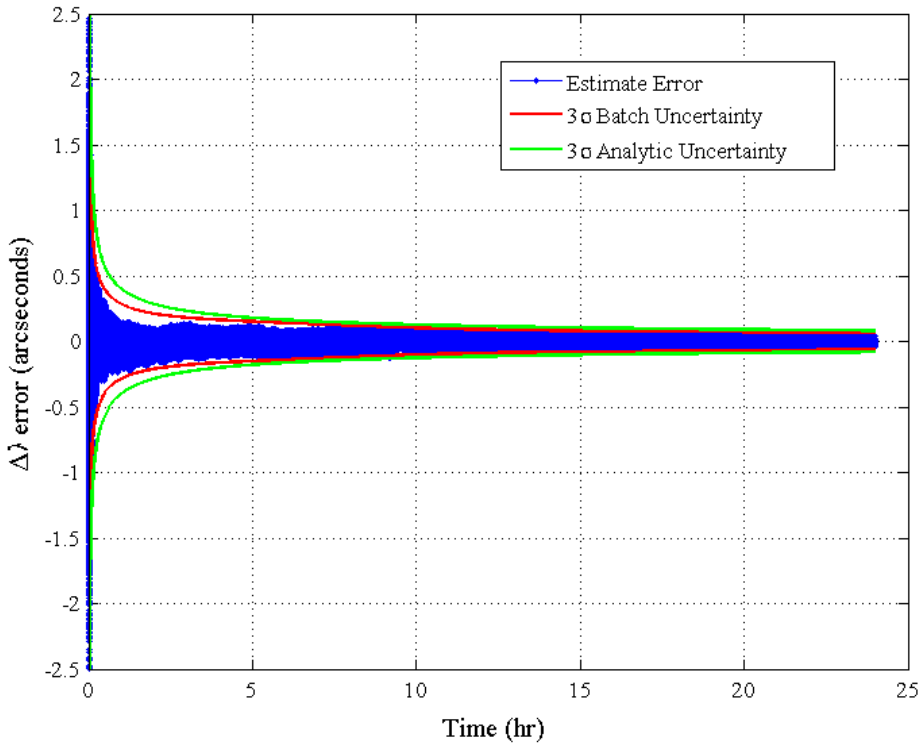

Figure 6.3: $\Delta\lambda$ 3σ Uncertainty Bounds and Estimation Error for $\Delta i = 0.01$ Degrees

6.8 Range Uncertainty Model

It may be of interest to characterize the uncertainty in the total distance between the chief and deputy spacecraft. For instance, close proximity operations may benefit from a direct metric of overall range uncertainty for spacecraft safety purposes. The analytic uncertainty in the intersatellite range magnitude is now derived from the $\Delta\lambda$ variance profile given by Eq. 6.41.

The intersatellite range, ρ, is defined as:

$$\rho = \sqrt{(x')^2 + (y')^2 + (z')^2} \tag{6.42}$$

For the simplified case of bounded circular relative motion in which only $\Delta\lambda$ and Δi are non-zero, the rectilinear relative position coordinates, x', y' and z', are expressed in terms of the relative GEO elements as shown in Eqs. 6.9 through 6.11. Substitution of Eqs. 6.9 through 6.11 into Eq. 6.42 produces:

$$\rho = r\sqrt{2(1 - \cos(\sin\theta\Delta i)\cos\Delta\lambda)} \tag{6.43}$$

With the range expressed in terms of the estimated states, the range uncertainty can now be derived by linearly transforming the $\Delta\lambda$ variance via the range sensitivity to the relative longitude. This transformation is given by:

$$P_\rho = \left[\frac{\partial\rho}{\partial\Delta\lambda}\right] P_{\Delta\lambda} \left[\frac{\partial\rho}{\partial\Delta\lambda}\right]^T \tag{6.44}$$

In order to linearly transform the relative longitude variance into the range space, the partial derivative of Eq. 6.43 with respect to the relative longitude must be computed. The partial derivative is:

$$\frac{\partial\rho}{\partial\Delta\lambda} = \frac{r^2}{\rho}\cos(\sin\theta\Delta i)\sin\Delta\lambda \tag{6.45}$$

Substituting Eq. 6.45 into Eq. 6.44 produces an expression of the approximated range variance:

$$P_\rho \approx \frac{4r^4 P_{\Delta\lambda,i} nS(az)\cos^2(\sin\theta\Delta i)\sin^2\Delta\lambda}{\rho^2(4nS(az) + P_{\Delta\lambda,i}\Delta\theta)} \tag{6.46}$$

The analytic expression shown in Eq. 6.46 is a linearized approximation of the range variance, and can be used as an orbit estimation planning tool to determine how much tracking is required to

estimate the range magnitude to a given accuracy level. Conversely, the expected range uncertainty can be approximated given a tracking duration and chief and deputy orbit paraemeters.

6.9 Numerical Verification of Range Uncertainty Profile

Similarly to the simulation verification of the relative longitude variance profile, the range variance model is now validated. The effect of linearization error on the range uncertainty model error is analyzed. Additionally, a Monte Carlo analysis is used to assess how well the analytic variance represents the actual estimation error.

6.9.1 Linearization Error

The impact linearizing the Riccati differential equation about $\sin\theta\Delta i = 0$ has on the analytic range variance is assessed by repeating the linearization error analysis performed for the $\Delta\lambda$ uncertainty profile. The chief spacecraft is initialized as shown in Table 6.2, and the relative longitude is set to 10 kilometers. A batch processor processes simulated noisy measurements for seven cases; each case has a different Δi value, varying from 1×10^{-8} degrees to 1×10^{-2} degrees. The analytic range uncertainty is computed as shown in Eq. 6.46. The batch estimated $\Delta\lambda$ variance is transformed into the range state space via:

$$P_\rho = \left[\frac{\partial\rho}{\partial\Delta\lambda}\right] \hat{P}_{\Delta\lambda} \left[\frac{\partial\rho}{\partial\Delta\lambda}\right]^T \tag{6.47}$$

in which $\hat{P}_{\Delta\lambda}$ is the estimated $\Delta\lambda$ covariance from the relative GEO element batch processor.

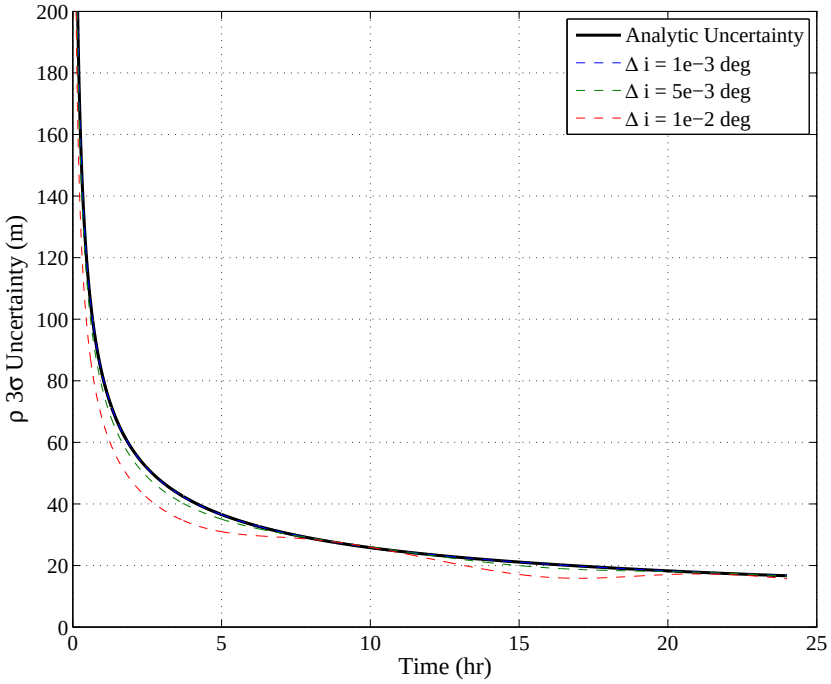

Figure 6.4: 3σ Range Uncertainty for Varying Δi Values

Fig. 6.4 presents the analytic 3σ range uncertainty with the estimated 3σ range uncertainty for each Δi value $\geq 1\times10^{-3}$ degrees. As was seen with the $\Delta\lambda$ uncertainty analysis, the linearization error does not significantly impact the analytic range uncertainty until Δi reaches a value of 1×10^{-2} degrees. At this point the second-order and covariance effects begin to present as small (sub-meter) oscillations in the estimated range uncertainty. The maximum discrepancy between the analytic and estimated 3σ uncertainty is on the order of 10 meters, indicating that at small Δi values (≤ 0.01 degrees) the linearization of the analytic range covariance profile does not introduce significant error. Also, like the $P_{\Delta\lambda}$ model, the range model is conservative compared to the estimated covariance.

The analytic range uncertainty shown in Fig. 6.4 indicates that 1 hour of continuous space-based passive tracking can decrease the range uncertainty from the kilometer-level down to the order of 10 meters, and 24 hours of produces meter-level range uncertainty. This is in line with the

results of Kawase's predicted covariance given range and angles measurements.[43]

6.9.2 Monte Carlo Analysis

Finally, a Monte Carlo analysis is performed to assess the range variance model's ability to accurately represent the estimation error distribution. The scenario used for the $P_{\Delta\lambda}$ Monte Carlo analysis is repeated. Fig. 6.5 shows the estimated range error, the estimated 3σ uncertainty bounds, and the 3σ analytic uncertainty bounds. Both the estimated and analytic covariances enclose the error distribution, demonstrating that the first-order prediction of the range uncertainty is representative of the true estimated state uncertainty.

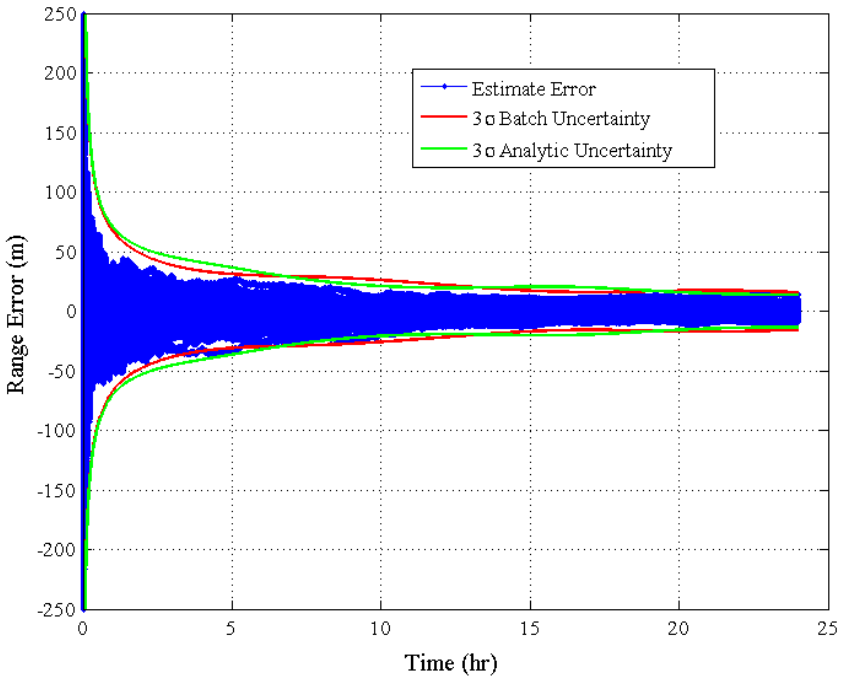

Figure 6.5: Range 3σ Uncertainty and Estimation Error for $\Delta i = 0.01$ Degrees

6.10 Conclusions

The outcome of the work presented in this chapter is a set of covariance prediction tools which are useful for space-based angles-only orbit estimation purposes. The focus of this research is the characterization of the uncertainty in the along-track separation, which is the limiting factor in angles-only relative orbit estimation. Linearized variance profiles for the along-track separation, $\Delta\lambda$, and the total distance between spacecraft, ρ, have been developed and numerically verified. Through Monte Carlo analysis, the analytic uncertainty has been shown to accurately capture the estimation error in the along-track separation and intersatellite range magnitude given small spacecraft separations. For a maximum out-of-plane displacement on the order of 10 kilometers, the $\Delta\lambda$ and range covariance models are shown to be accurate to the 10-meter level (3σ uncertainty). The results of this analysis indicate that given sufficient tracking (for approximately half of an orbit), the intersatellite range (or along-track separation) can be recovered to an uncertainty on the order of a few meters. The analytic uncertainty models developed in this work may be useful to approximate the amount of tracking that must be accomplished to meet an accuracy requirement, or to determine how well a spacecraft's orbit can be determined given a limited tracking scenario.

Chapter 7

Summary and Future Work

7.1 Summary

As the number of objects in and near the geosynchronous orbit regime continues to increase, so does the necessity for accurate knowledge of the positioning and dynamics of geosynchronous objects. In recent years, the capability to optically track space objects with ground-based sensors has been augmented with the addition of operational low-altitude space-based optical sensors. This work explored the accuracy of both ground-based and space-based geosynchronous orbit estimation, and specifically addressed the research goals outlined in Section 1.2. The principle findings of this work are now summarized in the context of the stated research goals.

- *High-accuracy dynamic modeling of geosynchronous motion utilizing a well-suited coordinate representation.*

  An investigation into the impact of coordinate selection on geosynchronous dynamic modeling and estimation led to the development of a GEO element set and a nonlinear GEO element dynamic model for general perturbed motion. It was shown that the GEO element perturbed dynamic model is as accurate as the more traditionally used inertial Cartesian coordinate dynamic models. Moreover, the GEO element model avoids potential singularities and numerical sensitivities for near-zero eccentricity and inclination orbits.

- *A strategy utilizing angles-only observations and an appropriate dynamic modeling coordinate set.*

  Well-defined and numerically stable for geosynchronous conditions, the GEO elements are an effective choice for linear orbit estimation and covariance propagation as their naturally-perturbed variations behave near linearly. Both simulated and experimental optical measurements of a TDRS satellite were processed to validate the GEO element batch estimator. Comparison with an inertial Cartesian batch estimator demonstrated that given angles-only measurements, GEO element batch estimation does not suffer as much accuracy loss through the measurement linearization as does estimation in the Cartesian state space. This results in a better estimate of the in-track position and radial velocity of the geosynchronous object.

- *Characterization of the achievable geosynchronous orbit accuracy given ground-based angles-only measurements collected by a single sensor.*

  This dissertation research used the high-accuracy, high-rate WAAS reference ephemerides to empirically assess geosynchronous orbit estimation accuracy given ground-based angles-only data. The reference point solutions allowed for a meter-level assessment of the dynamics of both operational and non-operational communications spacecraft. This work took advantage of the reference ephemerides published during the period of Galaxy 15's inactivity to assess the orbit accuracy for a non-maneuvering geosynchronous object. Through this analysis, guidelines were developed for meeting geosynchronous orbit accuracy requirements with two nights of optical tracking. It was shown that 10-meter accuracy is achievable given high-rate tracking for a duration of at least 3 hours each night. Furthermore, 100-meter accuracy can be achieved given only 30 minutes of tracking per night.

- *Observability of the state of a deputy object relative to a chief object given only space-based angular measurements.*

  This work demonstrated that the full relative state can indeed be recovered from space-based angles-only measurements. Using a measurement model and a two-body linearized dynamic model expressed in a spherical coordinate representation of relative motion, the observability constraints that arise when using a rectilinear coordinate dynamic model are removed. Given two spacecraft in bounded circular co-planar orbits, out-of-plane motion is required to produce observability. A relative GEO element batch estimator was constructed, and simulation studies demonstrated that the estimated uncertainty of each state decreased as observations are processed. This indicated that the filter was able to extract information about each relative GEO element from the space-based azimuth and elevation observations.

- *Modeling of estimated orbit accuracy given GEO-to-GEO space-based angles-only observations.*

  Finally, analytic models describing how the estimated uncertainty evolves over the tracking duration were developed. First-order approximated models for the batch estimated uncertainty of the along-track separation and intersatellite range magnitude were developed for close-proximity space-based angles-only tracking. The analytic uncertainty models are a function of the *a priori* covariance information, the chief spacecraft's mean motion, the measurement noise, and the change in argument of latitude of the chief spacecraft over the tracking period. In the absence of experimental data, Monte Carlo analyses were performed to numerically validate the variance models. The results show that the intersatellite range can be determined to the order of a few meters given sufficient tracking (roughly half of an orbit). The approximated uncertainty models produced by this work are an important tool in understanding the tracking requirements that must be met in order to reduce the estimated covariance to some desired level. This development will become increasingly relevant as space-based passive tracking becomes more prevalent in close-proximity geosynchronous

operations.

7.2 Future Work

Several suggestions are now made for further research. The first suggestion involves additional analysis of Galaxy 15's dynamics via the Wide Area Augmentation System (WAAS) reference ephemerides. Reference point solutions are available before, during, and after the spacecraft failure, and this presents a unique opportunity to study the dynamics of a spacecraft as it fails and is brought back online, as well as the longer-term (up to 9 months) behavior of an uncontrolled communications satellite. Also, Galaxy 15 had close approaches with several operational satellites during the time which it was uncontrolled. One of the close approach satellites is Anik F1R, which means that meter-level reference ephemerides are available for two satellites in close-proximity. This could be useful to study the close approach itself, or to validate relative motion studies when experimental ground-based or space-based angles-only data of multiple clustered objects is unavailable.

Follow-on work may also include an analysis of the geosynchronous estimation accuracy produced by estimation algorithms other than the batch processor. The use of a sequential estimation will easily allow for the inclusion of process noise, or dynamic model compensation. These filter augmentation techniques may prove to increase the orbit accuracy for experimental estimation purposes, such as when the solar radiation pressure is not perfectly modeled. Nonlinear filtering algorithms may also be beneficial, particularly when additional parameters that exhibit nonlinear time variations are included in the estimated state vector.

The space-based angles-only uncertainty models developed in this dissertation provide a first-order approximation of the estimation uncertainty given Keplerian dynamics and circular bounded relative motion. However, improvements may be made which will provide a more accurate representation of actual close-proximity operations. The Riccati differential equation used for the uncertainty modeling can be modified to include the effects of orbit perturbations such as luni-solar gravity, solar radiation pressure, and a higher-order Earth gravity model. The inclusion of orbit perturbations in the predicted uncertainty models will allow for an assessment of the impact

of dynamic mismodeling. It is of particular interest to inspect how errors in the solar radiation pressure model affect the orbit estimation accuracy. Note that a consider covariance analysis is not expected to be useful for this study due to the correlation between the effective area-to-mass ratio and the estimated GEO states, in particular the semi-major axis term.

The covariance model development presented in this work may also be expanded to include the covariance contributions, nonlinear spacecraft dynamics, and non-circular, unbounded relative motion. While a nonlinear coupled model is bound to be more complex and a closed-form solution to the resulting Riccati equation may not exist, an empirical analysis similar to that performed for the WAAS ground-based estimation accuracy assessment could be used to characterize the estimation error and uncertainty for various space-based tracking scenarios.

Finally, the quality and quantity of the angular measurements also affects the estimated covariance. The analytic covariance models can be altered to include the effects of systematic measurement errors and non-Gaussian measurement noise distributions on the relative orbit uncertainty. Case studies have been performed to study the estimation uncertainty given multiple sensors (i.e. combining ground-based and space-based data), and expansion to a general analytic covariance model incorporating multiple measurement sources will be of use for geosynchronous orbit estimation purposes.

Bibliography

[1] Odtk: A technical summary. Technical report, Analytical Graphics, Inc., January 23 2007.

[2] Federal Aviation Administration. Welcome to the william j. hughes technical center waas test team. http://www.nstb.tc.faa.gov/index.htm, January 2010.

[3] National Aeronautics and Space Administration. Sputnik and the dawn of the space age. http://history.nasa.gov/sputnik/, October 2007.

[4] National Aeronautics and Space Administration. Goddard space flight center flight dynamics facility. https://wakata.nascom.nasa.gov//, October 2009.

[5] National Aeronautics and Space Administration. Tracking and data relay satellite system (tdrss). https://www.spacecomm.nasa.gov/spacecomm/programs/tdrss/default.cfm, 2010.

[6] V. Agapov, I. Molotov, and V. Titenko. The ison international observations network - latest scientific achievement and the future works. http://lfvn.astronomer.ru/report/0000037/001/index.htm, February 2008.

[7] F. Alby. The Motion of Satellite, Lectures and Exercises on Space Mechanics, pages 569–611. Cepadues-Editions, Toulouse, Frane, 1983.

[8] R. R. Allan. Resonance effects due to the longitude dependence of the gravitational field of a rotating primary. Planetary Space Sciences, 15:53–76, 1967.

[9] Daniel L. Alspach and Harold W. Sorenson. Nonlinear bayesian estimation using gaussian sum approximations. IEEE Transactions on Automatic Control, 17(4):439–448, 1972.

[10] P. Axelrad, B. Bradley, J. Tombasco, S. Modiuddin, and J. Donna. Geo satellite positioning using gps detection. In ION GNSS 2010, Portland, OR, 2010.

[11] Richard Battin. An Introduction to the Mathematics and Methods of Astrodynamics, chapter 10.5. American Institute of Aeronautics, New York, 1999.

[12] Arthur Beer and K.A. Strand. Copernicus. Pergamon Press, Oxford, 1975.

[13] S. Bhaskaran, N. Mastrodemos, J. E. Riedel, and S. P. Synnott. Optical navigation for the stardust wild 2 encounter. Proceedings of the 18th International Symposium on Space Flight Dynamics, 2004.

[14] S. Bhaskaran, J. E. Riedel, and S. P. Synnott. Autonomous optical navigation for interplanetary missions. Proceedings of SPIE, 2810(32):133–143, 1996.

[15] Boeing. Boeing: Satellite development center. www.boeing.com/defense-space/space/bss/factsheets, October 2010.

[16] Juan Ceva. Hughes aircraft's architectural design of the federal aviation administration wide-area augmentation system: An international system. Acta Astronautica, 41(4):335–345, 1997.

[17] C. Chao and H. Bernstein. Onboard stationkeeping of geosynchronous satellites using a global positioning system receiver. Journal of Guidance, Control and Dynamics, 17(4):778–786, 1994.

[18] Tong Chen. Double line-of-sight measuring relative navigation for spacecraft autonomous rendezvous. Acta Astronautica, 67:122–134, 2010.

[19] R. Choc and R. Jehn. Classification of geosynchronous objects. Technical Report 12, European Space Operations Centre Space Debris Office, February 2010.

[20] John A. Christian and E. Glenn Lightsey. A review of options for autonomous cislunar navigation. Honolulu, HI, August 2008. AIAA Guidance, Navigation and Control Conference and Exhibit.

[21] Arthur C. Clarke. Peacetime uses for v2. Wireless World, October 1945.

[22] W. H. Clohessy and R. S. Wiltshire. Terminal guidance system for satellite rendezvous. Journal of the Aerospace Sciences, 27(9):653–658, 1960.

[23] United States Strategic Command. Space-track. http://www.space-track.org, June 2010.

[24] Kyle DeMars. Nonlinear Orbit Uncertainty Prediction and Rectification for Space Situational Awareness. PhD thesis, University of Texas, December 2010.

[25] A. J. Van Dierendonck and B. Elrod. Ranging signal control and ephemeris time determination for geostationary satellite navigation payloads. ION National Technical Meeting, 1994.

[26] A. J. Van Dierendonck and Per Enge. Global Positioning System: Theory and Applications, volume 2, chapter 4, pages 117–142. American Institute of Aeronautics, Inc., 1996.

[27] Larry Jay Friesen, Albert A. Jackson IV, Herbert A. Zook, and Donald J. Kessler. Results in orbit evolution of objects in the geosynchronous region. Journal of Guidance, Control and Dynamics, 15(1):263–267, January 1992.

[28] Arthur Gelb, editor. Applied Optimal Estimation. Cambridge: MIT Press, 1974.

[29] Robin M. Green. Spherical Astronomy. Cambridge University Press, New York, 1988.

[30] Sherry E. Hammel and Vincent J. Aidala. Observability requirements for three-dimensional tracking via angle measurements. IEEE Transactions on Aerospace and Electronic Systems, AES-21(2):200–207, March 1985.

[31] David Harrison and Joseph Chow. The space-based visible sensor. Johns Hopkins APL Technical Digest, 17(2):226–236, 1996.

[32] G. Hill. Researches in the lunar theory. American Journal of Mathematics, 1:5–26, 1878.

[33] Keric Hill, Chris Sabol, Craig McLaughlin, Kim Luu, and Michael Murai. Relative orbit determination of geosynchronous satellites using the cowpoke equations. Advances in the Astronautical Sciences, 119, 2004.

[34] University of Hawai'i Institute for Astronomy. Pan-starrs. http://pan-starrs.ifa.hawaii.edu/public/, January 2010.

[35] P. Jorgensen. Autonomous navigation of geosynchronous satellites using the navstar global positioning system. IEEE Plans, 1992.

[36] Simon J. Julier and Jeffrey K. Uhlmann. A new extension of the kalman filter to nonlinear systems. In Proceedings of SPIE, 1997.

[37] John L. Junkins. Adventures on the interface of dynamics and control. Journal of Guidance, Control and Dynamics, 20:1058–1071, 1997.

[38] A.A. Kamel. Geosynchronous satellite ephemeris due to earth's triaxiality and luni-solar effects. AIAA/AAS Astrodynamics Conference, August 1978.

[39] A.A. Kamel. On the orbit eccentricity control of synchronous satellites. AAS/AIAA Astrodynamics Specialist Conference, August 1981.

[40] A.A. Kamel. New nonsingular forms of perturbed satellite equations of motion. Journal of Guidance, Control and Dynamics, 6(5):387–392, September 1983.

[41] W. M. Kaula. Tesseral harmonics of the gravitational field and geodetic datum shifts derived from camera observations of satellites. Journal of Geophysical Research, 68(2):473–484, 1963.

[42] William M. Kaula. Theory of Satellite Geodesy. Blaisdell Publishing Company, 1966.

[43] S. Kawase. Intersatellite tracking methods for clustered geostationary satellites. IEEE Transactions on Aerospace and Electronic Systems, 26(3):469–474, 1990.

[44] S. Kawase and Y. Arimoto. Observation noise/bias errors and the geostationary orbit determination accuracy. Transactions of the Japan Society for Aeronautical and Space Sciences, 37(115):61–70, 1993.

[45] S. Kawase and F. Sawada. Interferometric tracking for close geosynchronous satellite. Journal of the Astronautical Sciences, 47(1):151–163, 1999.

[46] Seiichiro Kawase. Relative orbit estimation for co-located geostationary satellites. Japan, May 1996. 20th International Symposium on Space Technology and Science.

[47] Seiichiro Kawase. Orbit determination accuracy for optically tracked near-synchronous objects. Biarritz, France, June 2000. International Symposium on Space Dynamics.

[48] Seiichiro Kawase. Differential angle tracking for close geostationary satellites. Journal of Guidance, Control and Dynamics, 16(6):1055–1060, 2003.

[49] S. Kim, J. L. Crassidis, Y. Cheng, and A. M. Fosbury. Kalman filtering for relative spacecraft attitude and position estimation. Journal of Guidance, Control and Dynamics, 30(1):133–143, 2007.

[50] Gunther Krebs. Syncom 1, 2, 3. http://www.skyrocket.de/space/docsdat/syncom-1.htm, January 2010.

[51] M. Landgraf, G. Thiele, D. Koschny, and B. Udrea. Optical navigation for lunar exploration missions. Valencia, Spain, October 2006. 57th International Astronautical Congress.

[52] Christopher Lane and Penina Axelrad. Formation design in eccentric orbits using linearized equations of relative motion. Journal of Guidance, Control and Dynamics, 29(1):146–160, January-February 2006.

[53] A. Lemaitre, N. Delsate, and S. Valk. A web of secondary resonances for large a/m geostationary debris. Celestial Mechanics and Dynamical Astronomy, 104:383–402, 2009.

[54] Qiang Li, Fu cheng Guo, Jun Li, and Yi yu Zhou. Research of satellite-to-satellite passive tracking using bearings-only measurements in j2000 eci frame. IEEE 8th International Conference on Signal Processing, pages 1–4, 2006.

[55] A. C. Long and Jr. J. O. Cappellari. Goddard trajectory determination system (gtds) mathematical theory. Technical report, Computer Sciences Corporation, 1989.

[56] Jonathan D. Lowe, David Vallado, and Bob Hall. Technical analysis of commercially hosted optical payloads for enhanced ssa. In Proceedings of the Advanced Maui Optical and Space Surveillance Technologies Conference, Wailea, Maui, September 2010.

[57] J. Marshall and et. al. Precision orbit determination and gravity field improvement derived from tdrss. Halifax, Nova Scotia, Canada, August 14-17 1995. AAS/AIAA Astrodynamics Specialists Conference and Exhibit.

[58] Paul Maskell and Lorne Oram. Sapphire: Canada's answer to space-based surveillance of orbital objects. In Proceedings of the Advanced Maui Optical and Space Surveillance Technologies Conference, Wailea, Maui, September 2008.

[59] Chad Mendelsohn. Discussion of flight dynamics facility archival data. Personal Communication, August 2009.

[60] Pratap Misra and Per Enge. Global Positioning System: Global Positioning System: Signals, Measurements, and Performance, chapter 2. Ganga-Jamuna Press, 2006.

[61] Oliver Montenbruck. Discussion of geosynchronous satellite operations. Personal Communication, July-Aug 2010.

[62] Oliver Montenbruck and Eberhard Gill. Satellite Orbits: Models, Methods, and Applications, chapter 3, page 78. Springer, 2000.

[63] R. Musci, T. Schildknecht, T. Flohrer, and G. Beutler. Evolution of the orbital elements for objects with high area-to-mass ratios in geostationary transfer orbits. Advances in Space Research, 41:1071–1076, 2007.

[64] R. Musci, T. Schildknecht, and M. Ploner. Analyzing long observations arcs for objects with high area-to-mass ratios in geostationary orbits. Acta Astronautica, 66:693–703, 2010.

[65] CBC News. Zombie satellite to do another flyby. http://www.cbc.ca/technology/story/2010/11/04/zombie-satellite-flyby.html, November 2010.

[66] Space News. Orbital blames galaxy 15 failure on solar storm. http://www.spacenews.com/satellite_telecom/, April 2010.

[67] Spaceflight Now. Zombiesat has three more satellites in its crosshairs. http://www.spaceflightnow.com/news/n1007/25galaxy15/, July 2010.

[68] Orbital. Galaxy 12, 14 and 15 fact sheet. http://www.orbital.com/NewsInfo/Publications/, 2010.

[69] Ryan S. Park and Daniel J. Scheeres. Nonlinear mapping of gaussian statistics: Theory and applications to spacecraft trajectory design. Journal of Guidance, Control and Dynamics, 29(6):1367–1375, 2006.

[70] Ryan S. Park and Daniel J. Scheeres. Nonlinear semi-analytic methods for trajectory estimation. Journal of Guidance, Control and Dynamics, 30(6):1668–1676, 2007.

[71] Bradford W. Parkinson. Global Positioning System: Theory and Applications I. American Institute of Aeronautics and Astronautics, 1996.

[72] J. J. Pocha. An Introduction to Mission Design for Geostationary Satellites. D. Reidel, Dordrecht, 1987.

[73] A.B. Poore, B.J. Slocumb, B.J. Suchomel, F.H.Obermeyer, S.M. Herman, and S.M. Gadaleta. Batch maximum likelihood (ml) and maximum a posteriori (map) estimation with process noise for tracking applications. In Proceedings of SPIE, 2003.

[74] J. E. Riedel, W. M. Owen, J. A. Stuve, S. P. Synnott, and R. M. Vaughan. Optical navigation during the voyager neptune encounter. pages 118–128, Portland, OR, August 1990. AIAA/AAS Astrodynamics Specialist Conference.

[75] Lawrence D. Roberts. A lost connection: Geostationary satellite networks and the international telecommunication union. Berkley Technology Law Journal, 15, 2000.

[76] Chris Sabol. A Role for Improved Angular Observations in Geosynchronous Orbit Determination. PhD thesis, University of Colorado, 1998.

[77] Chris Sabol and Robert Culp. Improved angular observations in geosynchronous orbit determination. Journal of Guidance, Control and Dynamics, 24(1):123–130, January-February 2001.

[78] Chris Sabol, Tom Kelecy, and Michael Murai. Geosynchronous orbit determination using the high accuracy network determination system (hands). Wailea, Maui, February 2004. AAS/AIAA Space Flight Mechanics Meeting.

[79] Chris Sabol, Craig McLaughlin, and Kim Luu. Meet the cluster orbits with perturbations of keplerian elements (cowpoke) equations. Advances in the Astronautical Sciences, 2003.

[80] Andrew P. Sage and James L. Melsa. Estimation Theory with Applications to Communications and Control. McGraw-Hill Book Company, New York, 1971.

[81] Darryl Sanchez, Stephen Gregory, Susan Storm, Tamara Payne, and Carol Davis. Photopolarimetric measurements of geosynchronous satellites. In Proceedings of SPIE, volume 4490, 2003.

[82] Fumitake Sawada and Seiichirou Kawase. Relative orbit determination experiment by ground-based differential angle tracking. Electronics and Communications in Japan, 79(1):796–803, 1996.

[83] Hanspeter Schaub and John L. Junkins. Analytical Mechanics of Space Systems. American Institute of Aeronautics, Inc., Reston, Virginia, 2003.

[84] T. Schildknecht, R. Musci, and T. Flohrer. Properties of the high area-to-mass ratio space debris population at high altitude. Advances in Space Research, 41:1039–1045, 2008.

[85] T. Schildknecht, R. Musci, M. Ploner, G. Beutler, W. Flury, J. Kuusela, J. de Leon Cruz, and L. de Fatmia Dominguez Palermo. Optical observations of space debris in geo and in highly-eccentric orbits. Advances in Space Research, 34:901–911, 2004.

[86] J. Schmidt and T. A. Lovell. Estimating geometric aspects of relative satellite motion using angles-only measurements. Honolulu, HI, August 2008. AIAA/AAS Astrodynamics Specialist Conference.

[87] R. Lauchie Scott and Bryce Bennett. Canadian surveillance of space concept demonstrator - metric accuracy and limiting magnitude assessment. Acta Astronautica, 57:302–311, 2005.

[88] Jayant Sharma. Space-based visible space surveillance performance. Journal of Guidance, Control and Dynamics, 23(1):152–158, January-February 2000.

[89] Marcel J. Sidi. Spacecraft Dynamics and Control: A Practical Engineering Approach, chapter 2.7. Cambridge University Press, The Edinburgh Building, Cambridge CB2 2RU, UK, 1997.

[90] E.M. Soop. Handbook of Geostationary Orbits. Kluwer Academic, Dordrecht, 1994.

[91] Harold W. Sorenson and Daniel L. Alspach. Recursive bayesian estimation using gaussian sums. Automatica, 7, 1971.

[92] Space.com. 'zombie' satellite comes back to life. http://www.space.com/9677, December 29 2010.

[93] Nathan Stastny and David Gellar. Autonomous optical navigation at jupiter: A linear covariance analysis. Keystone, CO, August 2006. AAS/AIAA Astrodynamics Specialists Conference and Exhibit.

[94] B.D. Tapley, B.E. Schutz, and G.H. Born. Statistical Orbit Determination. Academic Press, 2004.

[95] B.D. Tapley, B.E. Schutz, and G.H. Born. Statistical Orbit Determination, chapter 4, pages 196–197. Academic Press, 2004.

[96] Jill Tombasco and Penina Axelrad. Observability of relative hybrid elements given space-based angles-only observations. Journal of Guidance, Control and Dynamics, Accepted for publication July 2011.

[97] Jill Tombasco and Penina Axelrad. A study of the achievable geosynchronous angles-only orbit estimation accuracy. Journal of Astronautical Sciences, Accepted for publication June 2011.

[98] Jill Tombasco, Penina Axelrad, and Moriba Jah. Specialized coordinate representation for dynamic modeling and orbit estimation of geosynchronous orbits. Journal of Guidance, Control and Dynamics, 33(6):1824–1836, November 2010.

[99] S. Valk and A. Lemaitre. Semi-analytical investigations of high area-to-mass ratio geosynchronous space debris including earth's shadowing effects. Advances in Space Research, 42:1429–1443, 2008.

[100] S. Valk, A. Lemaitre, and L. Anselmo. Analytical and semi-analytical investigations of geosynchronous space debris with high area-to-mass ratios. Advances in Space Research, 41:1077–1090, 2008.

[101] S. Valk, A. Lemaitre, and F Deleflie. Semi-analytical theory of mean orbital motion for geosynchronous space debris under gravitational influence. Advances in Space Research, 43:1070–1082, 2009.

[102] David Vallado. Fundamentals of Astrodynamics and Applications. Microcosm Press, 3 edition, 2007.

[103] David Vallado. Fundamentals of Astrodynamics and Applications, chapter 3.4.3, page 176. Microcosm Press, 3 edition, 2007.

[104] David Vallado. Evaluating gooding angles-only orbit determination of space based space surveillance measurements. In 2010 US Russian Space Surveillance Workshop, April 2010.

[105] David Vallado and Vladimir Agapov. Orbit determination results from optical observations. 2010 International Conference for Astrodynamics Tools and Techniques, May 2010.

[106] David Vallado, T.S. Kelso, Vladimir Agapov, and Igor Molotov. Orbit determination issues and results to incorporate optical measurements in conjunction operations. Fifth European Conference on Space Debris, March 2009.

[107] Benjamin Visser, Chris Sabol, and Scott Dahlke. Geosynchronous orbit determination using high accuracy angular observations. Advances in the Astronautical Sciences, 120(1):527–541, 2005.

[108] Curt von Braun, Jayant Sharma, and E. Michael Gaposchkin. Space-based visible metric accuracy. Journal of Guidance, Control and Dynamics, 23(1):175–181, January-February 2000.

[109] Mark Wade. Gorizont. http://www.astronautix.com/craft/gorizant.htm, February 2010.

[110] James R. Wertz and Wiley J. Larson, editors. Space Mission Analysis and Design. Microcosm Press, 3 edition, 1999.

[111] D. Woffinden and D. Geller. Relative angles-only navigation and pose estimation for autonomous orbital rendezvous. Journal of Guidance, Control and Dynamics, 30(5):1455–1469, 2007.

[112] D. Woffinden and D. Geller. Observability criteria for angles-only navigation. IEEE Transactions on Aerospace and Electronic Systems, 45(3), 2009.

[113] D. Woffinden and D. Geller. Optimal orbital rendezvous maneuvering for angles-only navigation. Journal of Guidance, Control and Dynamics, 32(4), July-Aug 2009.

[114] David Woffinden. Angles-Only Navigation for Autonomous Orbital Rendezvous. PhD thesis, Utah State University, December 2008.

[115] S.C. Wu, T.P. Yunck, S.M. Lichten, B.J. Haines, and R. P. Malla. Gps based precise tracking of earth satellites from very low to geosynchronous orbits. National Telesystems Conference, 1992.

[116] J. Yim, J. Crassidis, and J. Junkins. Autonomous orbit navigation of two spacecraft system using relative line of sight vector measurements. Maui, HI, February 2004. AAS Space Flight Mechanics Meeting.

[117] Simon Zajc. Herman potocnik noordung. http://noordung.vesolje.net, January 2010.

Appendix A

Derivation of Synchronous Element Nonlinear Variational Equations for General Perturbations

This Appendix presents a detailed derivation of the exact nonlinear synchronous element variational equations using the method of Poisson Brackets (Eq. 2.3). The derivation follows the method presented in Reference 11 and Reference 83.

A.1 Derivation of $\Delta\bar{a}$ Variational Equation

As $\Delta\bar{a}$ does not vary under Keplerian dynamics, only the disturbing acceleration portion of the Poisson Bracket contributes to the $\Delta\bar{a}$ dynamic equation. The derivation of the exact dynamic equation for the $\Delta\bar{a}$ synchronous element begins with the vis-viva orbital energy equation, given by:

$$\vec{v}^T\vec{v} = \frac{2\mu}{r} - \frac{\mu}{A(\Delta\bar{a}+1)} \tag{A.1}$$

in which μ is the central body gravitational parameter and $\vec{v}$ is the satellite velocity vector. Note that $\vec{v}$ is not assigned a coordinate frame. The coordinate frame independent variation of $\Delta\bar{a}$ with respect to the velocity vector is given by:

$$\frac{\partial\Delta\bar{a}}{\partial\vec{v}} = \frac{2A\vec{v}^T}{\mu}(\Delta\bar{a}^2+1) \tag{A.2}$$

A reference frame is assigned to Eq. A.2 through the definition of the velocity vector components. The position vector is defined in the rotating $\left[\hat{i}_r, \hat{i}_\theta, \hat{i}_h\right]$ local-vertical-local-horizontal (LVLH) frame by:

$$\vec{r} = r\hat{i}_r \tag{A.3}$$

The inertial time derivative of Eq. A.3 is given by:

$$\dot{\vec{r}} = \dot{r}\hat{i}_r + r\dot{\nu}\hat{i}_\theta \tag{A.4}$$

in which $\dot{\nu}$ denotes the time derivative of the true anomaly. The orbit equation and angular momentum magnitude are given by:

$$r = \frac{h^2}{\mu\left[1 + e\cos(\nu)\right]} \tag{A.5}$$

$$h = r^2\dot{\nu} \tag{A.6}$$

Using Eq. A.5 and A.6, the time rate of orbit radius magnitude is given by:

$$\dot{r} = \frac{\mu}{h}e\sin(\nu) \tag{A.7}$$

Eq. A.6 is used to express the quantity $r\dot{\nu}$ as:

$$r\dot{\nu} = \frac{\mu p}{hr} \tag{A.8}$$

Substituting Eqs. A.7 and A.8 into Eq. A.4 allows the velocity vector to be expressed in the LVLH frame as:

$$\vec{v} = \dot{\vec{r}} = \frac{\mu}{h}\left[(e_x\sin(s) - e_y\cos(s))\hat{i}_r + \frac{p}{r}\hat{i}_\theta\right] \tag{A.9}$$

Substituting Eq. A.9 into Eq. A.2 gives the LVLH frame partial derviative of $\Delta\bar{a}$ with respect to velocity as:

$$\frac{\partial\Delta\bar{a}}{\partial\vec{v}} = \frac{2(\Delta\bar{a}+1)^2}{Ah}\left[(e_x\sin(s) - e_y\cos(s))\hat{i}_r + \frac{p}{r}\hat{i}_\theta\right] \tag{A.10}$$

The disturbing acceleration vector is defined in the LVLH frame as:

$$\vec{a}_D = \begin{bmatrix} a_r & a_\theta & a_h \end{bmatrix} \tag{A.11}$$

Finally, multiplying Eq. A.10 by the disturbing acceleration vector gives the perturbed time rate of change of $\Delta\bar{a}$ as:

$$\Delta\dot{\bar{a}} = \frac{2A(\Delta\bar{a}+1)^2}{h}\left[(e_x\sin(s) - e_y\cos(s))a_r + \frac{p}{r}a_\theta\right] \tag{A.12}$$

A.2 Derivation of i_x and i_y Variational Equations

As the i_x and i_y synchronous elements do not vary under Keplerian motion, their motion is a function of only the perturbing accelerations. The angular momentum vector expressed in the orbit-fixed $\left[\hat{i}_n, \hat{i}_m, \hat{i}_h\right]$ reference frame is given by:

$$\vec{h} = h\hat{i}_h \tag{A.13}$$

The orbit frame is defined by the direction of perigee ($\hat{i}_n$), orbit normal ($\hat{i}_h$), and the completion of the right hand orthogonal frame ($\hat{i}_m$). The direction cosine matrix to rotate from the inertial $\left[\hat{i}_i, \hat{i}_j, \hat{i}_k\right]$ frame to the orbit frame is given by:

$$\begin{pmatrix} \hat{i}_n \\ \hat{i}_m \\ \hat{i}_h \end{pmatrix} = \begin{bmatrix} -i_y i^{-1} & i_x i^{-1} & 0 \\ -i_x \cos(i) i^{-1} & -i_y \cos(i) i^{-1} & \sin(i) \\ i_x \sin(i) i^{-1} & i_y \sin(i) i^{-1} & \cos(i) \end{bmatrix} \begin{pmatrix} \hat{i}_i \\ \hat{i}_j \\ \hat{i}_k \end{pmatrix} \tag{A.14}$$

This rotation matrix is used to express the angular momentum vector is terms of i_x and i_y as:

$$\vec{h} = h\hat{i}_h = h\left[i_x \sin(i) i^{-1} \hat{i}_i + i_y \sin(i) i^{-1} \hat{i}_j + \cos(i)\hat{i}_k\right] \tag{A.15}$$

The partial derivatives of i_x and i_y with respect to the velocity vector are determined by manipulating Eq. A.15. The partial derivative of Eq. A.15 is broken down into the contributions from h, i_x, and i_y as:

$$\frac{\partial \vec{h}}{\partial \vec{v}} = \frac{\partial \vec{h}}{\partial h}\frac{\partial h}{\partial \vec{v}} + \frac{\partial \vec{h}}{\partial i_x}\frac{\partial i_x}{\partial \vec{v}} + \frac{\partial \vec{h}}{\partial i_y}\frac{\partial i_y}{\partial \vec{v}} \tag{A.16}$$

Expanding the right side of Eq. A.16 produces:

$$\begin{aligned} \frac{\partial \vec{h}}{\partial \vec{v}} = & \left[\frac{i_x \sin(i)}{i}\hat{i}_i + \frac{i_y \sin(i)}{i}\hat{i}_j + \cos(i)\hat{i}_k\right]\frac{\partial h}{\partial \vec{v}} \\ & + h\left[\left(\frac{i_x^2 \cos(i)}{i^2} + \frac{i_y^2 \sin(i)}{i^3}\right)\hat{i}_i + \left(\frac{i_x i_y \cos(i)}{i^2} - \frac{i_x i_y \sin(i)}{i^3}\right)\hat{i}_j - \frac{i_x \sin(i)}{i}\hat{i}_k\right]\frac{\partial i_x}{\partial \vec{v}} \\ & + h\left[\left(\frac{i_x i_y \cos(i)}{i^2} - \frac{i_x i_y \sin(i)}{i^3}\right)\hat{i}_i + \left(\frac{i_y^2 \cos(i)}{i^2} + \frac{i_x^2 \sin(i)}{i^3} bigg)\hat{i}_j - \frac{i_y \sin(i)}{i}\hat{i}_k\right]\frac{\partial i_y}{\partial \vec{v}} \end{aligned} \tag{A.17}$$

The velocity partial derivative of the angular momentum vector is also given by:

$$\frac{\partial \vec{h}}{\partial \vec{v}} = \frac{\partial(\vec{r} \times \vec{v})}{\partial \vec{v}} = (\vec{r}\times) \tag{A.18}$$

Additionally, the satellite position vector is expressed in orbit frame components as:

$$\vec{r} = r(\cos(s-\Omega)\hat{i}_n + \sin(s-\Omega)\hat{i}_m) \tag{A.19}$$

Eq. A.19 is substituted into Eq. A.18, and the result is set equal to Eq. A.17. Next, the inertial frame unit vectors are expressed in orbit frame components using Eq. A.14. Though the resulting equation is quite algebraically complex, multiplication by the $\hat{i}_n$ and $\hat{i}_m$ unite vectors isolates the orbit frame components and provides two independent equations which are functions of $\frac{\partial i_x}{\partial \vec{v}}$ and $\frac{\partial i_y}{\partial \vec{v}}$. The partial derivates are then solved algebraically as:

$$\frac{\partial i_x}{\partial \vec{v}} = \left[\frac{r}{h}\sin(\Omega)\cos(\omega+\nu) + \frac{ir}{h\sin(i)}\cos(\Omega)\sin(\omega+\nu)\right]\hat{i}_h \tag{A.20}$$

$$\frac{\partial i_y}{\partial \vec{v}} = \left[\frac{ir}{h\sin(i)}\sin(\Omega)\sin(\omega+\nu) - \frac{r}{h}\cos(\Omega)\cos(\omega+\nu)\right]\hat{i}_h \tag{A.21}$$

Multiplication by the LVLH frame disturbing acceleration vector completes the Poisson Bracket derivation of the exact nonlinear i_x and i_y variational equations, given by:

$$\dot{i}_x = \left[\frac{r}{h}\sin(\Omega)\cos(\omega+\nu) + \frac{ir}{h\sin(i)}\cos(\Omega)\sin(\omega+\nu)\right]a_h \tag{A.22}$$

$$\dot{i}_y = \left[\frac{ir}{h\sin(i)}\sin(\Omega)\sin(\omega+\nu) - \frac{r}{h}\cos(\Omega)\cos(\omega+\nu)\right]a_h \tag{A.23}$$

A.3 Derivation of e_x and e_y Dynamic Equations

The eccentricity synchronous elements are only varied through orbit perturbations. To begin the Poisson Bracket derivation of the variational equations, the angular momentum magnitude is expressed as:

$$h^2 = r^2\vec{v}^T\vec{v} - (\vec{r}^T\vec{v})^2 \tag{A.24}$$

The partial derivative of Eq. A.24 with respect to the velocity vector is given by:

$$\frac{\partial h}{\partial \vec{v}} = r^2\vec{v}^T - (\vec{r}^T\vec{v})\vec{r}^T \tag{A.25}$$

The angular momentum magnitude can also be expressed in terms of the synchronous elements as:

$$h^2 = A\mu(\Delta\bar{a}+1)(1-e_x^2-e_y^2) \tag{A.26}$$

The partial derivative of Eq. A.26, using Eq. A.10, is given by:

$$\frac{\partial h}{\partial \vec{v}} = -2a\mu\left(e_x\frac{\partial e_x}{\partial \vec{v}} + e_y\frac{\partial e_y}{\partial \vec{v}} - \frac{a(1-e_x^2-e_y^2)}{2h}\left[(e_x\sin(s)-e_y\cos(s))\hat{i}_r + \frac{p}{r}\hat{i}_\theta\right]\right) \tag{A.27}$$

Setting Eq. A.25 equal to Eq. A.27 provides one algebraic equation in terms of the two unknown partial derivatives, $\frac{\partial e_x}{\partial \vec{v}}$ and $\frac{\partial e_y}{\partial \vec{v}}$.

A second equation in terms of both partial derivatives is necessary. The partial derivative of the orbit equation (Eq. A.5) is given by:

$$2h\frac{\partial h}{\partial \vec{v}} = r\mu\left(\cos(s)\frac{\partial e_x}{\partial \vec{v}} + \sin(s)\frac{\partial e_y}{\partial \vec{v}} + [e_y\cos(s)-e_x\sin(s)]\frac{\partial s}{\partial \vec{v}}\right) \tag{A.28}$$

Using the definition of s (Eq. 2.13) and the partial derivatives of the Keplerian elements ν, Ω, and ω presented in Reference 83, the partial derivative of the sidereal angle is given by:

$$\frac{\partial s}{\partial \vec{v}} = \frac{\partial \Omega}{\partial \vec{v}} + \frac{\partial \omega}{\partial \vec{v}} + \frac{\partial \nu}{\partial \vec{v}} = [1-\cos(i)]\frac{r\sin(\theta)}{h\sin i}\hat{i}_h \tag{A.29}$$

Substituting Eq. A.29 and Eq. A.25 into Eq. A.28 provides a second independent equation in terms of the e_x and e_y partial derivatives. Solving simultaneously with the first equation in terms of both unknown partial derivatives and subsituting in the position and velocity vectors (Eqs. A.3 and A.9) produces the partial derivatives of e_x and e_y with respect to the velocity vector, as given by:

$$\dot{e}_x = \frac{r}{h}\left\{\frac{p}{r}\sin(s)\hat{i}_r + \left[e_x + (1+\frac{p}{r})\cos(s)\right]\hat{i}_\theta\right\} + e_y\frac{r}{h}\left\{\left[\tan(\frac{i}{2})\sin(\Omega)\cos(s) - \tan(\frac{i}{2})\cos(\Omega)\sin(s)\right]\hat{i}_h\right\} \tag{A.30}$$

$$\dot{e}_y = \frac{r}{h}\left\{\frac{-p}{r}\cos(s)\hat{i}_r + \left[e_y + (1+\frac{p}{r})\sin(s)\right]\hat{i}_\theta\right\} - e_x\frac{r}{h}\left\{\left[\tan(\frac{i}{2})\sin(\Omega)\cos(s) - \tan(\frac{i}{2})\cos(\Omega)\sin(s)\right]\hat{i}_h\right\} \tag{A.31}$$

To complete the derivation of the variational equations, Eqs. A.30 and A.31 are multiplied by the disturbing acceleration vector (Eq. A.11). The resulting exact nonlinear variational equations are given by:

$$\dot{e}_x = \frac{r}{h}\left\{\frac{p}{r}\sin(s)a_r + \left[e_x + (1+\frac{p}{r})\cos(s)\right]a_\theta\right\} + e_y\frac{r}{h}\left\{\left[\tan(\frac{i}{2})\sin(\Omega)\cos(s) - \tan(\frac{i}{2})\cos(\Omega)\sin(s)\right]a_h\right\} \quad \text{(A.32)}$$

$$\dot{e}_y = \frac{r}{h}\left\{\frac{-p}{r}\cos(s)a_r + \left[e_y + (1+\frac{p}{r})\sin(s)\right]a_\theta\right\} - e_x\frac{r}{h}\left\{\left[\tan(\frac{i}{2})\sin(\Omega)\cos(s) - \tan(\frac{i}{2})\cos(\Omega)\sin(s)\right]a_h\right\} \quad \text{(A.33)}$$

A.4 Derivation of λ Dynamic Equation

The longitude synchronous element, λ, varies both naturally and under orbit perturbations. As such, the λ variational equation is defined as:

$$\frac{d\lambda}{dt} = \frac{\partial\lambda}{\partial\vec{v}}\vec{a}_D + \frac{\partial\lambda}{\partial t} \quad \text{(A.34)}$$

The definition of λ (Eq. 2.7) is differentiated with respect to time to produce:

$$\frac{\partial\lambda}{\partial t} = \frac{\partial s}{\partial t} - \frac{\partial G(t)}{\partial t} \quad \text{(A.35)}$$

The time derivative of the Greenwich angle is simply the rotation rate of the Earth, ω_E. The time partial derivative of the sidereal angle is computed by differentiating the sidereal angle definition, Eq. 2.13 and substituting the Keplerian element time partial derivatives presented in Reference 83. The sidereal angle time partial derivative is given by:

$$\frac{\partial s}{\partial t} = \frac{\partial\Omega}{\partial t} + \frac{\partial\omega}{\partial t} + \frac{\partial\nu}{\partial t} = \frac{h}{r^2} \quad \text{(A.36)}$$

Substituting Eq. A.36 and the Earth rotation rate into Eq. A.37 produces the time partial derivative of λ as:

$$\frac{\partial\lambda}{\partial t} = \frac{h}{r^2} - \omega_E \quad \text{(A.37)}$$

Using Eq. A.29 and the definition of λ, the velocity vector partial derivative of λ is given by:

$$\frac{\partial \lambda}{\partial \vec{v}} = \frac{\partial s}{\partial \vec{v}} = [1 - \cos(i)] \, \frac{r \sin(\theta)}{h \sin i} \hat{i}_h \tag{A.38}$$

Substituting Eqs. A.37, A.38 and A.11 into Eq. A.34, the exact variational equation of λ is given by:

$$\dot{\lambda} = \frac{h}{r^2} + \frac{r}{h} \tan(\frac{i}{2}) \sin(\omega + \nu) a_h - \Omega_E \tag{A.39}$$